

POLITECNICO DI TORINO

Corso di Laurea Magistrale in Ingegneria Elettronica

Tesi di Laurea Magistrale

**Study and development of high  
voltage energy harvesting and  
storage power-pack for indoor  
application**



Relatore:

Dr. Andrea LAMBERTI

Candidato:

Ioannis STRATAKIS

01/04/2020

# Dedication

Ai miei amati genitori, fari luminosi nelle giornate burrascose, che mi hanno insegnato a vedere negli abissi non la paura dell' ignoto, ma il fascino dell' inesplorato.

# Acknowledgments

Vorrei ringraziare il mio relatore, Dr. Andrea Lamberti, e il dott. Roberto Speranza, per avermi seguito in questo lavoro. Un grazie di cuore ai miei genitori, Anna Maria ed Emmanuil, che mi hanno sempre supportato in questi anni di studio. Επίσης, δράπτομαι της ευκαιρίας να ευχαριστήσω τον παππού μου από την πανέμορφη Κρήτη. Του στέλνω πολλά χαιρετίσματα και πολλή αγάπη. Θέλω να ευχαριστήσω και τον αδελφικό μου φίλο τον Γιάννη για όσα έκανε για μένα. Τα φοιτητικά μου χρόνια θα ήταν πολύ διαφορετικά χωρίς αυτόν.

Ringrazio infine i miei amici, Mario, Valerio e Martina, che ho molto stimato durante i miei studi torinesi, e il mio coinquilino Giovanni, con cui ho condiviso i momenti più belli della quotidianità di uno studente fuorisede.

# Table of contents

<b>Dedication</b>	I
<b>Acknowledgments</b>	II
<b>1 Theoretical aspects</b>	<b>2</b>
1.1 The solar resource . . . . .	2
1.2 Fundamentals of photovoltaics . . . . .	3
1.2.1 Solar cells: a simple circuitual model . . . . .	9
1.2.2 Solar cells II: I-V characteristic and fundamental parameters . . . . .	10
1.2.3 Light-matter interaction basics . . . . .	16
1.3 Dye-Sensitized-Solar-Cells . . . . .	18
1.4 Supercapacitors . . . . .	22
1.4.1 Materials for supercapacitors . . . . .	27
1.4.2 Supercapacitors: performance evaluation . . . . .	29
1.5 Electrochemical Impedance Spectroscopy, Cyclic Voltammetry and Galvanostatic Charge-Discharge: Basics . . . . .	31
1.5.1 Electrochemical Impedance Spectroscopy . . . . .	31
1.5.2 Cyclic Voltammetry . . . . .	35
1.5.3 Galvanostatic Charge-Discharge . . . . .	37
1.6 A Dssc-supercapacitor power-pack system . . . . .	39
<b>2 Experimental Part</b>	<b>41</b>
2.1 DSSC materials . . . . .	41
2.1.1 Oxide Semiconductor . . . . .	41
2.1.2 Sensitizer . . . . .	43
2.1.3 Electrolyte . . . . .	45
2.1.4 Counter electrode and substrate . . . . .	46
2.2 DSSC module characterization . . . . .	46
2.2.1 Indoor light sources . . . . .	48
2.3 Device fabrication . . . . .	49
2.4 Commercial Supercapacitor characterization . . . . .	58
<b>3 Results</b>	<b>60</b>
3.1 Test 1 . . . . .	61
3.2 Test 2 . . . . .	64
3.3 Test 3 . . . . .	66

3.4	Test 4 . . . . .	67
3.5	Fabrication and characterization of the final DSSCs module . . . . .	74
	3.5.1 DSSCs module EIS . . . . .	81
	3.5.2 Indoor Measurements . . . . .	83
	3.5.3 Module stability with respect to time . . . . .	93
3.6	Energy harvesting module with transparent $TiO_2$ round photoanodes	95
3.7	Energy harvesting module with transparent $TiO_2$ squared photoanodes	101
3.8	Transparent and opaque $TiO_2$ paste: a comparison . . . . .	108
3.9	HS power-pack system: characterization and testing . . . . .	109
	3.9.1 HS power-pack test . . . . .	112
<b>4</b>	<b>Conclusions and future developments</b>	<b>114</b>

# List of tables

1.1	Electrical elements impedances and phase shifts . . . . .	34
3.1	DSSCs module parameters . . . . .	69
3.2	DSSCs module parameters under different illumination conditions . .	71
3.3	DSSCs module parameters . . . . .	73
3.4	DSSCs module parameters . . . . .	77
3.5	DSSCs module parameters (with back-mirroring) . . . . .	79
3.6	DSSCs module parameters under different illumination conditions . .	80
3.7	Results under different indoor illumination conditions (LED) . . . . .	85
3.8	Results under different indoor illumination conditions (flu. lamp) . .	87
3.9	Results under different indoor illumination conditions (halogen lamp)	89
3.10	V-J curves measured on different days. . . . .	94
3.11	Module parameters transparent $TiO_2$ (device1) . . . . .	97
3.12	Module parameters transparent $TiO_2$ (device2) . . . . .	99
3.13	Module parameters with back-mirroring under different illumination conditions (device 2) . . . . .	100
3.14	Module parameters transparent $TiO_2$ (squared electrodes) . . . . .	105
3.15	Module parameters under different illumination conditions (squared electrodes) . . . . .	106

# List of figures

1.1	Standard Solar Spectra for space and terrestrial use[3]	3
1.2	Energy band diagram of a silicon p-n junction solar cell[5]	5
1.3	Best Research-Cell Efficiency Chart[9]	8
1.4	Solar cell equivalent circuit [10]	9
1.5	I-V characteristic solar cell[11]	11
1.6	FF graphical interpretation[12]	13
1.7	Quantum Efficiency [13]	15
1.8	Beer-Lambert law[15]	17
1.9	DSSC structure and working principle[17]	19
1.10	DSSC electron transfer processes[2]	21
1.11	DSSC electron transfer processes and time constants[2]	22
1.12	Ragone chart[19]	23
1.13	Supercapacitor generic structure[21]	24
1.14	Helmholtz double layer[20]	26
1.15	Nyquist plot DSSC	33
1.16	Bode plots DSSC	33
1.17	Potential profile CV[29]	35
1.18	CV different scan rates[31]	37
1.19	Galvanostatic discharge for different storage devices[21]	38
2.1	N-719 chemical structure[18]	43
2.2	N-719 absorption spectrum[44]	44
2.3	N-719 adsorbed on $TiO_2$ electrode: absorption spectrum[45]	44
2.4	Solar Simulator	47
2.5	Graphical interface	47
2.6	Indoor lights spectra	48
2.7	W-type series connection[47]	49
2.8	Glass substrates	49
2.9	FTO patterning	50
2.10	Titania deposition preparation	50
2.11	Titania deposition	51
2.12	Sintering oven	52
2.13	Sintered $TiO_2$ transparent paste	53
2.14	Sintered $TiO_2$ transparent paste	53
2.15	Pt sputtering preparation	54
2.16	Pt electrodes deposition	54
2.17	$TiO_2$ photoanodes after the dye adsorption	55

2.18	Hot press	55
2.19	Sealing mechanism	56
2.20	Final result after sealing	57
2.21	DSSC harvesting module	57
2.22	Cyclic voltammetry commercial SC	58
2.23	EIS commercial SC	59
3.1	2 series-connecte DSSCs module	62
3.2	V-J curve under 1 SUN and dark illumination conditions (Test 1)	63
3.3	Power curve 2 series-connected DSSC module	64
3.4	6 series-connected DSSCs sharing the electrolyte	65
3.5	V-J curve under 1 SUN illumination condition (Test 2)	65
3.6	Power curve 6 series-connected DSSCs module(shared electrolyte)	66
3.7	6 series-connected DSSCs module parafilm sealing	67
3.8	6 series-connected DSSCs module substrates	68
3.9	V-J curve (Test 4)	68
3.10	V-J curve under different illumination conditions (Test 4)	70
3.11	V-J curve (Test 4, 2 <sup>nd</sup> module)	72
3.12	V-J curves comparison	74
3.13	Final DSSCs module (balanced electrodes)	75
3.14	V-J curves	76
3.15	V-J curves comparison with and without mirroring	78
3.16	V-J curve under different illumination conditions	80
3.17	Impedance spectrum DSSCs module (Nyquist plot)	81
3.18	Indoor measurements setup	83
3.19	V-J curve indoor measurements LED lamp	84
3.20	V-J curve indoor measurements fluorescent lamp	86
3.21	V-J curve indoor measurements halogen lamp	88
3.22	Halogen spotlight	90
3.23	Halogen spotlight illumination	90
3.24	Lamps emission spectra and N-719 dye on $TiO_2$ absorptium spectrum	91
3.25	V-J curves indoor comparison (@ 1000lux)	92
3.26	V-J curves measured on different days	93
3.27	Energy harvesting module	95
3.28	V-J curve transparent $TiO_2$ module (device1)	96
3.29	V-J curve transparent $TiO_2$ module (device2)	98
3.30	V-J curves under different illumination conditions transparent $TiO_2$ (device 2)	98
3.31	Damaged photoanodes	101
3.32	Squared electrodes (balanced)	102
3.33	DSSCS module with squared electrodes	102
3.34	V-J curve with/without back-mirroring (squared electrodes)	103

3.35	V-J curves under different illumination conditions (squared electrodes)	104
3.36	Impedance spectrum DSSCs module (Nyquist plot)	107
3.37	V-J curves of transparent and opaque $TiO_2$ photoanodes DSSCs modules	108
3.38	Charge and galvanostatic discharge 33mF commercial supercapacitor	109
3.39	OPECSE(%) with respect to photocharging time	110
3.40	OPECSE(%) with respect to the changing voltage	110
3.41	Power-pack system test a)	112
3.42	Power-pack system test b)	113
3.43	Power-pack system testbench	113

# Introduction

The last decades have been characterized by a massive population growth which induced a global increase in energy demand. As a matter of fact, energy supply plays a great role in ensuring us a good quality of life. Until now fossil fuels have covered most of our energy needs, but this trend cannot go on for a long time yet. In fact, fossil resources progressive extinction and their dramatic environmental impact, combined with nuclear power safety and waste management concerns, have led to a widespread interest in renewable energies exploitation. Among renewable resources, solar energy plays a key role because of the huge amount of power we receive every year to the earth's surface in the form of sunlight. At this point the challenge becomes to convert light energy into electrical energy and furthermore to store and distribute it.

In this regard, the aim of this master thesis is to develop and fabricate a energy harvesting and storage system to feed a simple electronic device. More in details, this system is made up of a photovoltaic device consisting of six Dye-sensitized solar cells, a particular type of third generation solar cells as it will be clarified later, and a commercial supercapacitor as the storage element. The former has been entirely realized, characterized and tested by the author at DISAT labs (Polytechnic University of Turin, Italy).

As regards the content organization of this master thesis, it will first present the theoretical concepts needed to get a deep understanding of the work done. Afterwards a detailed explanation of the fabrication steps, the performed measurements and the subsequent experimental results analysis is given. Finally the work is concluded presenting a simple application of the power-pack, some possible improvements and future scenarios.

# Chapter 1

## Theoretical aspects

### 1.1 The solar resource

The sun is the star of our planet system. Its average distance from the earth is about 150 million Kms, meaning that about eight minutes are needed from the light to reach us. Every year an average amount of about 3.8 million EJ reaches the earth's surface in the form of solar radiation. This is more than 10.000 times world's energy demand [1]. This means that, in principle, it would be sufficient to cover just 0.1% of the world's surface with solar cells having 10% efficiencies to cover all the current global energy demand.

To define quantitatively the amount of power per unit area that reaches a given surface from the sun a parameter called irradiance, measured in  $Wm^{-2}$ , is introduced. In photovoltaics it is common place to measure the irradiance in "SUN", given that  $1 \text{ SUN} = 1000Wm^{-2}$ . It is clear that we get the maximum radiation on the earth when the sun rays have the shortest path length through the atmosphere. The path length is defined through a quantity called air mass(AM) which is approximately equal to the ratio  $\frac{1}{\cos\phi}$  where  $\phi$  is the zenith angle. The solar irradiance is made up of two components: direct irradiance and diffuse irradiance. The former represents the amount of power that reaches the earth's surface without being absorbed or scattered by the atmosphere from its line of propagation; the latter instead is due to the scattering of the sunlight in the atmosphere and it represents on average the 15% of total irradiance[2]. This incident light radiation has a spectrum, called "solar

spectrum”, which rigorously speaking is not constant. In fact, it changes depending on the sun activity, location, hour of the day, season. Despite this, a standard solar irradiation condition with a zenith angle  $\phi = 42^\circ$ , called ”AM1.5 Global”, is internationally considered when performing measurements on photovoltaic devices. The aforementioned solar spectrum and the two other standard spectra used for space and terrestrial applications are reported in Fig.1.1 taken from [3]

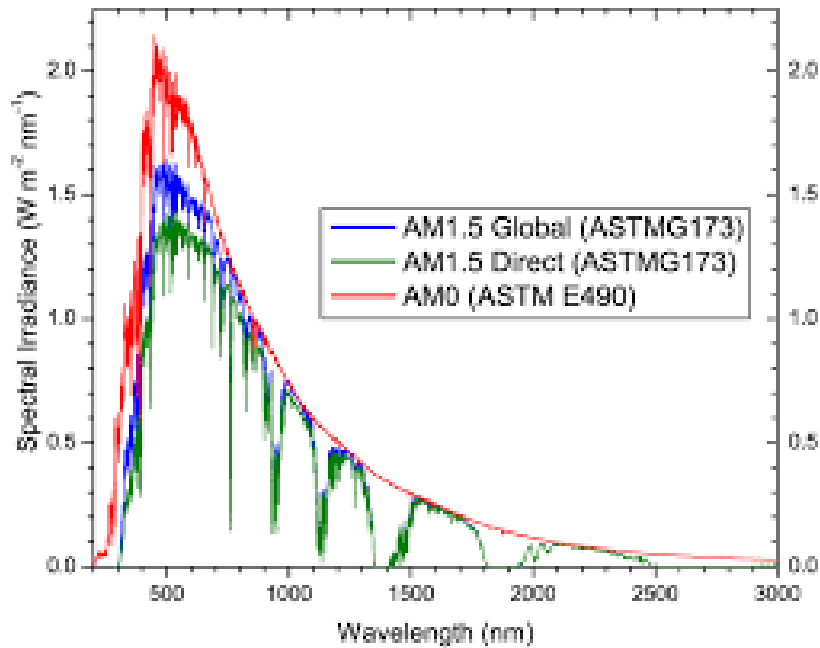


Figure 1.1: Standard Solar Spectra for space and terrestrial use [3]

## 1.2 Fundamentals of photovoltaics

The word ”Photovoltaics” refers to the conversion of solar energy into electricity. This effect was firstly observed by the French Physicist Alexandre-Edmond Becquerel in 1839. [4] The devices that allow this energy transformation are called ”solar cells”. The first modern silicon based solar cell was invented by the American engineer Russel Ohl in 1946. [4] This kind of devices should ideally satisfy the following

characteristics:

- high efficiency
- low cost
- long term stability and endurance
- biocompatibility
- abundant raw materials

In photovoltaics it is common place to divide solar cells into three generations according to their physical implementation cost and performance. The first generation technology solar cells are still the most efficient and popular in the market. They are based on silicon wafers which can be mono or multicrystalline.

It is well known that silicon can be both p-type(using an element of the III group of the periodic table such as Boron) and n-type(using an element of the V group i.e. Phosphorus) doped. If the p-type and the n-type semiconductors are joined together the formation of the so called "p-n junction" takes place. It can be shown that, because of concentration gradients, holes will diffuse across the junction from the p-side to the n-side and similarly electrons will diffuse from the n-side to the p-side of the device. Due to charge neutrality conservation law, this carriers migration leaves a region straddling the p-n interface which has positive fixed charges in the n-type semiconductor and negative fixed charges in the p-type part. This region is called "space-charge" or "depletion"(meaning depleted from mobile carriers) region and generates a potential difference across the junction("built-in potential"). The electric field due to the built-in potential induces a drift net current that opposes the diffusion process, trying to balance it. At the equilibrium this balance is perfect ,meaning that the absolute value of the drift current is equal to the absolute value of the diffusion current and therefore the net current across the junction is zero.

First generation solar cells are based on the silicon p-n junction. More in details, we have that when a photon of the incident sunlight, with its energy  $h\nu$  (where  $h = 6.626 \cdot 10^{-34} m^2 \frac{Kg}{s}$  is the Planck's constant and  $\nu$  is the frequency), reaches the space-charge region, it makes an electron of the silicon valence band being promoted to the conduction band generating an electron-hole pair which is then separated by the built-in electric field. Fig. 1.2 taken from [5] graphically shows the described phenomenon.

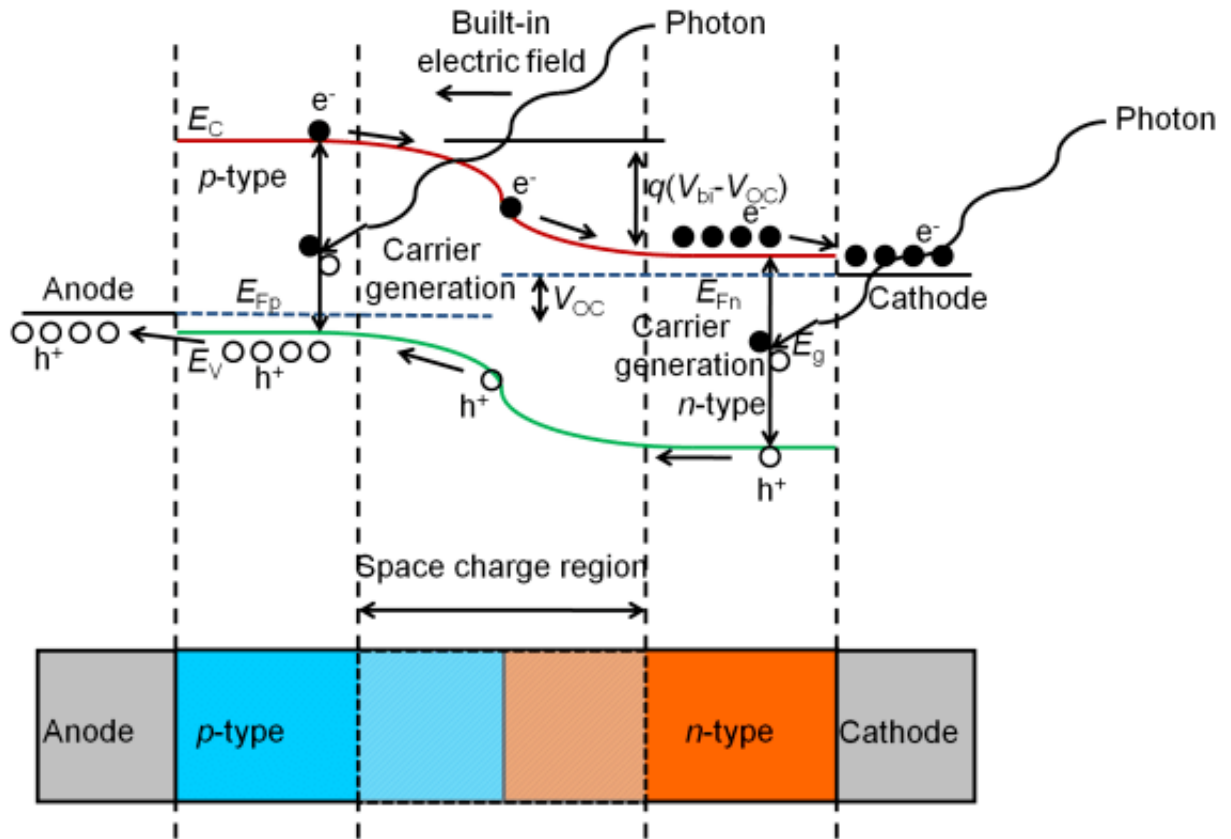


Figure 1.2: Energy band diagram of a silicon p-n junction solar cell[5]

Therefore, as soon as the separated charges exit the space-charge region, they can be collected at the positive and negative contacts constituting the photogenerated cell current. These monocrystalline silicon based solar cells show high efficiency, but

high cost too and this is due to expensive manufacturing process. To mitigate this issue polycrystalline silicon can be realized showing slightly lower efficiency, but also lower costs because of simpler manufacturing processes.

As regards second generation solar cells, they are mostly represented by thin-film solar cells, which are divided into three groups:

- amorphous-silicon solar cells(a-Si)
- Cadmium-Telluride solar cells(CdTe)
- CIGS(copper indium galliumdi-selenide).

At this point, it is mandatory to make a note. Silicon has encountered a so wide success in the PV industry thanks to the following pros: it is the second most abundant element on the earth after oxygen, it has a well established manufacturing technology due to its unquestionable success in electronics. On the other hand, being an indirect bandgap semiconductor material, it shows a low absorption coefficient(even though a low charge carrier recombination too) that significantly affects the efficiency requiring relatively thick layers to better absorb sunlight intensity( $\approx 350 \mu m$  according to [4]). Second generation solar cells are instead much thinner ( $\approx 1 \mu m$  [4]), as they exploit direct band gap semiconductors, less expensive(just think about amorphous silicon, for example, which involves much cheaper fabrication steps), but less efficient too. An exception to this general trend is represented by GaAs(gallium arsenide) based solar cells, which formally are considered as second generation solar cells, but are more efficient and more expensive than the silicon based ones. But, at the same time, gallium and arsenic are much more rare than silicon, arsenic is considered carcinogenic too, and manufacturing processes are really expensive.

The physics underlying second generation solar cells is always the p-n junction one

and therefore both first and second generation solar cells share the so called Shockley-Queisser limit [6], which is an upper theoretical limit for the efficiency of p-n junction based solar converters that considers only radiative recombination mechanisms for electron hole-pairs. As for instance, for silicon, which has an energy gap equal to 1.1 eV, the maximum obtainable efficiency is around 30% [6].

The third generation of solar cells have been introduced in order to try to overcome this efficiency limitation. It represents the most recent frontier in photovoltaics and hence has not been commercially implemented in large scale yet. This generation groups all the different technologies that are not ascribable to the first and the second ones, such as:

- dye-sensitized solar cells
- organic solar cells
- perovskite solar cells
- concentrated solar cells

Very high efficiencies have been reached by concentrated solar cells (larger than 40%) and perovskite solar cells (larger than 23%[7]), but they are critical from the long-life performance point of view. Organic solar cells and DSSCs, on the other hand, have shown not so high efficiencies, but very good performances in terms of low cost and lightweight nature. In particular, organic solar cells are characterized by the use of organic materials(i.e. polymers,small molecules) in the active layers and they show an efficiency of about [3%-10%] [4]. DSSCs finally are characterized by an efficiency slightly above 14%[8] and will be extensively described in 1.3 being the photovoltaic technology used in this master thesis.

To give a synoptic chart, concerning the many different photovoltaic technologies

and their performances, Fig. 1.3 reported from [9] shows the highest confirmed conversion efficiencies for research cells from 1976 to the present.

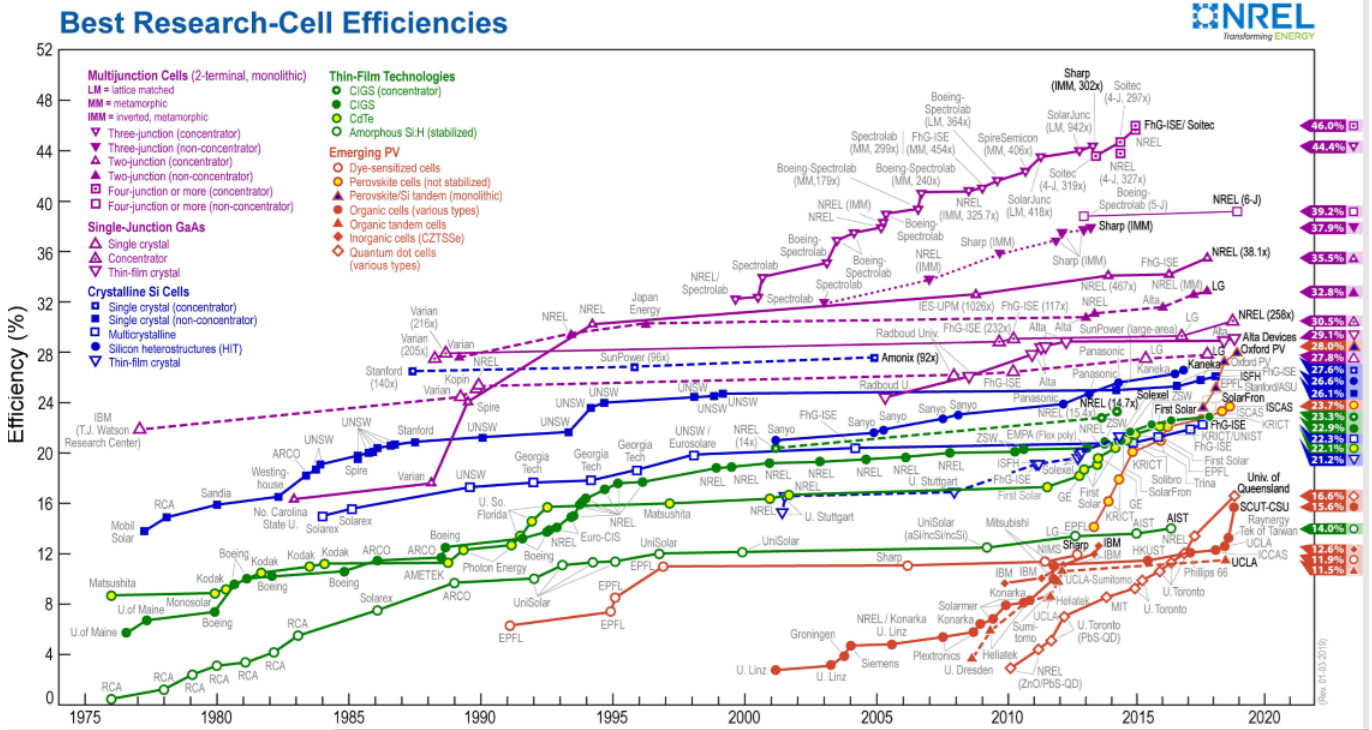


Figure 1.3: Best Research-Cell Efficiency Chart[9]

### 1.2.1 Solar cells: a simple circuital model

Considering the physical behaviour of a solar cell described above, it is easy to derive its equivalent circuit. In fact, in the ideal case, we will have a simple independent current generator (modeling the photogenerated current) connected in parallel to a diode which is responsible of the charge separation. Moreover, to take into account the many different non-idealities, it is mandatory to introduce two parasitic resistances (namely  $R_s$  and  $R_{sh}$ ) as depicted in Fig. 1.4 reported from [10].

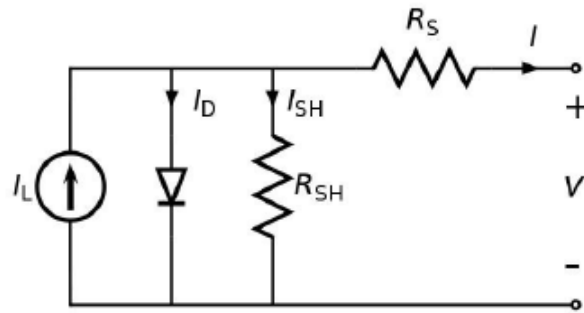


Figure 1.4: Solar cell equivalent circuit [10]

In particular, the presence of the series resistance  $R_s$  is due to the non ideal contacts, which of course exhibit a parasitic resistance contribution, and to charge transfer resistances. Being a detrimental component, the ideal value for  $R_s$  would be  $0\Omega$ .

$R_{sh}$ , instead, is the shunt resistance whose ideal value should be infinite. It is mainly due to manufacturing defects than effectively poor solar cell design. This resistance creates an alternative route for the photocurrent causing a significant power loss and thus lowering the efficiency.

## 1.2.2 Solar cells II: I-V characteristic and fundamental parameters

The I-V curve is a very important tool that gives us many important informations about the solar cell performances. It is obtained by adding the solar cell diode current in the dark to the photogenerated current. Therefore, the well known diode characteristic equation becomes:

$$I = I_0[e^{\frac{V}{nV_T}} - 1] - I_L \quad (1.1)$$

Where  $I_0$  is the reverse saturation current,  $V$  is the voltage across the diode and  $V_T = \frac{k_B T}{q}$  is the thermal voltage ( $k_B = 1.380649 \cdot 10^{-23} JK^{-1}$  is the Boltzmann constant). Being the exponential term much greater than one in absolute value (at least when  $v \geq 100mV$ ), the term "-1" can be neglected in equation 1.1. At this point, by changing the sign of both hands of equation 1.1, we obtain the following expression:

$$I = +I_L - I_0 e^{\frac{V}{nV_T}} \quad (1.2)$$

Plotting the equation above we get the red curve depicted in figure 1.5, taken from [11]. The blue curve, representing the power from the solar cell, has been superimposed on the I-V characteristic just recalling that  $P = V \cdot I$

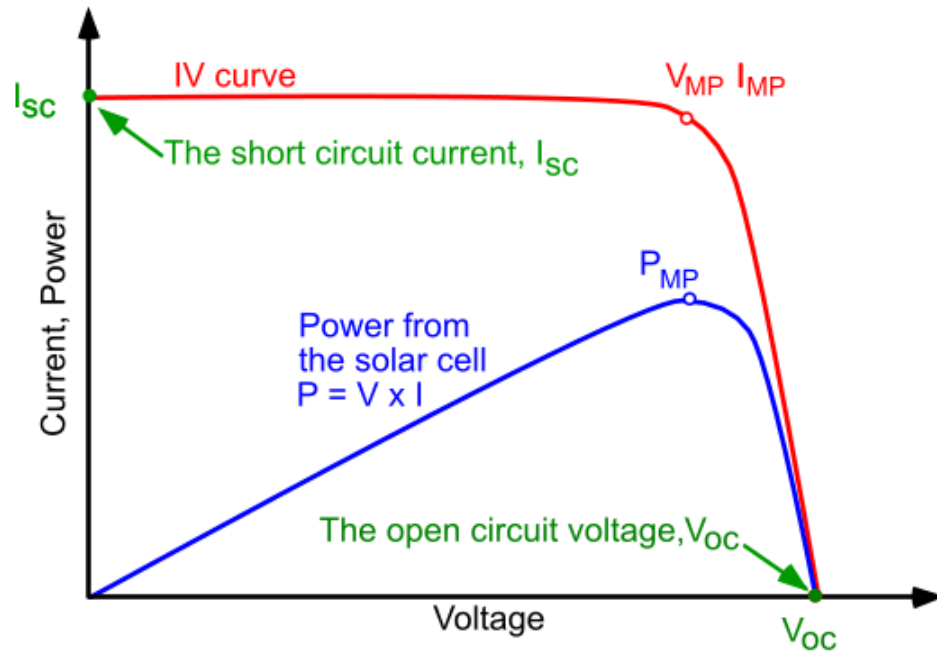


Figure 1.5: I-V characteristic solar cell[11]

As it was stated before, from figure 1.5 it is possible to read out some key parameters that allow us to evaluate how good a solar cell is. The most important ones are briefly described below.

### Short circuit current $I_{sc}$

It is defined as the current flowing through the solar cell when it is short circuited or, in other words, when its load has a null impedance. This value can be read from fig. 1.5 considering the point in which  $V = 0$ . In photovoltaics it is customary to define the short circuit current density  $J_{sc} = \frac{I_{sc}}{A}$ , where  $A$  is the effective area of the solar cell, to make the parameter independent from dimension.  $J_{sc}$  depends on many variables such as: solar illumination, charge transport effectiveness and materials' optical properties.[10]

**Open circuit voltage  $V_{OC}$** 

The open circuit voltage ( $V_{OC}$ ) is the maximum voltage that can be provided from a solar cell. It is defined as the voltage on the cell when the load has an infinite impedance.  $V_{OC}$  can be read from the I-V characteristic considering the point in which the current through the solar cell is equal to 0. Therefore, it is graphically given by the intersection point between the I-V curve and the x-axis. It is possible to derive a quantitative expression for  $V_{OC}$  by setting  $I = 0$  in equation 1.2 and thus obtaining:

$$V_{OC} = \eta V_T \ln\left(\frac{I_L}{I_0} + 1\right) \quad (1.3)$$

It can be proved that  $V_{OC}$  decreases with temperature. From equation 1.3, however, it may seem that  $V_{OC}$  increases linearly with respect to temperature, but this is not correct since  $I_0$  depends on temperature as well.

**Fill Factor (FF)**

The short-circuit current and the open-circuit voltage are respectively the maximum current and voltage from the solar cell. However, as it can be easily seen from the I-V characteristic, when the cell is working in these two operating points the power from the cell is zero. The maximum power point, instead is characterized by a current and a voltage which are indicated by  $I_{MPP}$  and  $V_{MPP}$  respectively.

It is to be noted that  $V_{MPP}$  can be found by imposing:

$$\frac{d(IV)}{dV} = 0$$

Therefore, it can be stated that the "fill factor", indicated by FF, is a parameter which gives us informations about the maximum power output from the cell. Mathematically, it is defined by the following expression:

$$FF = \frac{V_{MPP} \cdot I_{MPP}}{V_{OC} \cdot I_{SC}} \quad (1.4)$$

Thus, it is the ratio between the maximum power from the solar cell and the product  $V_{OC} \cdot I_{SC}$ . A graphical interpretation can be given considering Fig.1.6 taken from [12]. The FF is the ratio between the dark purple rectangle and the light mauve one. It is a measure of the "squareness" of the I-V curve being the area of the largest rectangle that could fit in the characteristic.

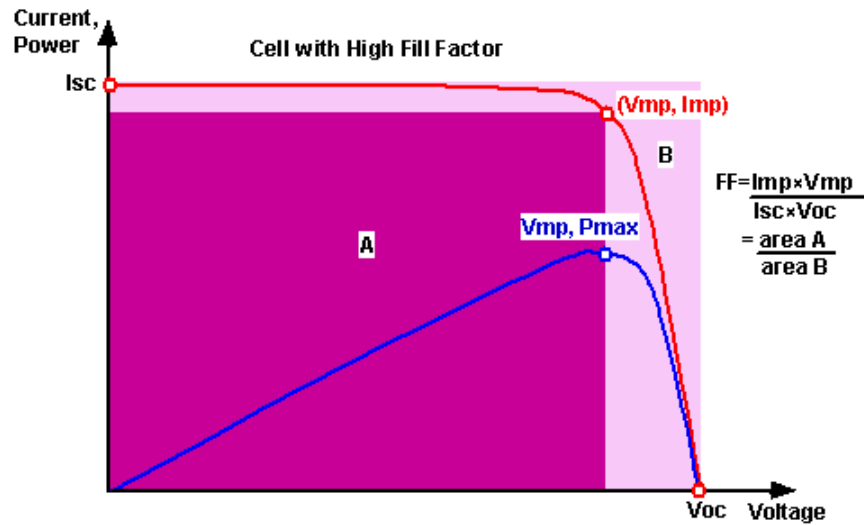


Figure 1.6: FF graphical interpretation[12]

The FF, deriving from a ratio of the same physical parameters, is a dimensionless number belonging to the interval between 0 and 1. It is a function of  $R_s$  and  $R_{SH}$  (series and shunt resistances). To obtain the higher FF is really important to ensure high performances from the solar cell thus, to reach this goal, it is fundamental to have the lowest  $R_s$  and the highest  $R_{SH}$  possible. Another way to improve this parameter is by minimizing the overvoltage due to diffusion and charge transfer processes. A typical value of the FF for commercialized solar cells is around 0.85 (visit [pveducation.org](http://pveducation.org) for more details).

## Efficiency

Efficiency is one of the most important parameters to make comparisons between different solar cells and to evaluate quantitatively their performances. It is defined as the ratio between the power output from the solar cell and the incident power from the sun and it is generally expressed in percentage. From equation 1.4 it is possible to derive

$$P_{OUT} = V_{OC} \cdot I_{SC} \cdot FF$$

and thus the efficiency  $\eta$  is given by:

$$\eta = \frac{V_{OC} \cdot I_{SC} \cdot FF}{P_{in}} = \frac{P_{out}}{P_{in}} \quad (1.5)$$

It is to be remarked that efficiency, besides being a function of the solar cell itself, depends on many other parameters, such as: incident solar spectrum, temperature, light intensity. Therefore, it is important to specify the conditions under which efficiency is calculated. Standard conditions for terrestrial solar cells efficiency measurements are under AM1.5G solar spectrum and at a temperature of  $25^{\circ}C$ . AM0 solar spectrum conditions are used for solar cells used in space applications.

## Quantum efficiency

Quantum efficiency is a parameter that gives a measure of how efficient the solar cell is in converting the incident photons into a photo-generated current. More in details, it is the ratio between the number of charge carriers generated by the solar cell and the number of photons of a given incident energy. It is expressed as a function of the wavelength( $\lambda$ ) or of the energy( $\nu$ ). If for every incident photon at a particular wavelength the resulting charge carriers are collected then the quantum efficiency at that  $\lambda$  is unitary. On the other hand, the quantum efficiency for photons that have an energy lower than the energy gap is zero. Quantum efficiency can be divided

into external quantum efficiency(EQE), sometimes also called Incident Photon to Charge Carrier Efficiency(IPCE), and internal quantum efficiency(IQE). The former takes into account the effect of reflectivity while the latter only considers photons that are neither reflected nor transmitted out of the solar cell. EQE and IQE can be,thus, defined as reported in the equations below:

$$EQE = \frac{Electrons_{out}}{Photons_{in}} \tag{1.6}$$

$$IQE = \frac{EQE}{1 - R} = IQE = \frac{Electrons_{out}}{(Photons_{in})(1 - R)} \tag{1.7}$$

Where R is the reflection coefficient from the top surface. For the sake of completeness, a quantum efficiency curve for an ideal solar cell is reported in Fig.1.7. As usual, it has been taken from "pveducation.org" website [13].

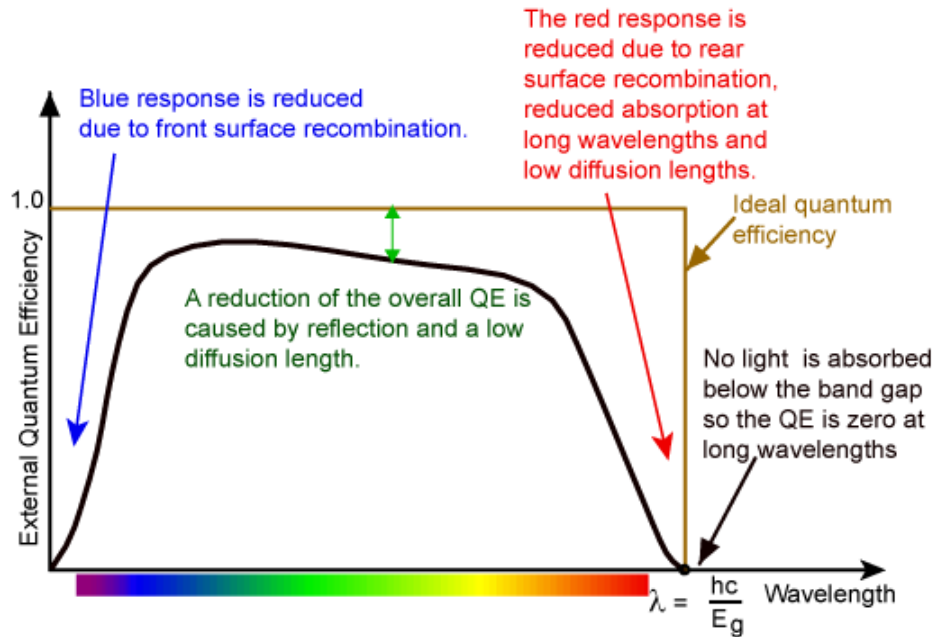


Figure 1.7: Quantum Efficiency [13]

It is to be remarked that for a DSSC, that is the type of solar cell that will be considered in this master thesis, EQE is defined as in 1.8(see [10])

$$EQE(\lambda) = LHE(\lambda) \cdot \phi(inj) \cdot \eta(coll) \quad (1.8)$$

where, LHE( $\lambda$ ) is the so called light-harvesting efficiency of photons at a wavelength  $\lambda$ ,  $\phi(inj)$  is the electron injection quantum yield from the excited dye to the conduction band of the semiconductor oxide and  $\eta(coll)$  is the percentage of injected charge carriers that reach the back contact.

### 1.2.3 Light-matter interaction basics

In order to better understand and clarify the aforementioned concept regarding the external quantum efficiency it may be useful to devote a few lines considering some basics of light-matter interaction. It is known that when a photon is incident at low energies(single eVs), which are typical for visible light, it interacts primarily with valence electrons. The interaction of visible light with matter can be described by means of the so called "refractive index"  $n$  which is, in general, a complex number.  $\hat{n}_c = \hat{n} + i\hat{k}$ . The real part of the refractive index  $\hat{n}_c$  is related to phase velocity while the imaginary part is related to attenuation. To measure  $\hat{n}$  and  $\hat{k}$  the spectroscopic ellipsometry technique is typically used.

Now, considering the reflection of light from a bare semiconductor, in case of normal radiation incidence from air, the reflection coefficient is given by the following formula [14]:

$$R = \frac{(\hat{n} - 1)^2 + \hat{k}^2}{(\hat{n} + 1)^2 + \hat{k}^2} \quad (1.9)$$

It can be seen that at visible  $\lambda$  the fraction of reflected light depends most

strongly on the real part of  $\hat{n}_c$ . To conclude this brief review on light-matter interaction it is important to recall the Beer-Lambert law which relates the attenuation of light depending on the material through which the light is travel. The expression of the Beer-Lambert law is given in equation 1.10

$$I = I_0 e^{-\alpha l} \quad (1.10)$$

where  $I$  is the intensity of the light leaving the sample,  $I_0$  is the intensity of the light entering the sample,  $\alpha$  is the absorption coefficient and  $l$  is the pathlength. An intuitive graphical representation of Beer-Lambert law is given in Fig. 1.8 taken from [15]

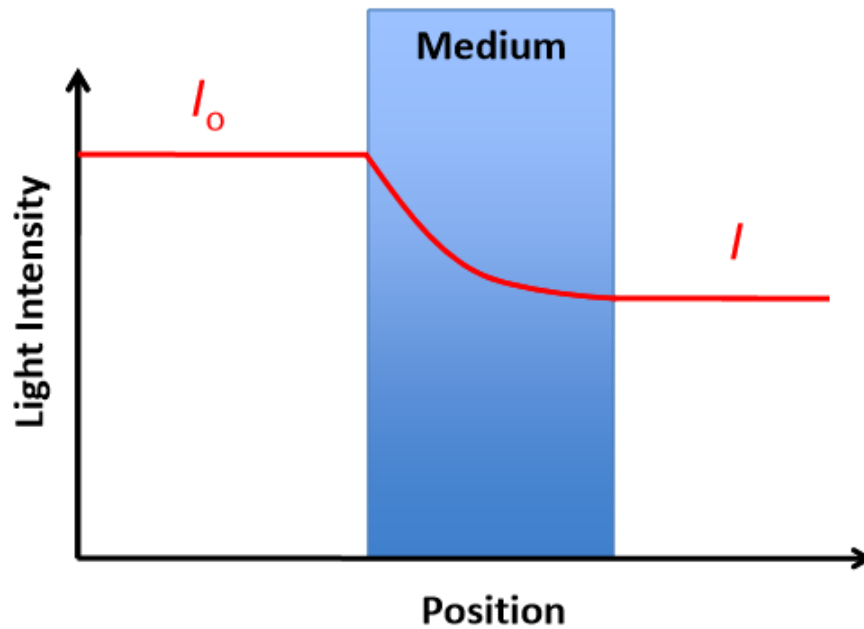


Figure 1.8: Beer-Lambert law [15]

### 1.3 Dye-Sensitized-Solar-Cells

Dye-sensitized solar cells are among the most promising technologies in the third generation photovoltaics scenery. They were first built in 1991 by B. O'Regan and M. Grätzel at EPFL having an efficiency  $\eta = 7.1\%$  and an  $EQE \approx 80\%$  [16]. Nowadays, the efficiency of DSSCs is slightly above 10% which is considered as the minimum required efficiency for commercial applications. In particular, dye-sensitized cells show their potential in domestic devices where low cost and easy fabrication is a great advantage with respect to Si-based solar cells and their low efficiency is not a dramatic shortage.

DSSCs working principle is similar to photosynthesis. In fact, the mesoporous semiconductor (usually  $TiO_2$ ) plays the role of thylakoid vesicles in plants leaves while the adsorbed dye, which injects the electrons in the semiconductor conduction band, behaves like the chlorophyll [17]. A DSSC, therefore, is a photochemical device whose constitutive elements are the following:

- A transparent anode which consists of a glass sheet covered with FTO (fluorine doped tin oxide), a transparent conductive oxide layer.
- A mesoporous wide band gap semiconductor, anatase  $TiO_2$  is the most used one and will also be used in this master thesis. It is deposited on the anode to establish electronic conduction.
- A monolayer of the molecular sensitizer (dye), usually a ruthenium polypyridin complex such as the N-719 dye, which is the one that absorbs light and injects the electron in the conduction band of the  $TiO_2$ . It is covalently bounded to the mesoporous semiconductor oxide layer.
- An electrolyte, usually a iodide/triiodide-based electrolyte with acetonitrile as the organic solvent, which acts as the redox mediator and regenerates the

oxidized dye.

- A platinum layer deposited on the FTO coated glass sheet which catalyzes the iodine reduction and closes the electrical circuit. It is the cathode of our device.

More details on the experimentally used materials are described in chapter 2. Fig. 1.9 taken from [17] gives a pictorial view of the basic DSSC structure and operational principle.

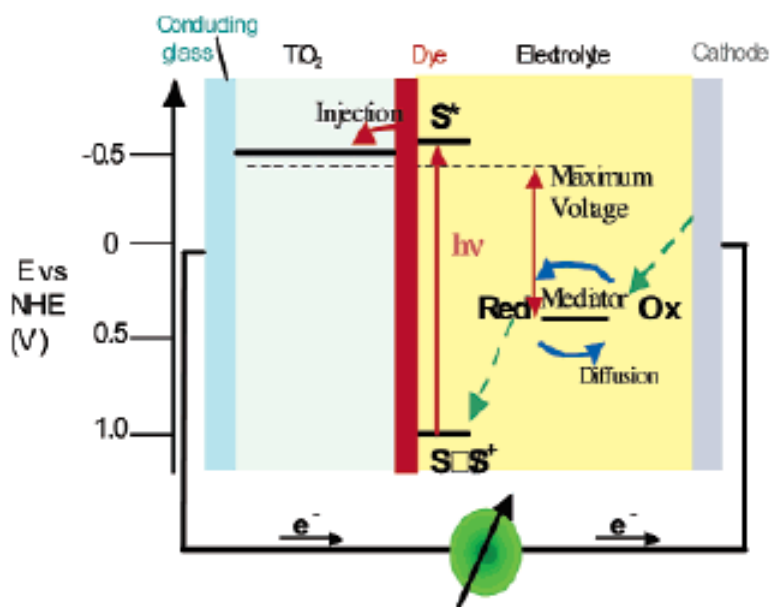


Figure 1.9: DSSC structure and working principle[17]

It can be seen that the ideal working scheme of a DSSC can be summarized in the steps reported below:

- The incident photon reaches the dye absorbed on the semiconductor surface
- The dye promotes one electron from HOMO(highest occupied molecular orbital) to LUMO(lowest unoccupied molecular orbital)

- The electron is injected in the  $\text{TiO}_2$  conduction band with a time constant  $\tau \approx 10^{-12}\text{s}$ [18]
- The electron diffuses through the semiconductor oxide to the FTO anode  $\tau \approx 10^{-3}\text{s}$ [2]
- The electron enters the external circuit performs a useful work and then is collected by the Pt counter electrode reducing the iodine in the electrolyte according to reaction 1.11(  $\tau \approx 10^{-5}\text{s}$ [2]):



- The oxidized dye recovers its lost electron from the reduced iodide in the electrolyte according to the following chemical reaction( $\tau \approx 10^{-6}\text{s}$ [2]):



At this point, having replenished the HOMO of the dye, we are back to the initial condition and ready to start a new cycle.

Figure 1.10, taken from [2], represents the main electron transfer processes considering both the ideal and the non-ideal behavior in the DSSC working mechanism. In fact, the numbered arrows 1, 5, 6 represent the basic loss reactions. In particular, reaction one represents the undesired HOMO-LUMO direct recombination of the electron promoted from the dye, reaction five is the recombination between the electron injected in the  $\text{TiO}_2$  and the oxidized dye and finally reaction six is the recombination between the electron injected in the mesoporous semiconductor and the electrolyte. It is to be noted that the recombination between the electron in the  $\text{TiO}_2$  and the electrolyte can happen both at the interface between the electrolyte

and the semiconductor and at the interface between the electrolyte and the FTO layer. That is why the use of some "blocking-layers" deposited on the oxide and the FTO can be useful to increase the photogenerated current and therefore to improve the FF and the efficiency.

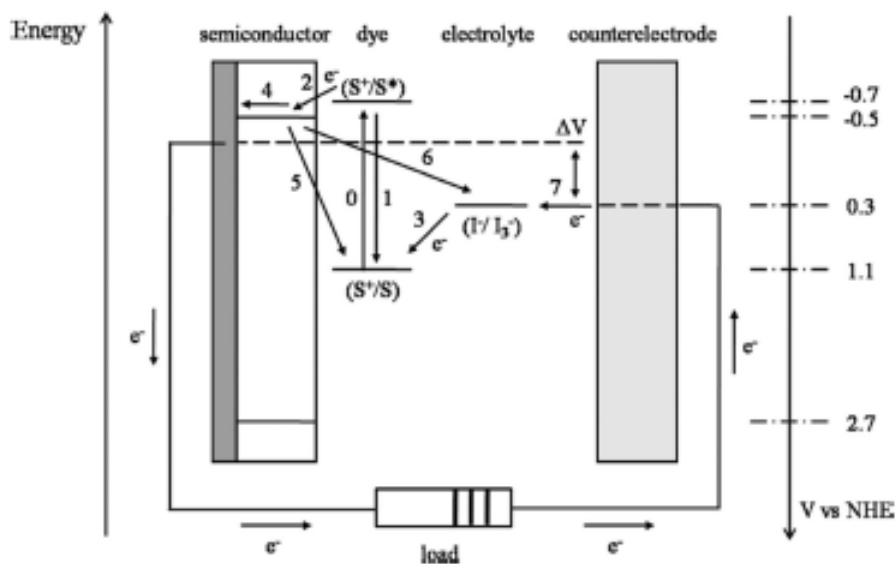


Figure 1.10: DSSC electron transfer processes[2]

The  $\Delta V$  term in Fig. 1.10 indicates the open circuit voltage of the cell which is given by the difference between the (quasi)Fermi level of the mesoporous semiconductor and the Nernst(redox) potential of the electrolyte. It is approximately equal to 0.7 V under solar illumination conditions. Fig. 1.11,(taken from [2]),instead, shows the same electron transfer processes of the previous one, but adds some information about the order of magnitude of the time constants involved. It can be easily seen that the time constants of the recombination mechanisms are much bigger than the ones of the desired processes and so they play a minor role in the DSSC operation, but still they are present and represent a key marker in evaluating how good the performance of a cell are.

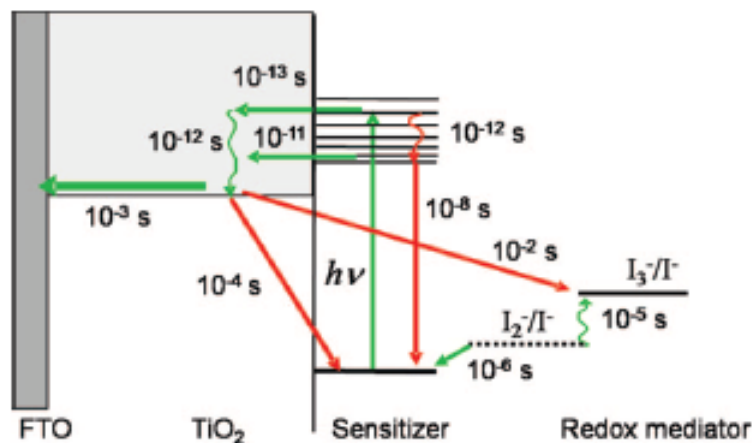


Figure 1.11: DSSC electron transfer processes and time constants[2]

## 1.4 Supercapacitors

Energy storage technologies have undergone a dramatic spur in the last decades in parallel to energy harvesting techniques. In fact, it is evident that, besides generating energy, it is of utmost importance to be able to store it in a safe and stable way [19]. Among these energy storage systems a key role is played by the so called "supercapacitors", whose widespread industrial production dates back to 1978[20]. They are a particular type of electrochemical devices. Supercapacitors have filled the "gap" left by previous energy storage technologies. In fact, they have features that are intermediate between standard electrolytic capacitors and batteries. More in details, supercapacitors can store energy with a density that is 10-100 times greater than the standard capacitor one [21], but smaller compared to battery energy density. On the other hand, supercapacitors are able to provide a lot of energy in a short time (high power density), unlike batteries, but of course their power density is not so high as the standard capacitors one. To show this in a graphical way a Ragone chart, which plots power density vs energy density for different storage

technologies, is reported in Fig.1.12 taken from [19]

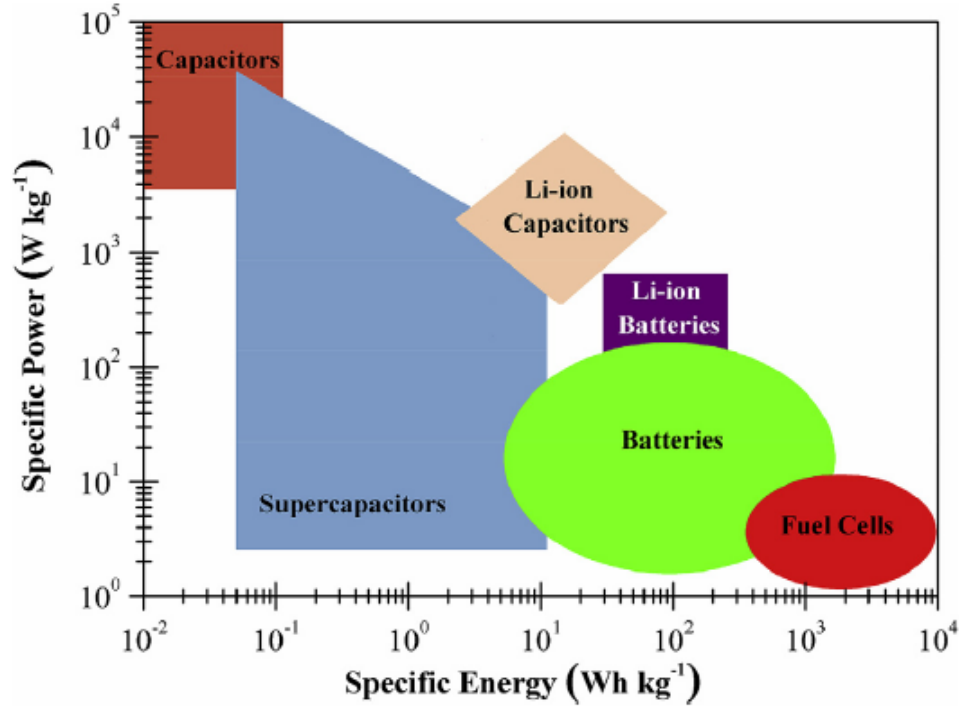


Figure 1.12: Ragone chart[19]

Supercapacitors are, in general, made up of the following elements:

- two electrodes(anode and cathode) which should be properly engineered in order to maximize the specific surface area(SSA), a key parameter that is related to the number of charges on the electrodes surface, increasing the overall capacitance of the device.
- an electrolyte which substitutes the dielectric of an ordinary capacitor.
- a separator that allows ionic conduction through the electrolyte, but prevents shorts between the two electrodes.

A basic picture of the generic structure of a supercapacitor is reported in Fig.1.13, taken from [21]:

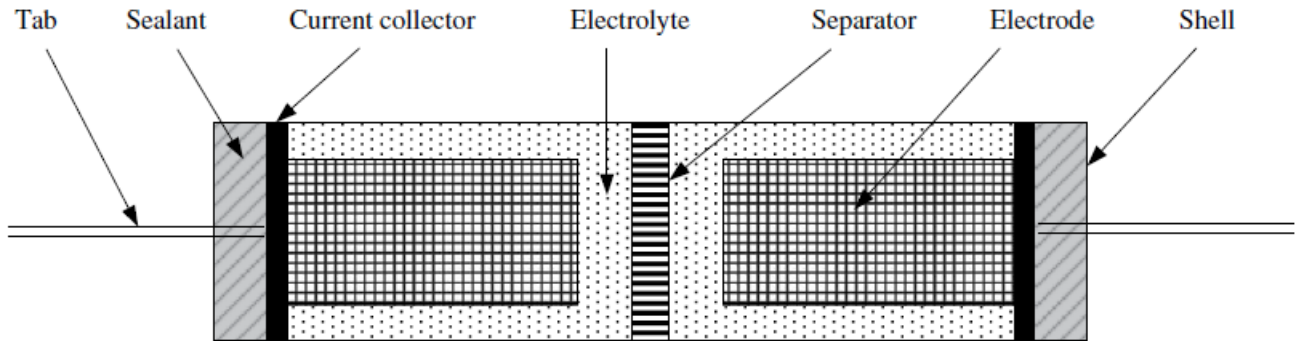


Figure 1.13: Supercapacitor generic structure[21]

According to the charge storage mechanism, supercapacitors can be divided into three categories:

- electrical double-layer capacitors(EDLCs)
- pseudocapacitors
- hybrid capacitors(a combination of the previous two types)

It is to be noted that both the electrical double layer capacitance and the pseudocapacitance contributions are always present in a supercapacitor. By the way, we say that a supercapacitor belongs to one category or the other depending on what is the dominant contribution to its capacitance. EDLC is the fundamental charge storage mechanism of supercapacitors[22]. The idea behind this principle is easy to be understood starting from some considerations on ordinary capacitors. It is well known that  $q = C\Delta V$  and that for a parallel plate capacitor  $C = \frac{\epsilon A}{d}$  where A is the surface of the electrodes,  $\epsilon$  is the dielectric constant and d is the distance between the two electrodes. It is therefore clear from the previous two equations that in order to increase the capacitance the charge and the surface of the electrodes should be increased, while the distance should be decreased as much as possible. This is

the principle exploited in EDLCs, where we have the two electrodes immersed to an electrolyte. By biasing the electrodes with an external source, ions of the opposite charge from the electrolyte build up at the electrode/electrolyte interface in order to achieve electroneutrality. In this process no charge transfer is present between the electrode and the electrolyte, so it is a true capacitive effect. The thickness of the double layer, which corresponds to the  $d$  of a parallel plate capacitor, where one layer is made up of the charges on the surface of the electrode and the other layer consists of the ions at the electrolyte/electrode interface, is about 10-15 Å for concentrated electrolytes and depends on the dimensions of the ions and on the ion concentration in the electrolyte. The typical values for the capacitance per unit area of the double layer are in the range 10-15  $\frac{\mu F}{cm^2}$  considering smooth electrodes and concentrated electrolyte.[21]. The phenomenon of the double layer capacitance have been first observed and described by Helmholtz in 1879. He provided a simple model for it made up of two series connected capacitors. Fig.1.14, taken from [20], gives a pictorial view of the Helmholtz electrical double layer in order to better clarify the concept.

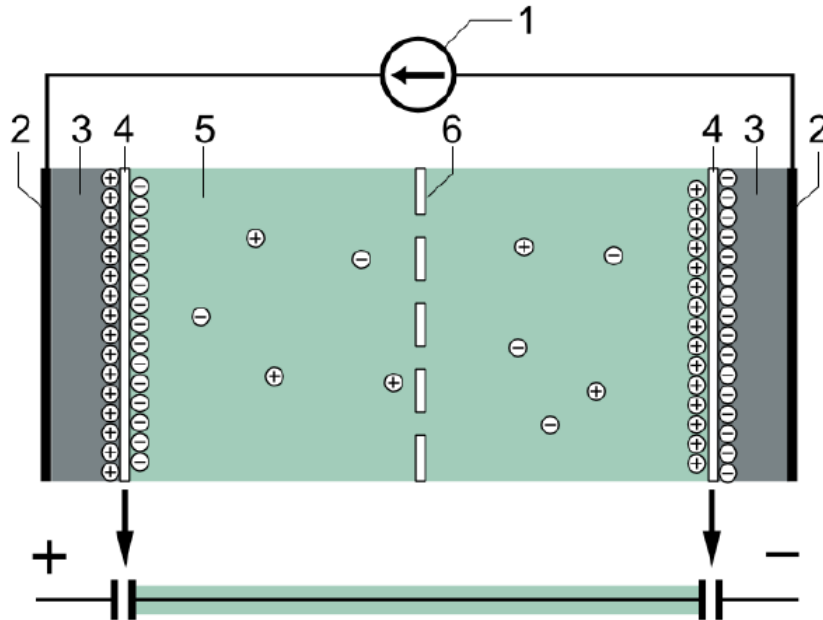


Figure 1.14: Helmholtz double layer[20]

- 1) external source
- 2) current collector
- 3) electrode
- 4) electrode/electrolyte interface
- 5) electrolyte
- 6) separator

As regards pseudocapacitive effects, instead, they are due to Faradaic charge transfers between the electrodes and the electrolyte such as: redox reactions, incanalation and electrosorption. Compared to EDLC, pseudocapacitors show much higher values of capacitance per unit area ( $\approx 2000 \frac{\mu F}{cm^2}$ ), but has not a so good dynamics in terms of charge/discharge processes[21]

### 1.4.1 Materials for supercapacitors

As it was stated before, the two electrodes, the electrolyte and the separator are the constitutive elements of a supercapacitor. A brief description of the most common materials employed for these purposes is reported in the lines below.

As regards the electrodes, they are made up of a metal foil (typ. Aluminium), which is the current collector, and the active material placed on the metal which is used to increase the SSA. A binder (typ. a polymeric material) is also used to allow the adhesion of the active material on the metal. With respect to the active material, there are three main categories used: carbon based, transition metal oxides and conductive polymers. Carbon based materials are widely employed in EDLC. The most common ones are active carbon, carbon aerogels, carbon nanofibers and nanotubes. They have had a great success because of their many positive features such as: relatively low cost, easy fabrication steps, high chemical stability, wide temperature range and non toxicity[21]. In particular considering active carbon(AC), which is a quite popular solution in EDLCs fabrication, the SSA of the electrode is increased because of the porous structure of the material. Thus, an important parameter to be engineered is the so called "pore size distribution" (PSD). In fact, it can be seen that micropores( <2nm wide) are good to obtain high capacitance but show a quite slow charge/discharge, while to improve the high rate performances mesopores(2-50nm wide) are more suitable[21].

To exploit the pseudocapacitive faradaic effect, instead, transition metal oxides and polymers represent a very good choice for the electrodes materials. Concerning the formers,  $RuO_2$  plays a key role because of its high specific capacitance, good high rate performances and long cycle life. However, due to Ru lack of abundance and high cost, some alternative materials such as  $MnFe_2O_4$ , NiO and, above all,  $MnO_2$  are also used. In fact, manganese is among the cheapest and most eco-friendly transition metals, even though its high rate performance are not excellent. Considering

polymers, on the other hand, they show high specific capacitance, easy manufacturing, low cost, but a bad long term stability during cycling. In fact, it was observed that electroactive polymers undergo swelling and shrinking during cycling. [21]

As long as the electrolyte is concerned, they define the voltage range of the device and also the possible stored energy. An ideal electrolyte should have the following characteristics [23]:

- electrochemical stability of the electrolyte
- low viscosity (related to high ion mobility) and high conductivity in a large range of operating temperature in order to have a fast and efficient storage process.
- low melting point and high boiling and flash point
- low cost and low toxicity

Commercial electrolytes are mainly aqueous or organic based. The formers show high conductivity and low cost but limit the unit cell voltage to about 1V [22] reducing the available energy dramatically. Organic-based electrolytes, instead, undergo more complicated fabrication steps and are more expensive, but they allow an operating voltage of about 2.7-2.8 V in a relatively wide temperature range. They usually consist in 1 M solution of the salt tetraethylammonium tetrafluoroborate ( $Et_4NBF_4$ ) in acetonitrile (ACN). Propylene carbonate (PC) is sometimes used instead of ACN as a solvent. To make the supercapacitor working at even higher voltages, it is mandatory to think about alternative conductive salts and solvents such as glutaronitrile (GTN) or adiponitrile (ADN) thus reaching  $\approx 3.5$  V [23].

Finally, as regards the separator, it should allow the ionic conduction, but avoid shorts between the two electrodes, as it was previously stated. There are mainly two types of separators that can be used depending on the type of electrolyte chosen:

polymeric and cellulose fibers separators are mostly employed with organic based electrolytes, while glass fibers and ceramic separators are mainly used with aqueous electrolytes[20]. A lot of research has been carried out in order to engineer and improve the separator performance([24] can be seen as an example). It should be also said that the separators used in supercapacitors can be also exploited in electrochemical batteries.

For this master thesis project purposes a 33 mF commercial supercapacitor by AVX BZ series has been used. it shows a very large potential window(5.5 V, suggesting the series connection of more cells) and a wide operating temperature range. More details about this supercap can be found on the AVX website[25].

### 1.4.2 Supercapacitors: performance evaluation

To evaluate the performances of a supercapacitor many different parameters can be taken into account. However, it is possible to consider a small set of parameters from which we can assess the devices behaviour in terms of their energy and power features[26]. They are nominally: the total capacitance of the device( $C_T$ ), the operating voltage( $V_O$ ), the equivalent series resistance( $R_S$ ) and the coulombic efficiency(CE). The total capacitance of the device is the result of an electrical charge stored under a given potential difference. In fact, as it is well known  $C_T = \frac{\Delta Q}{\Delta V}$ . To better define the intrinsic storage ability of the SC materials, instead, it is preferable to define the specific capacitance  $C_S = \frac{\Delta Q}{\Delta V \Pi}$  where  $\Pi$  can be the volume, the mass, the surface area of the electrode material, the electrode size[26]. These capacitances values can be calculating using different measuring techniques such as: electrochemical impedance spectroscopy(EIS), cyclic voltammetry(CV), constant current charge discharge(CCCD)... that will be briefly described in next section. The operating voltage, instead, is referred to the proper potential window within which the device normally operates.  $V_O$  can be measured by using both CV or CCCD and it is a

function of the device configuration (symmetric, asymmetric system...) and of the type of the electrolyte used.

As concerns the equivalent series resistance, it represents the internal resistance that dissipates the energy that is stored in the SC. It is better to minimize  $R_S$  in order to have a better electrochemical behaviour. This resistance can be computed by using CCCD and applying Ohm's law to the IR drop at the initial stage of the discharge process ( $R_S = \frac{\Delta V}{\Delta I}$ ). Finally, considering the coulombic (or faradaic) efficiency, it is a description of how much effectively charges are transferred to the supercapacitor. It is given by the expression 1.13 taken from [27]:

$$CE = \frac{100 \cdot Q_{discharge}}{Q_{charge}} \quad (1.13)$$

Or, supposing to have performed a CCCD test, equation 1.14 can be used:

$$CE = \frac{100 \cdot time_{discharge}}{time_{charge}} \quad (1.14)$$

To conclude this brief description of supercapacitors characteristics, a list of their main advantages will be presented in order to give a synoptic view of these devices.

- They have a higher power density with respect to batteries and a higher energy density with respect to standard electrolytic capacitors.
- They can work in a wide temperature range  $\approx [-50, 200]^\circ C$  [19].
- Safe and easy to recycle.
- About same cost of the other main storage technologies.
- Lower heat generation thanks to its simpler charge storage mechanism. [26]

- Very long cycle life(> 1000000 cycles) with respect to batteries(2000-3000 cycles)[26].
- Supercapacitors, unlike batteries, can easily adapt to the voltage they are receiving and this implies that they can work well with renewable resources.

## 1.5 Electrochemical Impedance Spectroscopy, Cyclic Voltammetry and Galvanostatic Charge-Discharge: Basics

### 1.5.1 Electrochemical Impedance Spectroscopy

Electrochemical impedance spectroscopy(EIS) is a very effective and widely used electrochemical analytical technique. It has been proved to be a very powerful tool to analyze many DSSCs properties that are still not fully understood, such as the charge transport through the oxide or the electron injection process, as well as to characterize the different materials of the device. EIS is used when the material under test shows a prevailing ionic conduction on the electronic one. It consists in the application of an AC voltage(an AC current is used in the case of galvanostatic EIS) to the device under test and in the detection of the related AC current(voltage) response as a function of the frequency. It can be performed using two or three electrodes. In the latter case, a reference electrode whose potential is known and fixed is present. In order to get reliable results from EIS four conditions should be met[28]. They are namely linearity, causality, stability and finiteness. Linearity means that the I-V curve of the system should be linear, with a certain grade of approximation, in the region of interest. Causality, instead, implies that the response of the device depends only on the AC input and not from any other external

”noise”. Stability requires the system to be in a stationary state until the AC input is applied and then, when the stimulus is not active anymore, go back to the initial state. Finiteness, finally, requires the real and the imaginary part of the measured impedance to be finite. The complex impedance, which is the output of the EIS measurement, is given by the ratio of the small signal AC voltage  $V(\omega,t) = V_0 \sin \omega t$  (it is important to note that in order to stay in the small signal approximation conditions the  $V_0$  value should be chosen properly and usually must not exceed a few mVs) and the measured current according to Ohm’s law:  $Z(\omega,t) = \frac{V(\omega,t)}{I(\omega,t)}$ . Being a complex number, the impedance  $Z(\omega,t)$  can be represented in two ways:

1.

$$Z(\omega,t) = Z'(\omega,t) + jZ''(\omega,t) \quad (1.15)$$

2.

$$Z(\omega,t) = |Z|e^{j\theta} \quad (1.16)$$

where  $Z' = |Z|\cos\theta$  and  $Z'' = |Z|\sin\theta$  are the real and the imaginary part of  $Z$  and  $\theta$  is the phase shift between voltage and current. As it is known from basic complex numbers theory:  $|Z(\omega)| = \sqrt{Z'^2(\omega) + Z''^2(\omega)}$  and  $\theta(\omega) = \tan^{-1}(\frac{Z''(\omega)}{Z'(\omega)})$

According to equations 1.15 and 1.16 just written, there are also two ways to plot the values of the impedance  $Z(\omega)$ . The first way is the Nyquist plot where the y axis represents  $Z''$  and the x axis represents  $Z'$ . In this way we have condensed all the information of the complex number in one graph, but we have lost the ”immediate contact” with the angular frequency  $\omega$ . In the second case, the complex number is plotted using two graphs(Bode plots): one for the logarithm of the module and one for the phase both as functions of the logarithm of the frequency  $f$ (remembering that  $\omega = 2\pi f$ ). In this last case, with respect to the Nyquist plot, we have two graphs instead of one, but a direct connection between  $|Z|, \theta$  and frequency. An example of Nyquist and Bode plots is reported in Fig. 1.15 and 1.16 respectively. In particular,

they represent the results of an EIS procedure applied on a DSSC. Both pictures have been modified from [28].

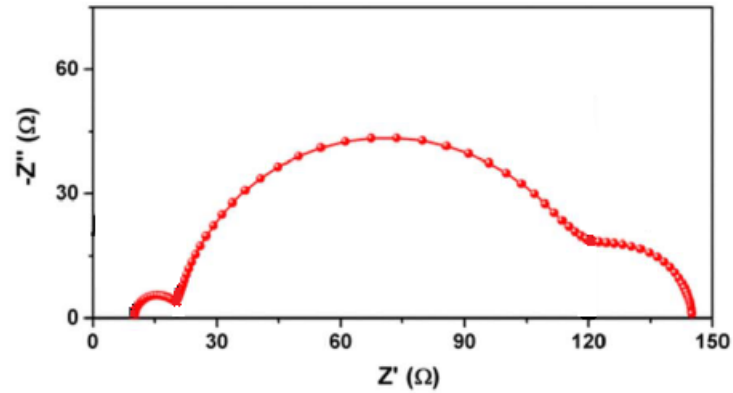


Figure 1.15: Nyquist plot DSSC

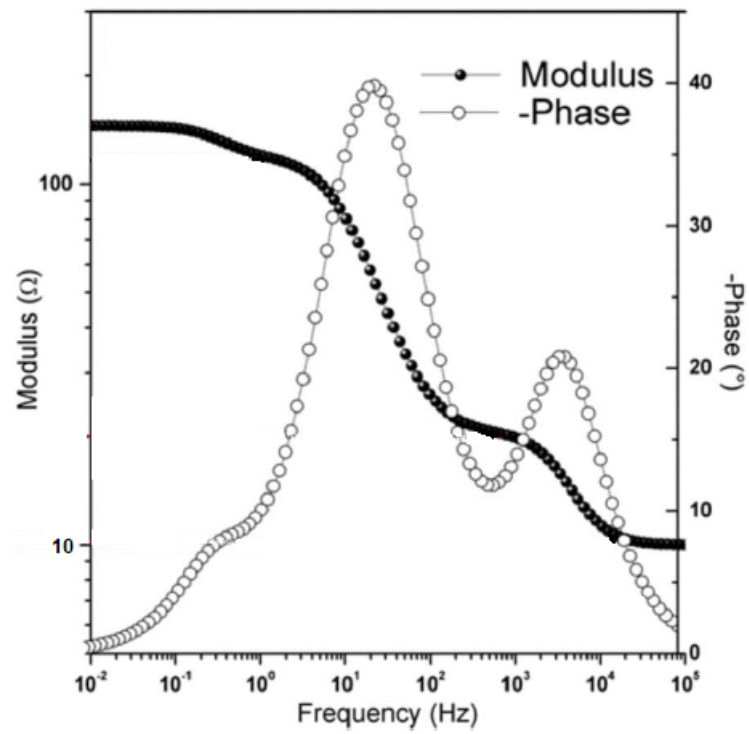


Figure 1.16: Bode plots DSSC

It is useful to derive relatively simple equivalent electrical circuits of the electrochemical systems that undergo the EIS test in order to have a model that tries to fit the experimental values. For the sake of simplicity, the impedances and phase shifts of the most used electrical elements are reported in table 1.1:

Table 1.1: Electrical elements impedances and phase shifts

Element	Impedance	Symbol	Phase Shift(rad.)
Resistor	R	R	0
Capacitor	$\frac{1}{j\omega C}$	C	$\frac{-\pi}{2}$
Inductor	$j\omega L$	L	$\frac{\pi}{2}$
Constant Phase element	$\frac{1}{Q(j\omega)^\beta}$	Q	$\frac{-\beta\pi}{2}$
Warburg	$\frac{W}{\sqrt{j\omega}}$	W	$\frac{-\pi}{4}$
Warburg Short	$R_d \sqrt{\frac{\omega_d}{j\omega}} \tanh(\sqrt{\frac{j\omega}{\omega_d}})$	$W_s$	

Where Q is the so called CPE prefactor,  $\beta$  is a number comprised between 0 and 1 called CPE index, W is the Warburg parameter and  $R_d, \omega_d$  are namely the diffusion resistance and the diffusion characteristic frequency. It is to be noted from 1.1 that, besides the three basic circuitual elements, other three devices have been added in order to modelize better the electrochemical behaviour. More in details, CPEs represent the generalization of ordinary capacitances (In fact, when  $\beta = 1$  the CPE degenerates in a capacitor) and they are used when porous interfaces are present in the system in order to take into account frequency dispersion[28]. Warburg elements, instead, have been introduced to modelize the Nernst diffusion. In particular, simple Warburg element are of interest when a semi-infinite diffusion is considered; otherwise, if it is the case of a finite length diffusion, a Warburg short

element is used.

### 1.5.2 Cyclic Voltammetry

CV testing is an analytical technique that consists in the application of a linearly and cyclically changing voltage within a range, called "potential window", between the two electrodes (for a two electrodes procedure) or between the two electrodes and a reference in the three electrodes configuration[26]. The speed of the voltage variation is reported in  $\text{mVs}^{-1}$  and is called scan rate  $\nu$ . A graphical exemple of the voltage as a function of time applied in CV is given in Fig. 1.17 taken from [29]

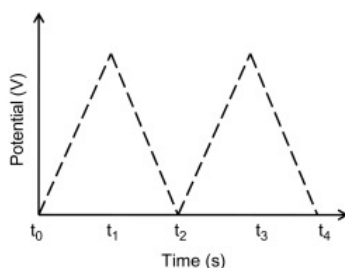


Figure 1.17: Potential profile CV[29]

As a response to the applied voltage, a related current is measured and therefore the I-V curve can be plotted observing a hysteresis cycle called cyclic voltammogram. These cycles can be repeated many times. This electrochemical technique is usually used to study redox processes and to analyze electrochemical reactions between ions and surface atoms of electrodes[30]. CV can be applied to supercapacitors to determine their potential window and their capacitance. In particular, the former can be obtained by initially applying a lower voltage to the device that should be slowly increased until a spike can be observed at the edge of the potential window. As regards the capacitance, it is to be stated that, under the hypothesis of a linearly changing charge with the applied potential, its value is perfectly constant and the cyclic voltammogram has a pure rectangular shape. Thus, the well known

equations for energy( $W$ ) and maximum power density( $P_{in}$ ) 1.17 and 1.18 can be used [23].

1.

$$W = \frac{CV^2}{2} \quad (1.17)$$

2.

$$P_{in} = \frac{V^2}{4R} \quad (1.18)$$

Where  $C$  is the capacitance,  $V$  the applied voltage and  $R$  the equivalent series resistance. As a matter of fact, in the experimental case, the shape of the voltammogram is definitely not rectangular. However, it is clear that the area of the hysteresis cycle is directionally proportional to the accumulated charge and therefore to the capacitance. It can be seen that a high scan rate leads to a big area, while a low scan rate to a small area. On the other hand, it is to be stated that the specific capacitance decreases with the increase of the scan rate, thus opposing the previous effect. This is due to the fact that, when I have a low scan rate, charges will have more time to accumulate in the porous material reaching the end of the pore; otherwise, with a high scan rate, this would not be possible.

The expression of the total capacitance of the cell is given by equation 1.19 as reported in [26]

$$C_{cell} = \frac{Q}{2V} = \frac{1}{2V\nu} \int_{V^-}^{V^+} i(v)dv \quad (1.19)$$

Finally, Fig.1.18, taken from [31], plots an exemple of cyclic voltammetry showing the curves shape variation as a function of the different scan rates.

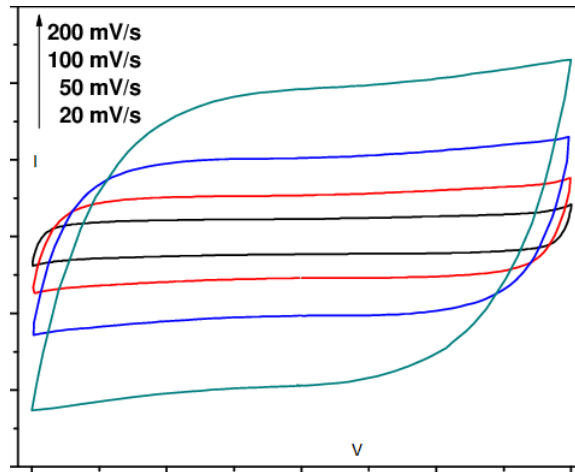


Figure 1.18: CV different scan rates[31]

### 1.5.3 Galvanostatic Charge-Discharge

This method, also called CCCD (constant current charge discharge), implies a charge-discharge cycle for the device performed at a constant fixed current. As it is known from basic physics, plotting the voltage across the capacitor as a function of time, in the ideal case, a triangular-shaped curve is expected to be obtained. As a matter of fact, the experimental data would never be exactly triangular, strictly speaking. CCCD can be also used to measure the supercap capacitance and consequently to compute the energy and the maximum power density. In fact, it should be remembered that, according to the constitutive relation of capacitors,  $C = \frac{I\Delta t}{V}$  from which we get  $E = \frac{CV^2}{2}$  and  $P = \frac{E}{\Delta t}$  where  $\Delta t$  is the discharge time.

Galvanostatic techniques are an important tool to study and understand many different properties of supercapacitors. An example is reported in Fig. 1.19 that shows a constant current discharge curves for three main storage devices, namely a supercapacitor, a battery and a standard capacitor.

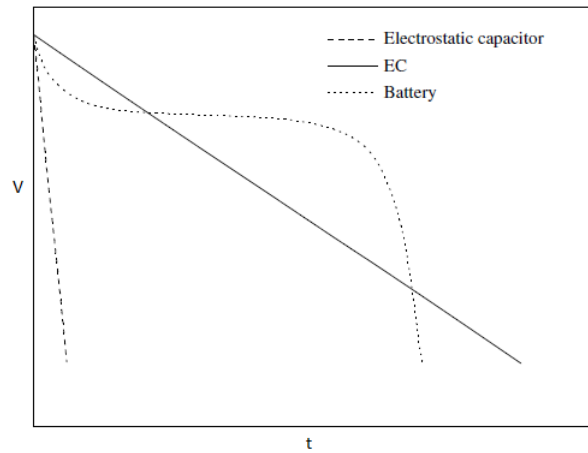


Figure 1.19: Galvanostatic discharge for different storage devices[21]

It can be seen that the battery curve has a discharge plateau, which means that the voltage keeps constant. This is due to the fact that the potential is defined by the electrochemical behaviour of the battery. For the supercapacitor and the electrostatic capacitor, instead, the discharge curves are similar. In fact, they are both linear, but of course with a different slope due to the different capacity values [26].

## 1.6 A Dssc-supercapacitor power-pack system

The huge growth of sensors industry combined with the increasing need for long term off-grid power have been a constant trend of the last few years[32]. Moreover, renewable power generation is dramatically limited by the uncertainty on the source availability. Thus, an intense research activity has been devoted to the development of integrated energy harvesting and storage(HS) portable devices, especially for low power electronics[33]. This system should be able to provide energy on demand at any time of the day and wherever we are. An optimal device of this kind should have the best matching between the harvesting and the storage, adaptability, low dimensions, low cost and low toxicity. In this perspective, flexible power pack systems represent a fundamental chance as they allow a wide range of potential application such as packaging, wereable technology, automotive systems, smartphones... even though their overall efficiency is still quite low( $\approx 1.65\%$ ) with respect to the standard planar ones[33]. One of the best choices in designing the HS power-pack system is exploiting photovoltaics as the energy harvesting principle and a supercapacitor as the storage element. Among the photovoltaic technologies, DSSCs show a large set of advantages, as it has already been described in the previous section related to solar cells, such as acceptable efficiencies, low cost, relatively easy fabrication steps and the possibility to work under low illumination conditions thanks to the photoinduced charge separation that can happen with light of energy lower than the band gap one[34]. In the same way, supercapacitors have a certain number of advantages on batteries (higher power density, more charge-recharge cycles, less generated heat...) that have been already analyzed before in this chapter. In order to meet real world energy requirements, HS devices having an operating voltage greater than a single cell  $V_{oc}$  are needed[35]. That is why a module consisting in six DSSCs connected in series in the so called "W-configuration" has been developed and fabricated in this master thesis.

To combine the energy harvesting part with the storage one two ways can be employed: the first one is to realize the two components as two separate entities and afterwards to connect them through the proper circuitry and wiring; the second one is to physically integrate the two components, for exemple by sharing one electrode between the DSSC module and the supercapacitor. The latter choice looks very promising in order to lower manufacturing costs, weight and occupied space[36], but, on the other hand, it shows the drawback of allowing the self-discharge of the supercapacitor on the DSSC module when illumination is over and therefore it will not be the one chosen for this M.Sc. work.

Some different attempts to build DSSC-supercapacitor power-pack systems have been carried out in literature, such as [37] and [38](in the latter a module consisting in the series connection of 4 DSSCs in "W-type" configuration has been built by Scalia et Al.), obtaining overall efficiencies of 5.12% and 1.83%. It is to be noted that the aforementioned overall efficiency it is nothing but the so called "OPECSE" (overall photon to electrical conversion and storage efficiency). It is computed by means of eq.1.20[35]

$$\eta(OPECSE) = \frac{0.5CV^2}{GtS} \quad (1.20)$$

Where C is the capacitance of the supercapacitor, V is the voltage across the supercapacitor, S is the active area of the DSSC module, t is the photo-charge time, G is the electromagnetic power density produced by the sun simulator or any other light source[ $Wm^{-2}$ ][33]. Another way to express the OPECSE is according to equation 1.21 where the global efficiency of the HS device is represented by the product between the efficiency of the photovoltaic part and the efficiency of the storage part[38].

$$\eta(OPECSE) = \eta_{PV}\eta_{STORAGE} \quad (1.21)$$

# Chapter 2

## Experimental Part

### 2.1 DSSC materials

This section will briefly analyze the materials involved in the DSSC fabrication giving some basic knowledge of how material properties drive the choice of the specific constitutive elements of a DSSC and how fabrication steps affect these properties and thus the overall performances of the final solar cell.

#### 2.1.1 Oxide Semiconductor

In this master thesis project anatase  $TiO_2$  paste by Dyesol(the SOLARONIX transparent  $TiO_2$  paste has been used for the transparent photoanode DSSC module version) was chosen as the wide band gap semiconductor oxide because of its many positive features. In fact, it is characterized by a porous structure with a large surface area, a proper HOMO an LUMO alignment with the electrolyte and the dye and a wide band gap to prevent easy direct recombination. In this regard, the anatase phase has been chosen because it is characterized by a bandgap of 3.2 eV, while the rutile phase one is only 3 eV[10]. The  $TiO_2$  paste has a mesoporous structure(this means that the pore diameter is between 2 and 50 nm). The pores size is something that has to be engineerd because an increase in size leads to a reduction of  $TiO_2$  mass(and therefore of the photo-generated current), while too small pores limit the diffusion of the electrolyte. Porosity is defined as the ratio between the volume of empty space and the total volume. It is expressed in percentage. As regards the

$TiO_2$  nanoparticles, they show a nanometer size( $\approx 20-40$  nm)[39]. Their size is another key parameter that has to be optimized. In fact, larger particles imply a decrease of the electron recombination lifetime; on the other hand, the decrease of the particle size results in a lower charge injection efficiency that is due to a reduced diffusion length. It is to be noted at this point that the nanoparticles diameter is too small to build up an electric field, charge transport mechanism in the semiconductor oxide is mainly diffusive[10]. Both porosity and particles size, that have been just cited, are functions of the annealing profile that the  $TiO_2$  paste must undergo. It has been proven that with an increasing temperature, starting from  $400\text{ }^\circ C$ , the average pores size increase[10]. However, with annealing temperatures higher than  $500\text{ }^\circ C$  no-more changes in the pores dimensions are observed[40]. Moreover,  $TiO_2$  layers baked at higher temperatures show a higher  $J_{SC}$  due to an increase of the diffusion coefficient and the carrier lifetime[41].

Also the annealing temperature rise rate affects the overall performances of the devices. In fact, it has been showed that for a faster rate annealing recipe  $V_{OC}$  and the series resistance  $R_S$  are lowered, while  $J_{SC}$  is increased[10]. Finally, another parameter of great importance is the oxide thickness. In fact it was observed that a thicker layer results in an increase of the photo-generated current because of the bigger quantity of dye adsorbed by the oxide layer. On the other hand, a thicker  $TiO_2$  layer implies a longer path for the electron to be covered, thus increasing the recombination probability[10]. That is why an optimum value for the titania film should be found. A typical value for the  $TiO_2$  thickness is in the range between  $5-20\mu m$  with a mass of  $\approx 1-4\frac{mg}{cm^2}$  and a porosity of  $50-65\%$ [42]. As concerns the effect of the DSSC performances as a function of the oxide thickness, literature states that a small decrease in the  $V_{OC}$  is expected with a thicker titania layer.  $J_{SC}$  behaviour as a function of the oxide thickness, instead, depends on the electrolyte viscosity, the particles size and the surface configuration[10].

### 2.1.2 Sensitizer

The dye is the core element in a DSSC device. In fact, it is the one that injects electrons in the  $TiO_2$  layer. In this work N-719 dye, a ruthenium polypyridin complex, is used. A picture of N-719 molecular structure is reported in figure 2.1 taken from [18]:

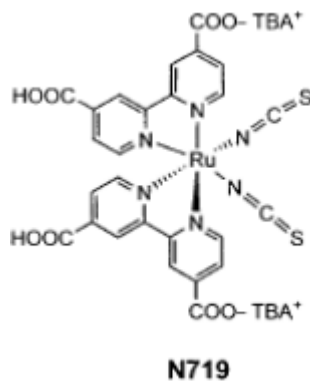


Figure 2.1: N-719 chemical structure [18]

When the dye is adsorbed on the titania film, it forms a monolayer coating with a stoichiometry of the anchored sensitizer of  $\approx 1:100$  (Ru per Ti) [10]. For the sake of clarity, the main properties of a good photosensitizer and the related features of the N-719 dye are reported here in the form of a bullet list.

- Proper HOMO and LUMO alignment: first of all, it should be remarked that in order to achieve an efficient electron injection, the LUMO of the dye should be  $\approx 0.3$  eV above the  $TiO_2$  conduction band. Moreover, the electrolyte redox potential should be also  $\approx 0.3$  eV above the homo level of the dye. It can be seen that the combination  $TiO_2$ , N-719 dye and  $I^-/I_3^-$  fulfills these requirements [43].
- Good spectral response: the absorption spectrum for N-719 sensitizer is reported in Fig. 2.2, taken from [44]. Fig. 2.3, instead, shows the absorption

spectrum for N-719 dye when adsorbed on the  $TiO_2$  electrode. It has been modified from [45].

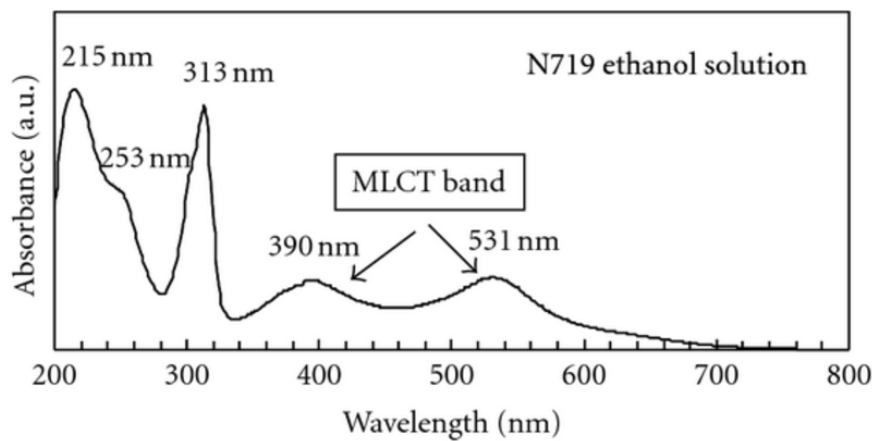


Figure 2.2: N-719 absorption spectrum[44]

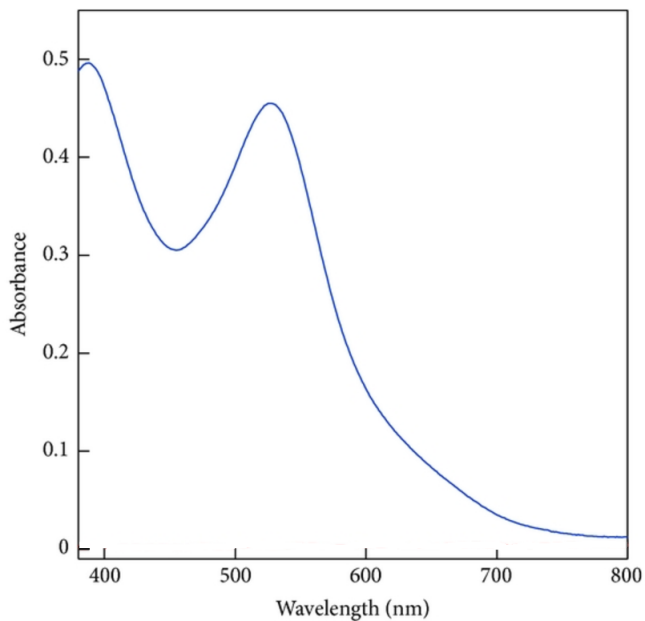


Figure 2.3: N-719 adsorbed on  $TiO_2$  electrode: absorption spectrum[45]

It can be seen that the absorbance is relatively good in all the visible light range (with significant peaks around 215nm and 313nm) a part from the near infrared wavelengths, as it has been deeply described in literature.

- Functional groups and chemical binding with  $TiO_2$ : it has been proposed by Lee et Al.[46] that the binding between the N719 dye and the  $TiO_2$  nanoparticles "occurs through two neighboring carboxylic acid/carboxylate groups because of a combination of bidentate-bridging and H-bonding that involve a donating group from the N719 (and/or Ti-OH) units and acceptor from the Ti-OH (and/or N719) groups".
- Stability: N-719, as the other Ruthenium-based dyes, exhibits good stability performances keeping the 96% of the initial efficiency even after 1000h under standard AM1.5 radiation spectrum and at a temperature of 60 °C[18]. This allows the DSSC to have a lifetime of about 20 years (i.e.  $\approx 10^8$  redox reaction cycles)[10].

### 2.1.3 Electrolyte

Iodolyte AN-50 by SOLARONIX has been used as the electrolyte for the DSSC module. It is characterized by a iodide-triiodide redox couple and a 50mM redox concentration. Acetonitrile is used as the organic solvent. Other informations can be found on the SOLARONIX official website. It shows quite low viscosity and an obtainable  $V_{OC}$  of around 0.7 V. More in details,  $V_{OC}$  is a function the iodide concentration because of the presence of a recombination reaction between the electrons in the conduction band of  $TiO_2$  and the triiodide ( $I_3^-$ ). This is quantitatively expressed by equation 2.1 as reported in [16]

$$V_{OC} = \frac{KT}{q} \ln\left(\frac{\eta\Phi_0}{n_0 k_{et} [I_3^-]}\right) \quad (2.1)$$

Where  $\eta$  is the quantum yield of photogenerated electrons,  $\Phi_0$  is the incident photon flux  $n_0$  is the electron density under dark conditions in the  $TiO_2$  conduction band, while  $k_{et}$  represents the rate constant of the triiodide reduction and  $[I_3^-]$  is the triiodide concentration.

### 2.1.4 Counter electrode and substrate

The DSSC counter electrode is made up of a FTO covered glass substrate coated with a sputtered Platinum film. Platinum has a double purpose: to catalyze the reduction of the triiodide ions and to reflect back the radiation that passes through the device increasing the light absorption and therefore boosting the resulting photogenerated current and the overall cell efficiency.

As regards the substrate, the FTO layers affects the DSSC performances in two ways: firstly, it increases the series resistance  $R_S$  of the cell and secondly it reflects back a fraction of the incident light causing optical losses. In order to reduce FTO sheet resistance, thus minimizing  $R_S$ , a thicker FTO layer is preferable. However, thicker layers imply a reduced transmittance efficiency. An optimized value for the FTO sheet resistance was found to be  $10\Omega/\square$  with a related radiation transmittance of  $\approx 80\%$ [10].

## 2.2 DSSC module characterization

The DSSC module performances were tested using a 91195 Newport solar simulator and a 2440 Keithley was used as the source measurement unit(SMU). The former is reported in Fig.2.4. It simulates the solar radiation using an AM1.5G solar spectrum. The SMU, instead, applies a varying potential with a 0.02V voltage step and measures the related current values. To perform this measurements, the SMU terminals are connected to the DSSC contacts.



Figure 2.4: Solar Simulator

To set the different parameters for the device characterization the graphical interface reported in Fig.2.5 was used. It has been programmed using a block-diagram Labview script.

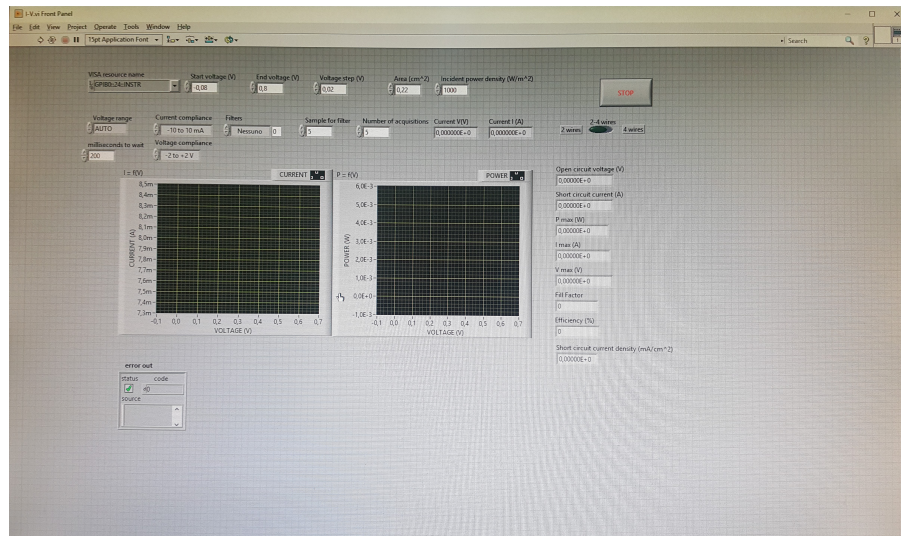


Figure 2.5: Graphical interface

### 2.2.1 Indoor light sources

Besides being tested under solar illumination conditions, the DSSCs module can be tested under indoor illumination conditions. More in details, in this master thesis, a LED lamp, a fluorescence lamp and a halogen lamp will be employed. The emission spectra of this three light sources were measured by means of an Ocean Optics spectrometer. They are reported in 2.6.

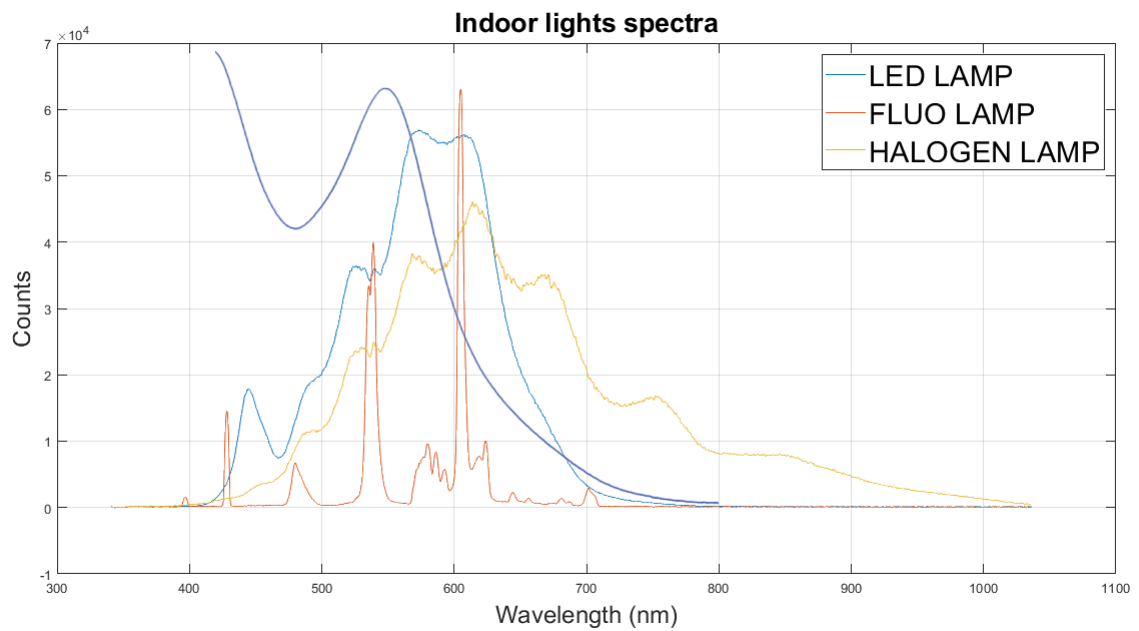


Figure 2.6: Indoor lights spectra

## 2.3 Device fabrication

At this point, a detailed description of the fabrication steps performed to build the DSSC module is given. The module consists of six series connected DSSCs arranged in a "W-type" configuration. Fig.2.7, modified from [47], shows the section of the module clarifying how a "W-type" connection works.

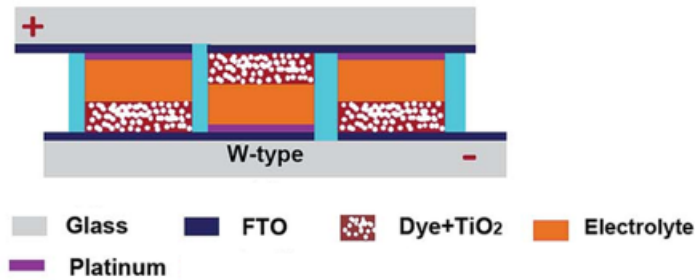


Figure 2.7: W-type series connection[47]

For the sake of clarity, the performed steps are reported in the form of a bullet list.

- Two  $5 \times 5 \text{ cm}^2$  FTO covered glass plates, reported in Fig.2.8 were used as the DSSC module substrates.



Figure 2.8: Glass substrates

- The FTO of the two glass substrates was properly patterned by using a diamond tip in order to electrically insulate the counter electrode of one cell from the photoanode of the neighboring DSSC and six holes(diameter  $\approx 1\text{mm}$ ) were

drilled through the backward plate to allow the electrolyte filling. The final result is shown in Fig.2.9

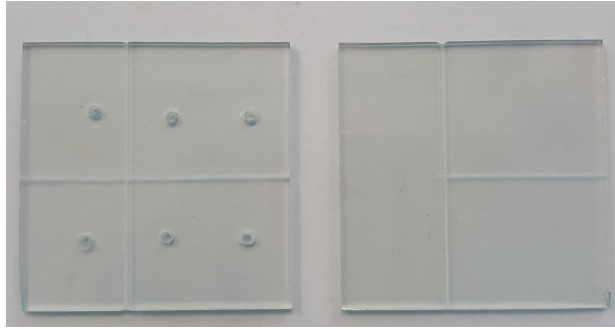


Figure 2.9: FTO patterning

- The two glass plates were rinsed in a ethanol-acetone ultrasonic bath for about 10 minutes to remove the eventual residual FTO dust and dried using  $N_2$  flow.
- The titania paste was deposited onto the glass plates exploiting doctor blade technique. More in details, 80  $\mu m$  thick adhesive tapes were properly patterned with holes (manually), to define the photoanodes of the six DSSCs, and put on the FTO conductive side, thus serving as fabrication masks. Fig.2.10 shows a picture of the described steps:

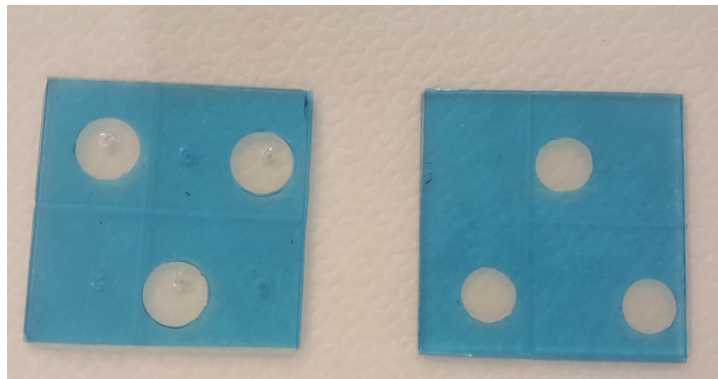


Figure 2.10: Titania deposition preparation

As can be seen from Fig.2.10 the back-illuminated plate shows higher surface

photoanodes(diameter = 12mm) than the front-illuminated ones(diameter = 10mm). This is due to the fact that the incident power density is clearly greater on the front-illuminated cells than the back-illuminated ones and therefore different active surfaces are needed to ensure comparable current values for the different DSSCs. The photoanodes diameters have been chosen according to what found in [38]. At the end of the titania paste deposition, the tapes were removed carefully and the two glass plates were put on a hot plate(at  $\approx 90^\circ\text{C}$ ) for 15-20 minutes to reduce the surface irregularities, let the solvent evaporating and bring the air bubbles out. Fig.2.11 shows the final result at this point.

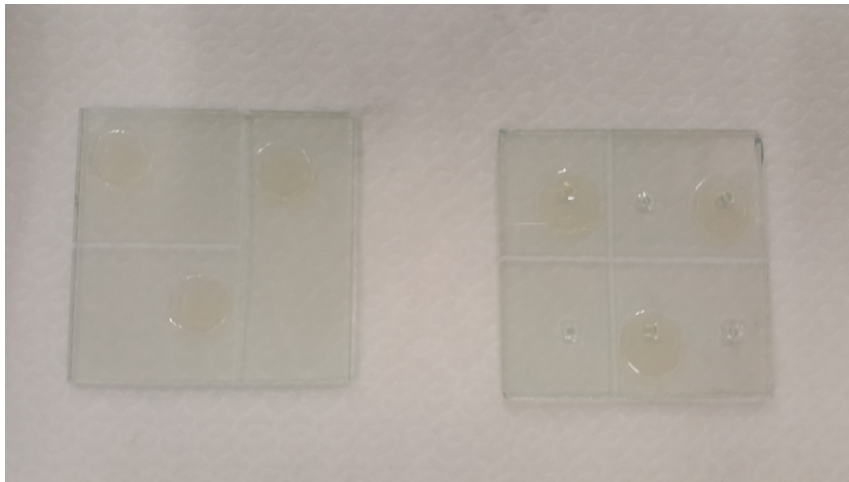


Figure 2.11: Titania deposition

- The two substrates were afterwards sintered with two different recipes depending on the particular  $TiO_2$  paste used(SOLARONIX *anataseTiO<sub>2</sub>* transparent paste or Dyesol *anataseTiO<sub>2</sub>* opaque paste). Namely, for the Dyesol paste the baking recipe was the following:
  1. temperature increase from  $26^\circ\text{C}$  to  $515^\circ\text{C}$  (rate:  $80\frac{^\circ\text{C}}{h}$ )
  2.  $515^\circ\text{C}$  isotherm for 30 minutes

3. temperature decrease from  $515^{\circ}\text{C}$  to  $26^{\circ}\text{C}$  (in about 5 hours)

For the SOLARONIX transparent titania paste, instead, the sintering program was different:

1. temperature increase from  $26^{\circ}\text{C}$  to  $450^{\circ}\text{C}$  (rate:  $80\frac{^{\circ}\text{C}}{\text{h}}$ )
2.  $450^{\circ}\text{C}$  isotherm for 30 minutes
3. temperature decrease from  $450^{\circ}\text{C}$  to  $26^{\circ}\text{C}$  (in about 5 hours)

In both cases the baking process was performed using a Nabertherm oven (see Fig. 2.12).



Figure 2.12: Sintering oven

At the end of the sintering process in the case of the transparent paste, that was the one chosen to describe the DSSCm fabrication steps in this section of the chapter, the two substrates look like in Fig. 2.13 and 2.14. The  $\text{TiO}_2$  layer thickness was measured using a Mitutoyo profilometer and resulted to be equal to  $10\ \mu\text{m}$ .

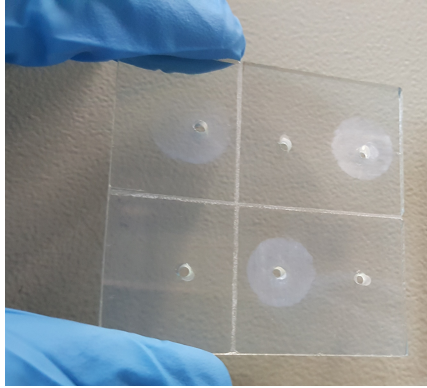


Figure 2.13: Sintered  $TiO_2$  transparent paste

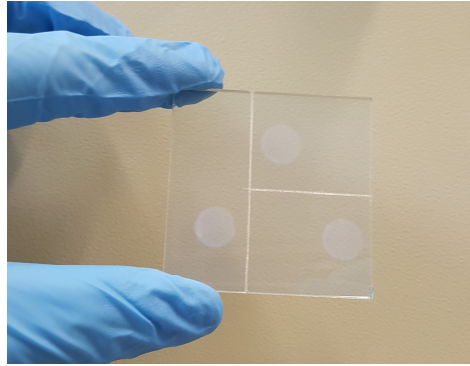


Figure 2.14: Sintered  $TiO_2$  transparent paste

- Platinum was sputtered(Q150TS, Quorum Technologies Ltd.) onto the DSSCs counter electrodes using a 30mA current corresponding to a deposition rate of about  $30 \frac{nm}{min}$ . A 15s deposition time was employed for the front illuminated DSSCs cathodes( $\approx 7.5$  nm thick Pt layers) and a 100s deposition time for the back-illuminated cathodes( $\approx 50$  nm thick Pt layers). The different thicknesses are due to the fact that a thicker Pt layer would dramatically reduce the incident power density onto the back-illuminated photoanode, thus significantly reducing the photogenerated current. To define the proper geometry of the electrodes parafilm layers have been patterned manually and used as masks as shown in Fig.2.15.

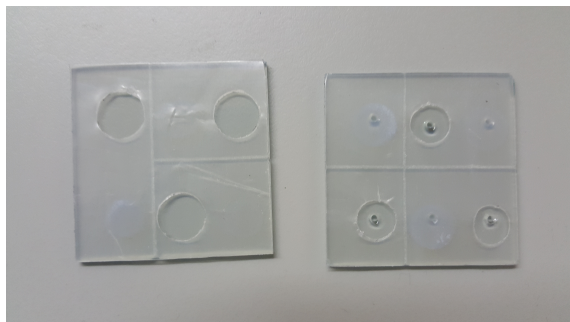


Figure 2.15: Pt sputtering preparation

Fig.2.16 shows the result of Pt electrode deposition:

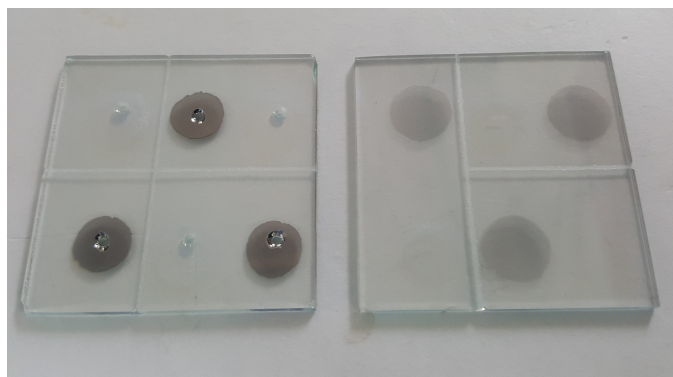


Figure 2.16: Pt electrodes deposition

- The two substrates were immersed in a 0.3 mM N719 dye solution in ethanol and were kept there (in a dark environment to prevent dye damage from UV radiation) for about 24h in order to get a suitable adsorption of the dye molecules on the  $TiO_2$  structure. At the end of this procedure the photoanodes show a dark red colour, as reported in Fig.2.17

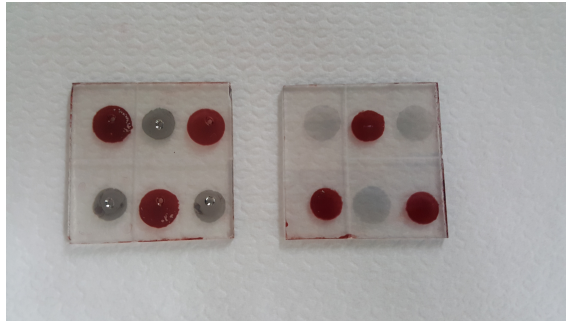


Figure 2.17:  $TiO_2$  photoanodes after the dye adsorption

- The devices were sealed using a  $60\mu m$  thick meltonix film. The thermoplastic film has been properly patterned in order to match the different electrodes area. The sealing happens placing the substrates as a glass sandwich and applying heat and pressure by means of a hot press(see Fig.2.18) until the whole surface of the polymer has melted onto both substrates.



Figure 2.18: Hot press

The applied temperature was  $105^{\circ}\text{C}$ . A huge care must be put in the choice of the applied pressure, temperature and sealing process time. In fact, a too high temperature may lead to the spread out of the gasket causing an uneven gasket thickness. Moreover, a too high temperature or sealing time may cause the formation of bubbles in the sealing film causing the electrolyte leakage. In order to reduce this issue, a meltonix film with a protective foil can be used or alternatively a PET protective layer can be employed exploiting the fact that it does not melt with the sealing film at the working temperatures. On the other hand, it should be taken into account that too low temperature and-or too low pressure would not melt properly the thermoplastic film, thus leading to electrolyte leakage as well. A graphical representation of the sealing mechanism and the final result are reported in Fig.2.19 and 2.20 respectively.

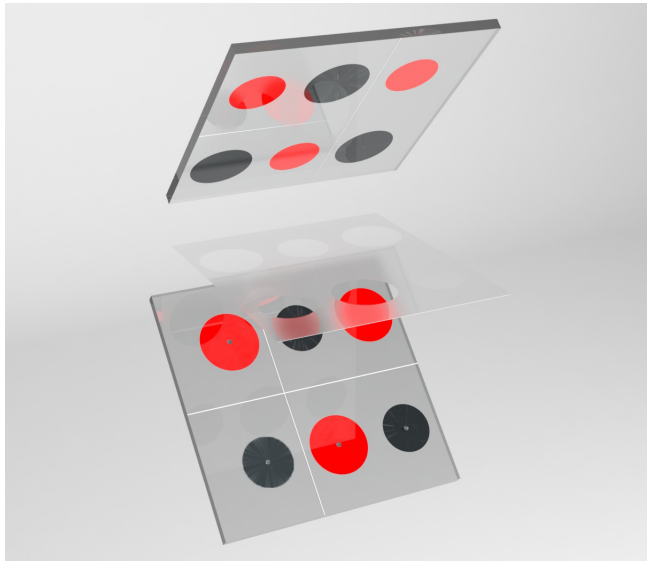


Figure 2.19: Sealing mechanism

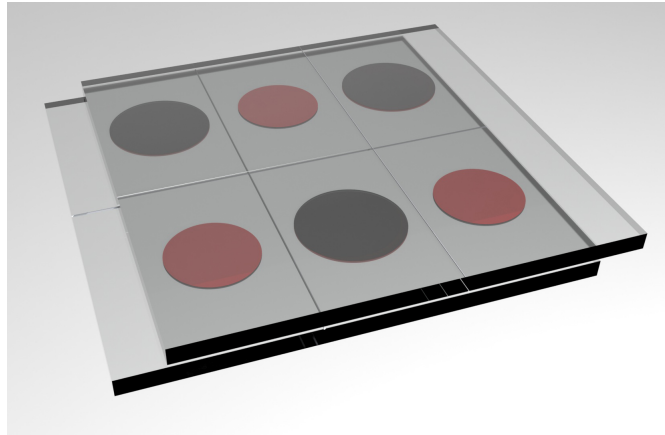


Figure 2.20: Final result after sealing

- Given that the meltonix film physically insulates the six DSSCs, the AN-50 iodolyte was injected into the devices through the 6 holes by vacuum backfill technique. Once all the different cells were filled, they have been sealed using parafilm(or meltonix) and glass fragments placed on the 6 holes. It is to be noted that the electrolyte is confined for every single cell, so that the DSSCs series connection is protected from the formation of additional charge path due to shared electrolyte. At this point, the DSSCs harvesting module is completed. It is shown in Fig. 2.21:

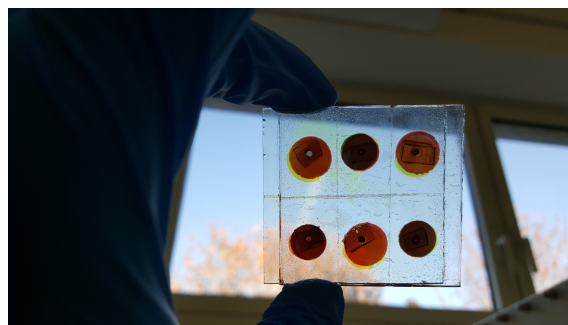


Figure 2.21: DSSC harvesting module

## 2.4 Commercial Supercapacitor characterization

As it has been stated before, a commercial supercapacitor (AVX BestCap series) with a nominal capacitance of 33mF was used. In this section of the chapter EIS and CV are carried out to verify the supercapacitor main parameters. To perform the required measurements Ec-lab Biologic software and instrumentation were used, while the plots reported in this section have been obtained using Matlab software. The CV results are reported in Fig.2.22.

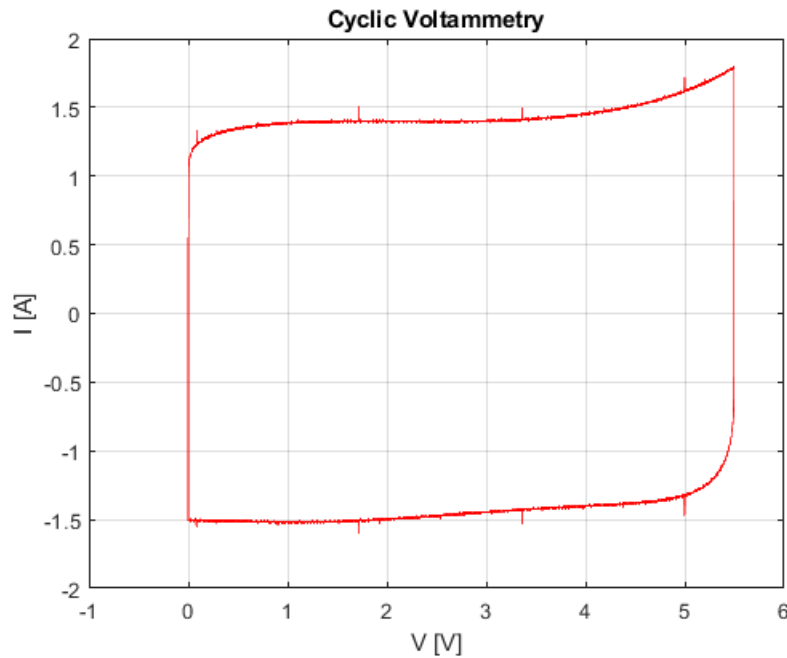


Figure 2.22: Cyclic voltammetry commercial SC

From the CV measurements it is possible to evaluate the Coulombic efficiency and the capacitance of the supercapacitor. In fact, it is known that:

$$C = \frac{Q_-}{2\Delta V} = \frac{0.352C}{5.5V \cdot 2} = 0.032F \quad (2.2)$$

Where  $Q_-$  is the charge,  $\Delta V$  is the potential window (equal to 5.5V as declared

in the supercapacitor data sheet and verified by the presence of the spike in the CV plot). The Cyclic voltammetry was performed using a scan rate  $\nu$  equal to  $50 \text{ mVs}^{-1}$ . The obtained result of  $0.032\text{F}$  is definitively comparable with the  $33\text{mF}$  value declared by the manufacturer. The coulombic efficiency, instead, was computed according to 2.3:

$$C.E. = \frac{Q_-}{Q_+} = \frac{0.349C \cdot 100}{0.352C} = 99.1\% \quad (2.3)$$

The other important parameter to be computed is the internal series resistance which can be derived considering the real part of the impedance when the frequency is equal to  $1\text{kHz}$ , as stated by [48]. The computed value was  $0.26 \Omega$  which shows a great correspondence with the values reported in the supercapacitor data sheet (typ. value  $0.25\Omega$ , max. value  $0.3\Omega$ ). Fig.2.23 reports the Nyquist plot considering a frequency range which goes from  $1\text{Hz}$  to  $100 \text{ kHz}$ .

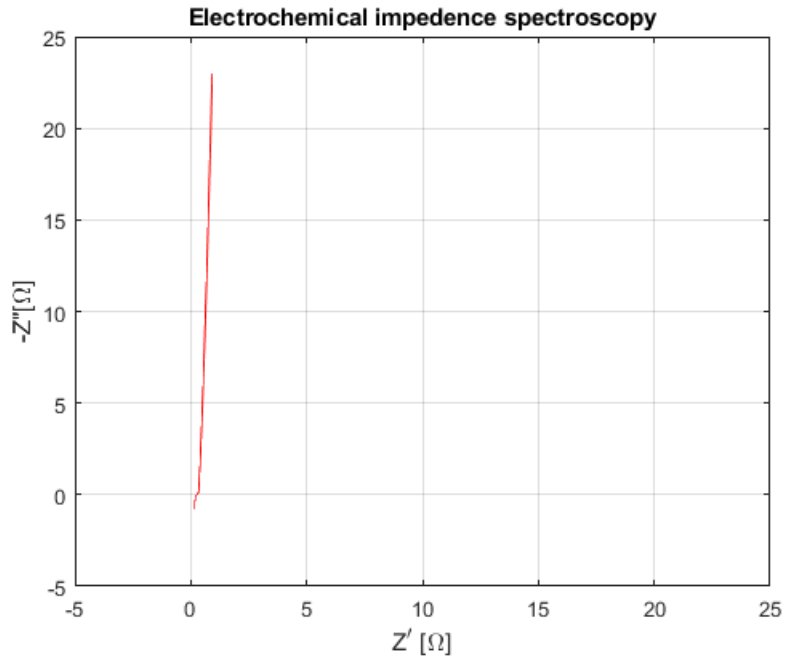


Figure 2.23: EIS commercial SC

# Chapter 3

## Results

In order to define a standard and easy fabrication procedure for the DSSCs module, as well as to optimize its design, some preliminary tests have been performed. In particular:

- Test 1: a 2 series-connected DSSCs module was built sharing the electrolyte between the two cells and the device was closed just using two clips. The electrodes had rectangular shapes ( $1.1 \times 5$  and  $1.9 \times 4.5$ ) and the two glass substrate were kept for 12 hours in a 0.1 mM N-719 dye solution in ethanol.
- Test 2: a 6 series-connected DSSCs module was built, again, sharing the electrolyte, a meltonix layer was placed at the border of the module to seal the device. But, this time, all the cells had equal circular photoanodes(radius = 0.5cm), the N-719 solution concentration was 0.3 mM and the substrates were kept immersed in the solution for 24 hours.
- Test 3: a parafilm layer was used to seal the module and insulate the single cells instead of the meltonix film, in order to simplify the sealing procedure and lower the sealing costs.
- Test 4: a meltonix film was used to insulate the single cells and seal the device. The DSSCs module was working but showed very poor performance because of the current unbalance between the cells due to different incident power for front and back-illuminated solar cells. At this point, we have all the

information needed to realize the final energy harvesting module as described in 3.5.

The various obtained results are described in details in the following. All the plots of the experimental results reported in this chapter have been obtained using Matlab software.

### 3.1 Test 1

The first test performed was to build a energy harvesting module consisting of two series connected DSSCs sharing the electrolyte. This test was carried on to understand if it is possible to build properly working series-connected devices just sharing the electrolyte instead of confining it for every single cell. It is clear that the shared electrolyte would simplify the sealing process by far. In fact, it would allow to seal the module by using only a thermoplastic strip at the borders, which is afterwards melted by means of a hot press, instead of using a precisely patterned thermoplastic layer. Another possible way to seal the module with the shared electrolyte can be to use an epoxy resin to glue the two glass substrates. As the aim of the test was to see how the sharing of the electrolyte affects the module performance, and not to investigate the sealing procedure, the module was closed up by simply using two clips and the electrolyte was inleted between the two substrates by means of a pipette, exploiting capillary effect. As regards the other fabrication steps, they have been performed as described in 2 a part from two differences: the dye concentration in the ethanol solution(in this test, a 0.1mM N-719 solution was used instead of a 0.3mM not to delay the test because of the small amount of dye at my disposal at that very moment) and the immersion time of the module in the solution (12 hours instead of the 24 hours established by the definitive fabrication procedure defined). The final fabricated device is reported in Fig.3.1.

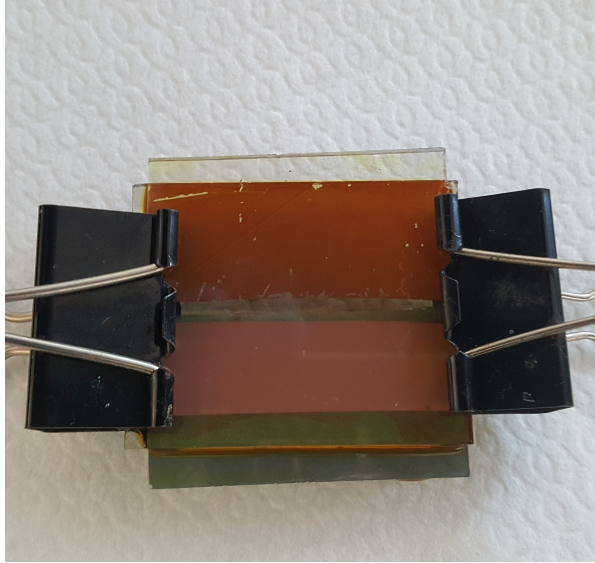


Figure 3.1: 2 series-connecte DSSCs module

It can be seen that a rectangular shape was chosen for the cells electrodes. More in details, the front-illuminated cell has a photoanode area of  $1.1 \times 5\text{cm}^2$ , while for the back-illuminated one the photoanode area is  $1.9 \times 4.5\text{cm}^2$ . The V-J characteristic of the module is reported in Fig.3.2.

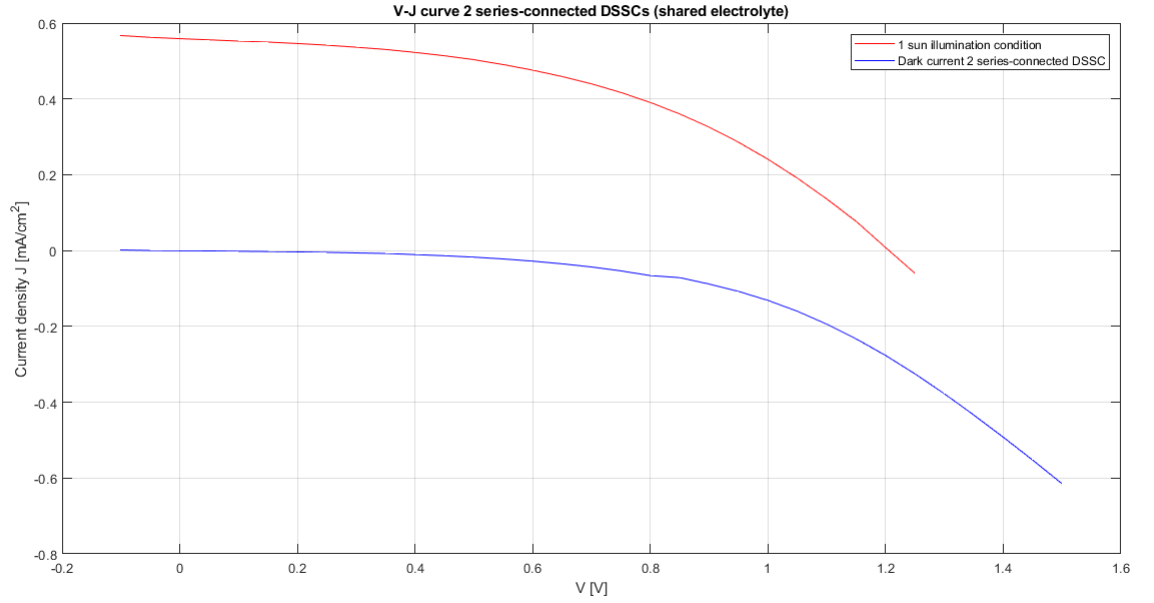


Figure 3.2: V-J curve under 1 SUN and dark illumination conditions (Test 1)

It can be seen that  $V_{OC} = 1.2V$  as it is expected from the series connection of two DSSCs. In fact, it should be remembered that the voltage drop across one single cell is about  $0.6V$ .  $I_{SC}$  is, instead, approximately equal to  $8mA$ . This means that, although the electrolyte is shared between the two cells and not separate for each device, the module is properly working. The low efficiency value  $\eta \approx 0.3\%$  is due to a bad dye adsorption on the  $TiO_2$  layer, whose causes can be found in the too low N-719 concentration in the ethanol solution ( $0.1mM$ ) and in the too short immersion time of the module in the dye solution ( $\approx 12h$ ). The FF, instead, shows an acceptable value of  $0.49$ .

Fig.3.2 plots also the V-J curve under dark conditions. Ideally, we want to minimize the dark current, that is we want to minimize the charge recombination between the photoinjected electron and  $I_3^-$ . It is to be noted that the N-719 dye already reduces the dark current in a significant way[49], as can be seen from the good dark conditions performance shown in Fig.3.2, but it is possible to further increase the

dark current control. In order to do that, an exploited solution is the introduction of a  $TiCl_4$  blocking layer on the conductive FTO.

For the sake of completeness, the plot of the power from the solar cell is reported in Fig.3.3:

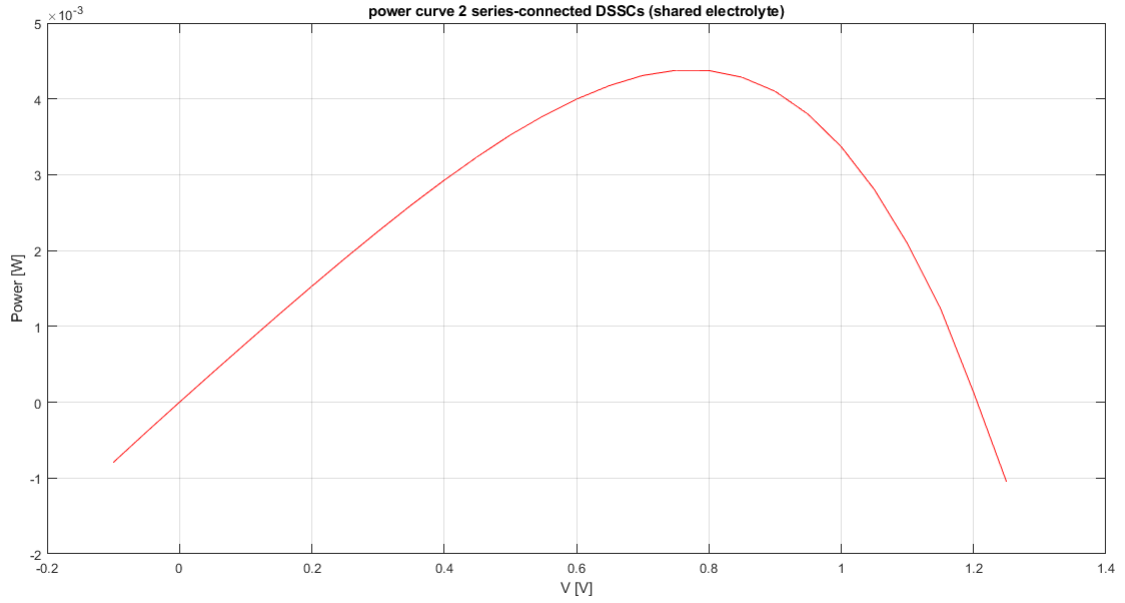


Figure 3.3: Power curve 2 series-connected DSSC module

## 3.2 Test 2

Having obtained good results with the series connection of two DSSCs sharing the electrolyte, a second test was performed, building a new module made up of six DSSCs connected in series in a "W" configuration, always sharing the electrolyte. In this second module, all the cells have equal circular electrodes of radius equal to 0.5 cm. Moreover, a 0.3 mM N-719 dye solution in ethanol was used and the two glass substrates were left immersed in the solution for 24 hours. Finally, a  $60\mu m$  meltonix film placed at the borders together with a bicomponent epoxy resin have

been used to seal the module. A picture of the final result is reported in Fig.3.4

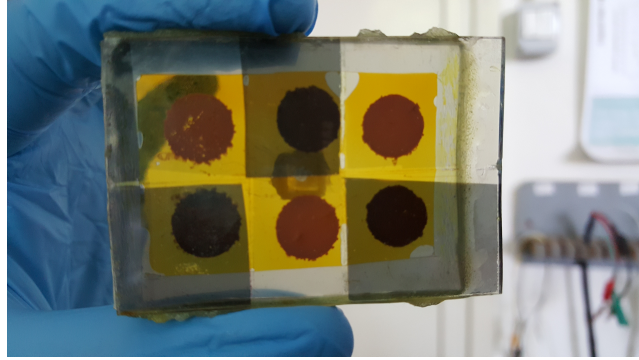


Figure 3.4: 6 series-connected DSSCs sharing the electrolyte

The J-V curve of the module is reported in Fig.3.5.

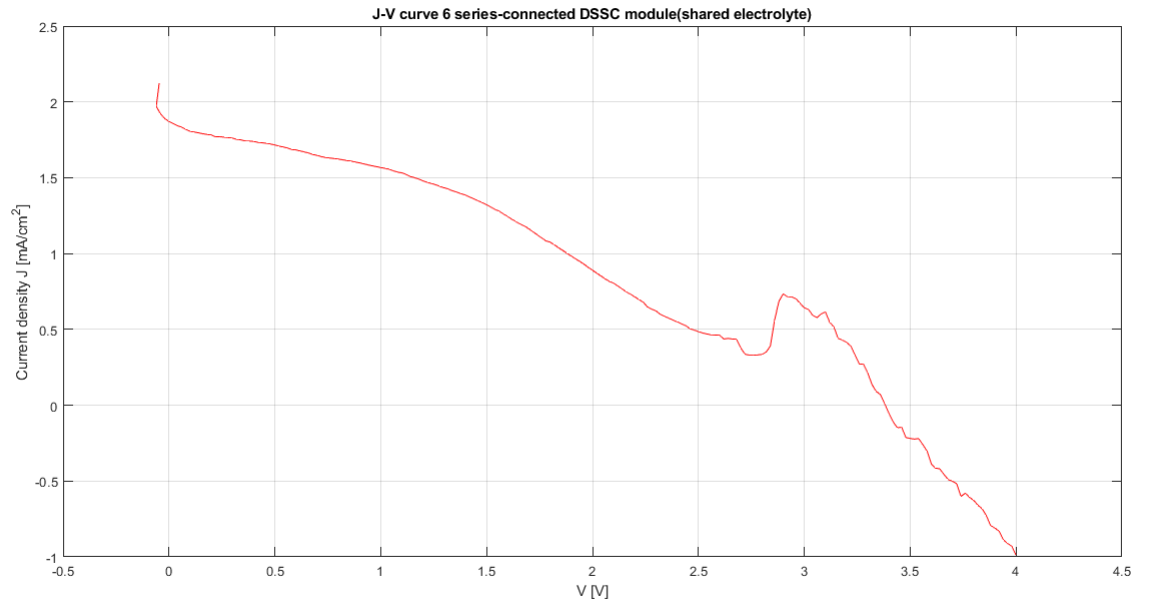


Figure 3.5: V-J curve under 1 SUN illumination condition (Test 2)

It is clear that, this time, the device is not working properly, even though the module shows a  $V_{OC} \approx 3.5V$ . In fact, the curve has not the expected classical shape and shows a strange peak around the applied voltage value of 3V. This strange

behavior should be ascribed to the presence of the shared electrolyte that provides an alternative path for the photogenerated electrons causing dramatic detrimental effects for the overall module. This effect was not evident in the harvesting module built in 3.1 because, being just two series-connected DSSCs, the solar cells were neighbouring and therefore the electrons parasitic paths were shorter not causing significant damages to the module performance. Thus, this test has shown that it is not possible to build a module made up of six series connected DSSCs just sharing the electrolyte. It is necessary to physically separate the different cells by properly patterning the thermoplastic sealing film. The power curve of the built module is reported in Fig.3.6.

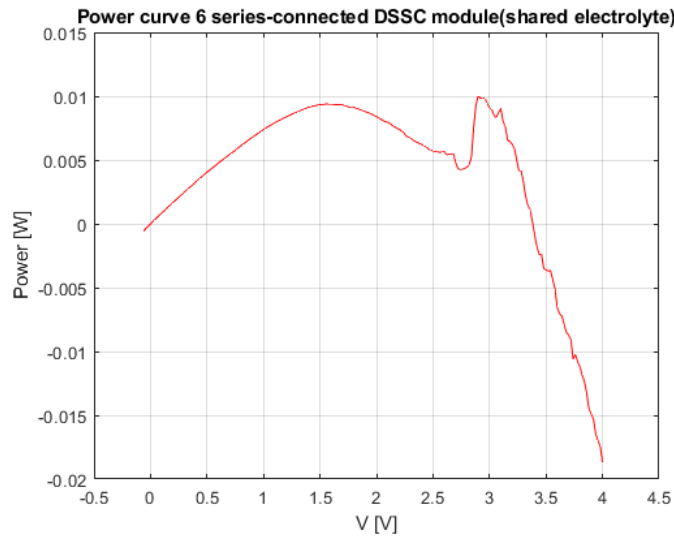


Figure 3.6: Power curve 6 series-connected DSSCs module(shared electrolyte)

### 3.3 Test 3

Having understood from 3.2 that it is not possible to share the electrolyte in the 6 DSSCs module, it becomes mandatory to pattern the sealing film in order to confine the electrolyte for every single cell. However, the Meltonix film is quite expensive

and requires a careful sealing process. In fact, a too high pressure or temperature may allow the formation of air bubbles in the film leading to the electrolyte leakage. For this reason a new module was built as described in 3.2, but this time using a properly patterned parafilm layer as the sealing element. Parafilm, in fact, is a cheaper material and undergoes easier fabrications steps. On the other hand, the sealing is not effective as it can be seen from Fig.3.7.

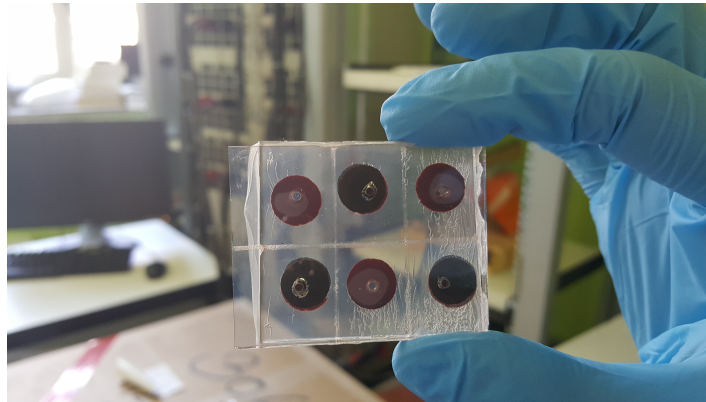


Figure 3.7: 6 series-connected DSSCs module parafilm sealing

## 3.4 Test 4

At this point, a new module was built just as the one described in 3.3 (a picture of the 2 glass substrates is reported in Fig.3.8), but this time a  $60\mu m$  Meltonix film was used to seal the device.

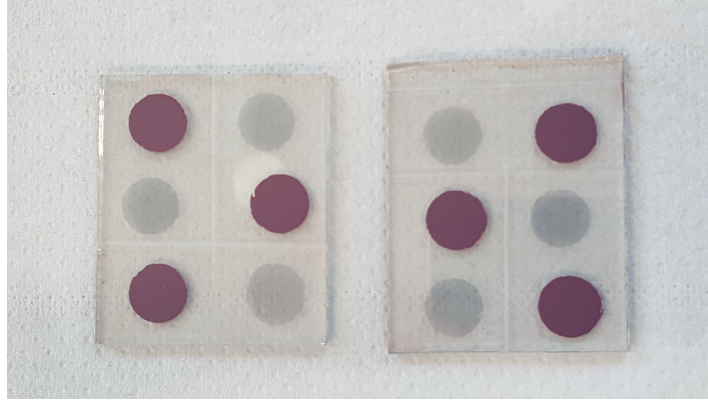


Figure 3.8: 6 series-connected DSSCs module substrates

The V-J curve of the device is reported in Fig3.9 and, for the sake of clarity, the main parameters used for the DSSCs module performance evaluation are reported in table3.1:

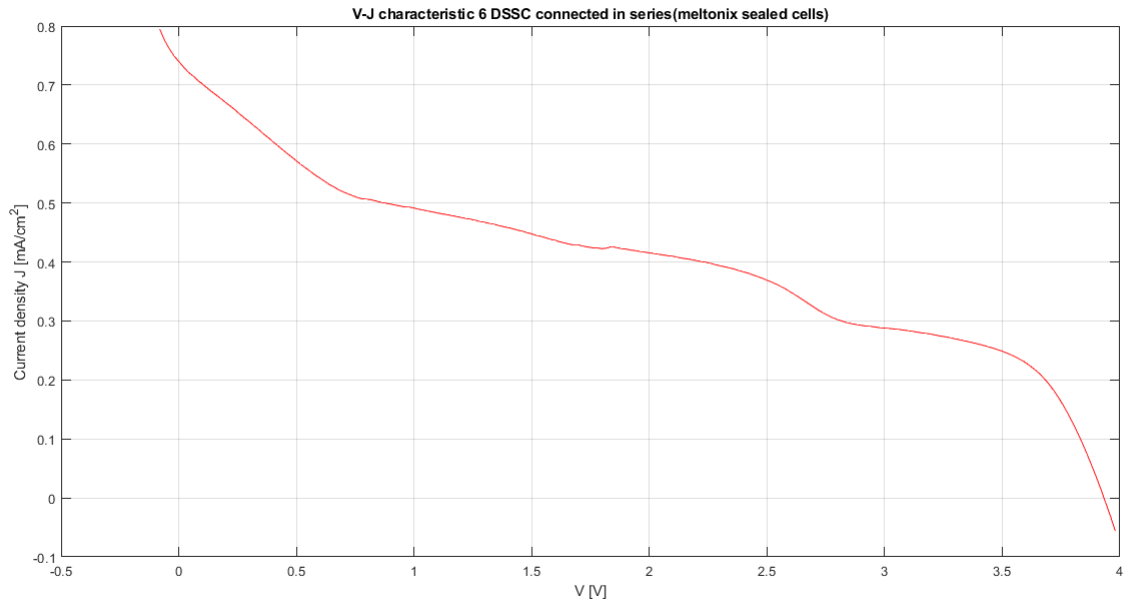


Figure 3.9: V-J curve (Test 4)

Table 3.1: DSSCs module parameters

Parameter	Value
Area( $cm^2$ )	4.71
$I_{SC}$ (A)	$3.48 \cdot 10^{-3}$
$V_{OC}$ (V)	3.9
$P_{MAX}$ (W)	$4.35 \cdot 10^{-3}$
$I_{MAX}$ (A)	$1.75 \cdot 10^{-3}$
$V_{MAX}$ (V)	2.48
FF	0.32
Eff(%)	0.92
$J_{SC}$ ( $\frac{mA}{cm^2}$ )	$7.4 \cdot 10^{-1}$

The poor performance of the DSSCs module built in this test are due to the current mismatch between front-illuminated and back-illuminated cells (resulting from the "W-type" series connection of the devices that constitute the module), as described in [50]. In order to reduce this issue and have an uniform current across the devices, the photoactive areas of the back-illuminated cells should be bigger than the front-illuminated ones, so that they compensate the smaller amount of incident radiation that reaches the photoanodes. An optimum value for the ratio between back-illuminated photoactive areas and front-illuminated ones was found to be between [1.4-1.6] , as reported in[51].

Fig.3.10 plots the V-J curve for the same module under many illumination conditions to see how different incident power affects the device performance. All the

measured values are reported in Table 3.2

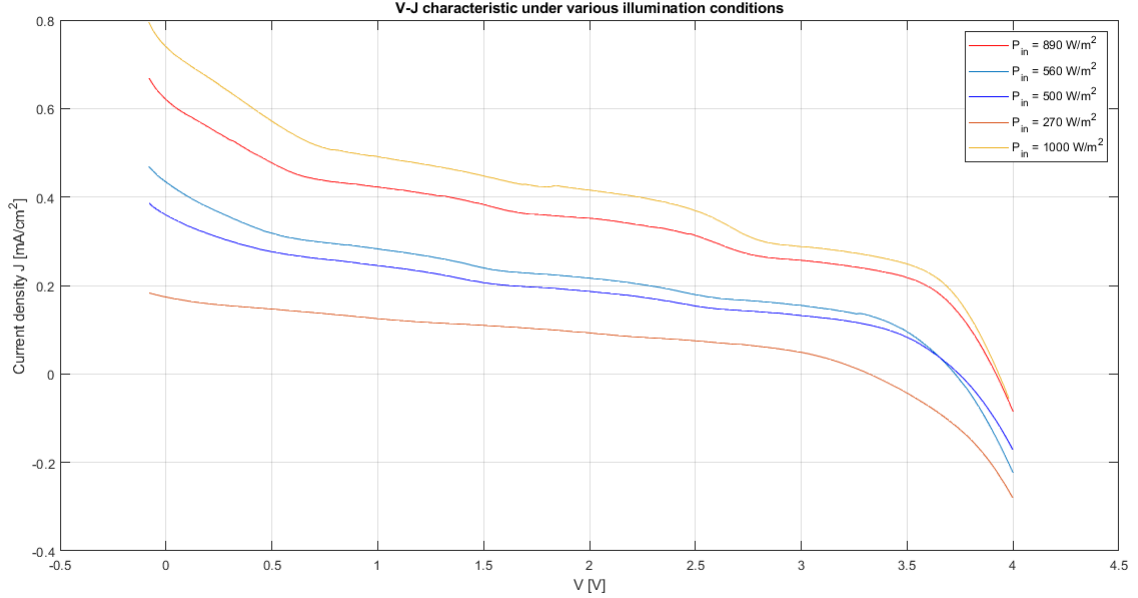


Figure 3.10: V-J curve under different illumination conditions (Test 4)

It can be seen that  $I_{SC}$ ,  $J_{SC}$  and  $P_{MAX}$  decrease as the incident power decrease. This can be easily understood just reminding that a reduced input power implies a smaller photogenerated current. Also  $V_{OC}$  decreases lowering the incident power and this can be easily proved recalling eq. 2.1. The FF variation, instead, does not show a clear monotonic trend and this is due to the fact that the reduction in the input power lowers both the numerator and the denominator of the ratio 1.4; thus, the overall variation of the FF value depends on which is the dominant effect. Finally, considering the module efficiency, it lowers as the incident light intensity is reduced. This may seem strange considering that reducing the input power reduces the denominator of eq. 1.5, but, again, the numerator is reduced too and to a more significant extent, thus dominating the final effect on the efficiency value.

In order to assess the repeatability of the fabrication steps and of the device

Table 3.2: DSSCs module parameters under different illumination conditions

Parameter	$P_{in} = \frac{1000W}{m^2}$	$P_{in} = \frac{890W}{m^2}$	$P_{in} = \frac{560W}{m^2}$	$P_{in} = \frac{500W}{m^2}$	$P_{in} = \frac{270W}{m^2}$
Area( $cm^2$ )	4.71	4.71	4.71	4.71	4.71
$I_{SC}$ (A)	$3.48 \cdot 10^{-3}$	$2.92 \cdot 10^{-3}$	$2 \cdot 10^{-3}$	$1.69 \cdot 10^{-3}$	$8.19 \cdot 10^{-4}$
$V_{OC}$ (V)	3.9	3.9	3.8	3.74	3.32
$P_{MAX}$ (W)	$4.35 \cdot 10^{-3}$	$3.71 \cdot 10^{-3}$	$2.22 \cdot 10^{-3}$	$1.87 \cdot 10^{-3}$	$8.86 \cdot 10^{-4}$
$I_{MAX}$ (A)	$1.75 \cdot 10^{-3}$	$1.14 \cdot 10^{-3}$	$7.64 \cdot 10^{-4}$	$6.51 \cdot 10^{-4}$	$3.66 \cdot 10^{-4}$
$V_{MAX}$ (V)	2.48	3.25	2.9	2.87	2.42
FF	0.32	0.32	0.29	0.30	0.33
Eff(%)	0.92	0.87	0.67	0.66	0.63
$J_{SC}$ ( $\frac{mA}{cm^2}$ )	$7.4 \cdot 10^{-1}$	$6.2 \cdot 10^{-1}$	$4.26 \cdot 10^{-1}$	$3.55 \cdot 10^{-1}$	$1.74 \cdot 10^{-1}$

performance another module was built, as much as possible identical to the previous one. The V-J curve for this second module is reported in Fig.3.11, while the main parameters values are summarized in Table3.3

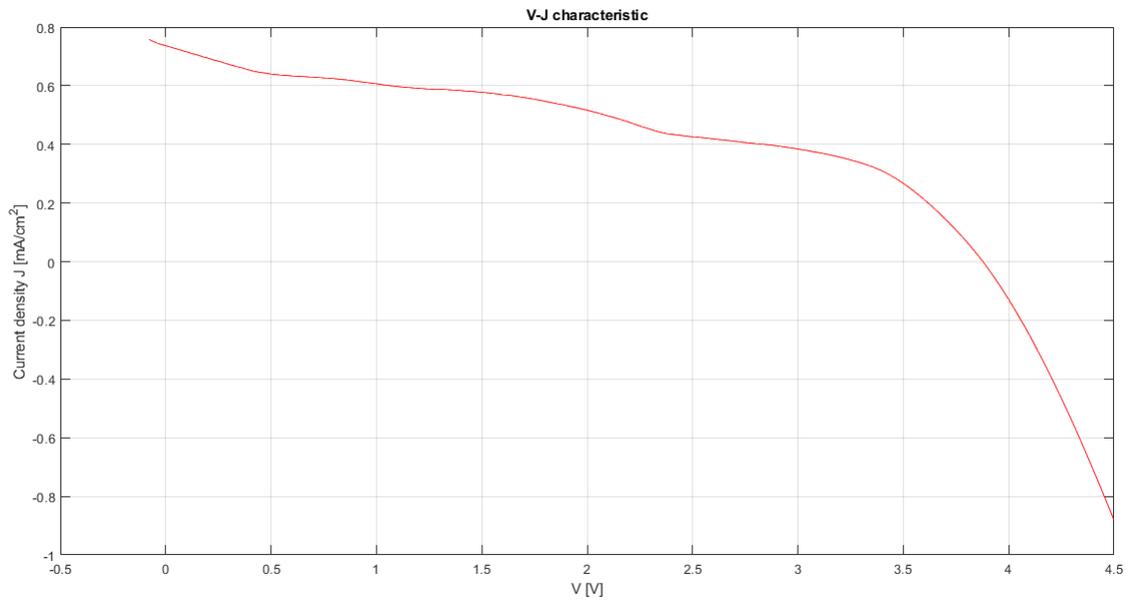


Figure 3.11: V-J curve (Test 4, 2<sup>nd</sup> module)

Table 3.3: DSSCs module parameters

Parameter	Value
Area( $cm^2$ )	4.71
$I_{SC}$ (A)	$3.47 \cdot 10^{-3}$
$V_{OC}$ (V)	3.87
$P_{MAX}$ (W)	$5.43 \cdot 10^{-3}$
$I_{MAX}$ (A)	$1.79 \cdot 10^{-3}$
$V_{MAX}$ (V)	3.03
FF	0.40
Eff(%)	1.15
$J_{SC}$ ( $\frac{mA}{cm^2}$ )	$7.37 \cdot 10^{-1}$

As it can be seen, this second module not only does it work properly, but also shows improved performance such as higher efficiency (1.15% instead of 0.92%) and higher FF (0.40 instead of 0.32) with respect to the previous one. For the sake of completeness, a comparison of the V-J curves of the two energy harvesting modules is given in Fig3.12:

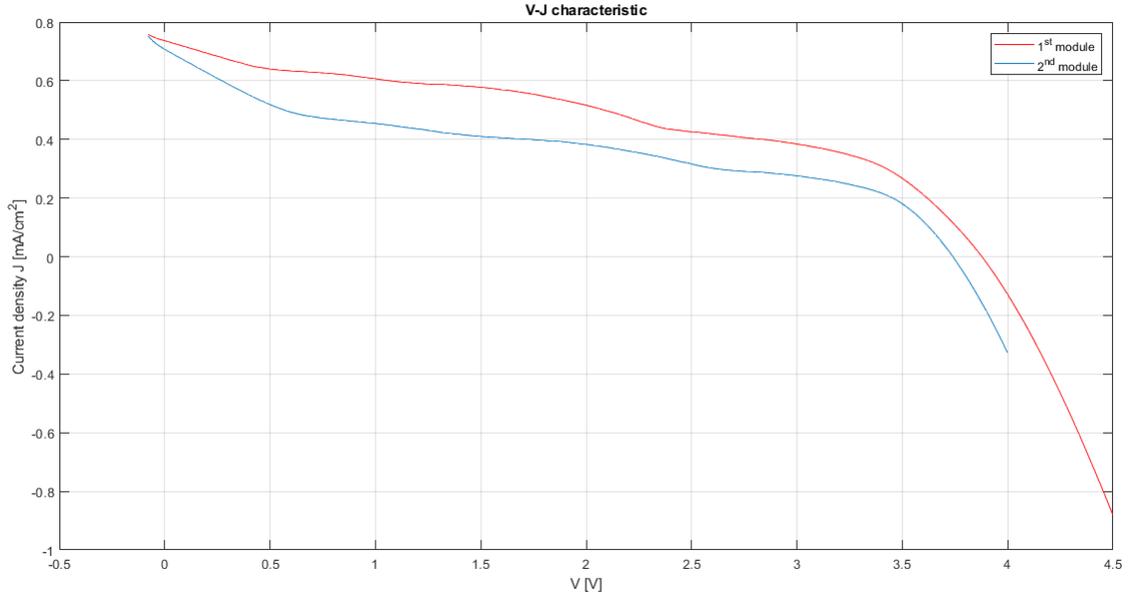


Figure 3.12: V-J curves comparison

### 3.5 Fabrication and characterization of the final DSSCs module

As it was stated in 3.4, making a module with six identical devices is not a good choice in a "W-type" series-connection configuration because of the current mismatch due to the different illumination conditions of the front-illuminated cells and the back illuminated ones. In order to solve this issue, a new module was built having round photoanodes of radius 0.5 cm for the front-illuminated DSSCs and 0.6 cm for the back-illuminated devices. The surface ratio between back-illuminated and front-illuminated anodes will thus be equal to 1.44, which is a value comparable with the interval reported in [51]. The fabrication steps were exactly the same as for 3.4, a part from the different photoactive areas. As will be discussed below more in detail, this module shows good performance and therefore will constitute the energy

harvesting block of the power-pack system developed in this master thesis. Thus, the fabrication steps performed to build this module are the definitive ones reported in 2. A picture of the final module is reported in 3.13.

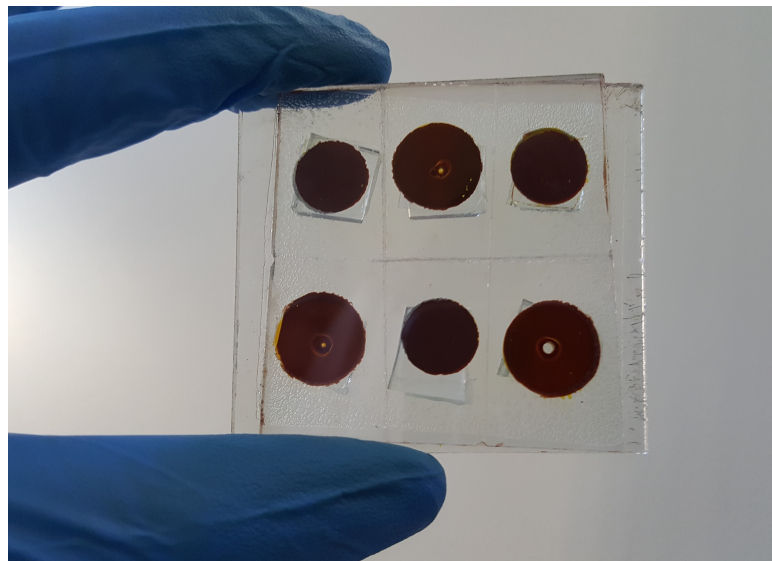


Figure 3.13: Final DSSCs module (balanced electrodes)

Fig.3.14, instead, represents the V-J curves of the module obtained from four successive measurements. It can be seen that, as long as we proceed with the measurements, the cells get warmer. This temperature increase leads to an upwards shift of the V-J curve up to a saturation condition, which is represented by the mauve curve in the picture.

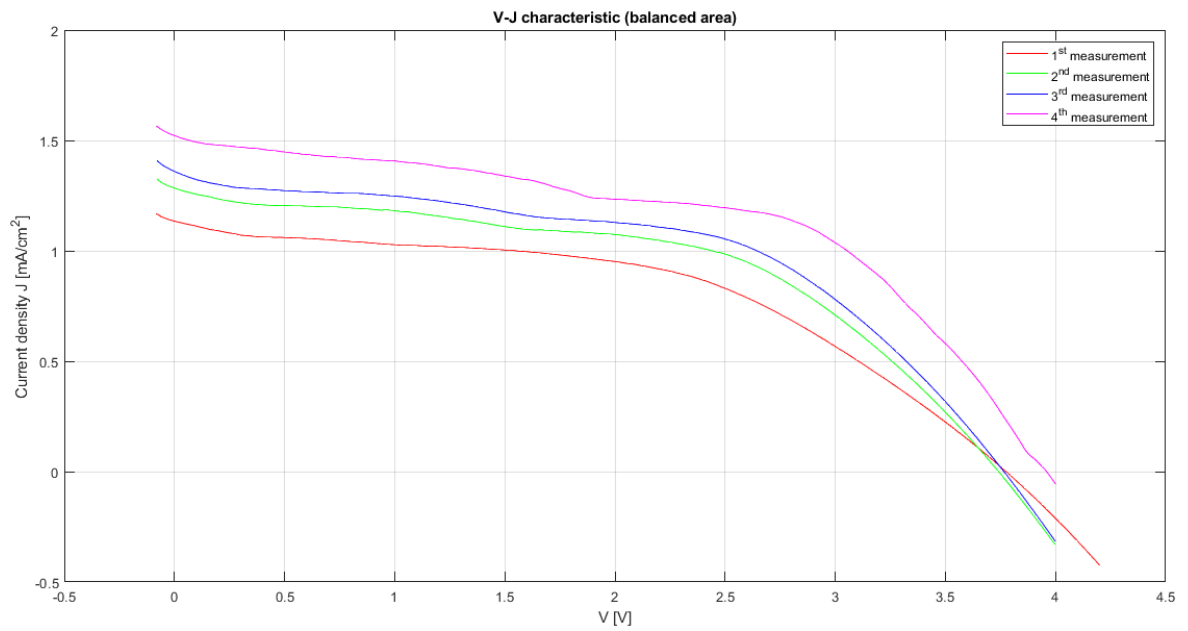


Figure 3.14: V-J curves

The parameters values for the definitive J-V curve are reported in table 3.4.

Table 3.4: DSSCs module parameters

Parameter	Value
Area( $cm^2$ )	5.74
$I_{SC}$ (A)	$8.75 \cdot 10^{-3}$
$V_{OC}$ (V)	3.95
$P_{MAX}$ (W)	$1.83 \cdot 10^{-2}$
$I_{MAX}$ (A)	$6.46 \cdot 10^{-3}$
$V_{MAX}$ (V)	2.84
FF	0.53
Eff(%)	3.19
$J_{SC}$ ( $\frac{mA}{cm^2}$ )	1.52

As it can be read out from the table, the module shows very good performance, namely a relatively high efficiency (3.19%) and FF (0.53). To further boost the device performance, a mirror was placed at the back of the module to increase the optical path, enhancing light absorption and therefore the photogenerated current. Detailed values for the various parameters in back-mirroring conditions are reported in Table3.5.

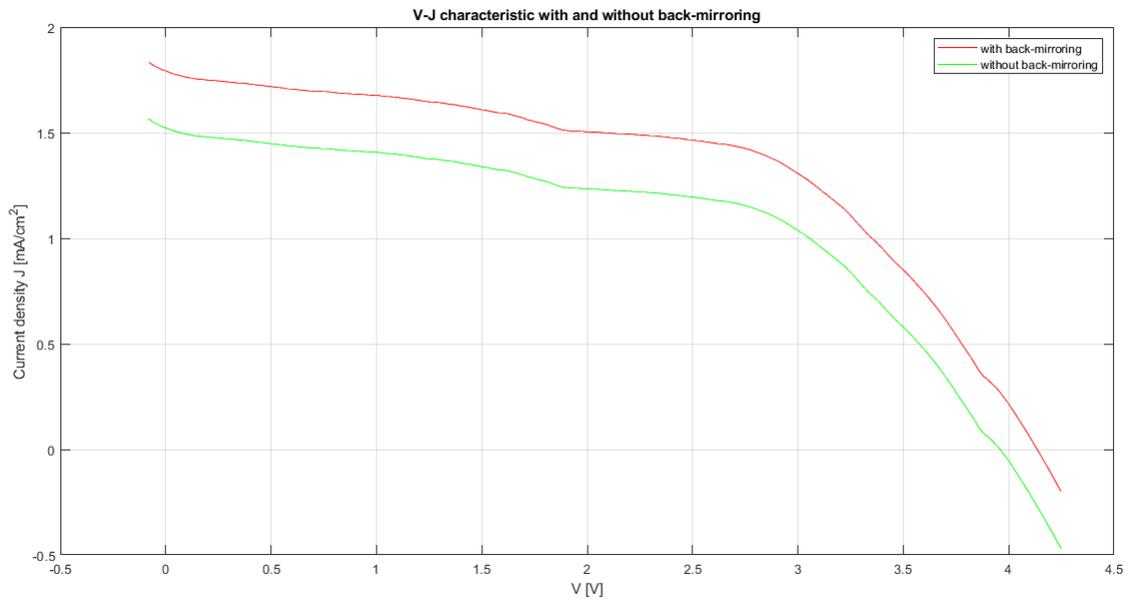


Figure 3.15: V-J curves comparison with and without mirroring

Table 3.5: DSSCs module parameters (with back-mirroring)

Parameter	Value
Area( $cm^2$ )	5.74
$I_{SC}$ (A)	$10.02 \cdot 10^{-3}$
$V_{OC}$ (V)	4.11
$P_{MAX}$ (W)	$2.25 \cdot 10^{-2}$
$I_{MAX}$ (A)	$7.5 \cdot 10^{-3}$
$V_{MAX}$ (V)	3
FF	0.54
Eff(%)	3.95
$J_{SC}$ ( $\frac{mA}{cm^2}$ )	1.784

In this master thesis it is to be given for granted that the measurements have been carried out without back-mirroring unless it is differently specified. The module performance under different illumination conditions are reported in Fig.3.16, while Table3.6 reports the measured parameters values.

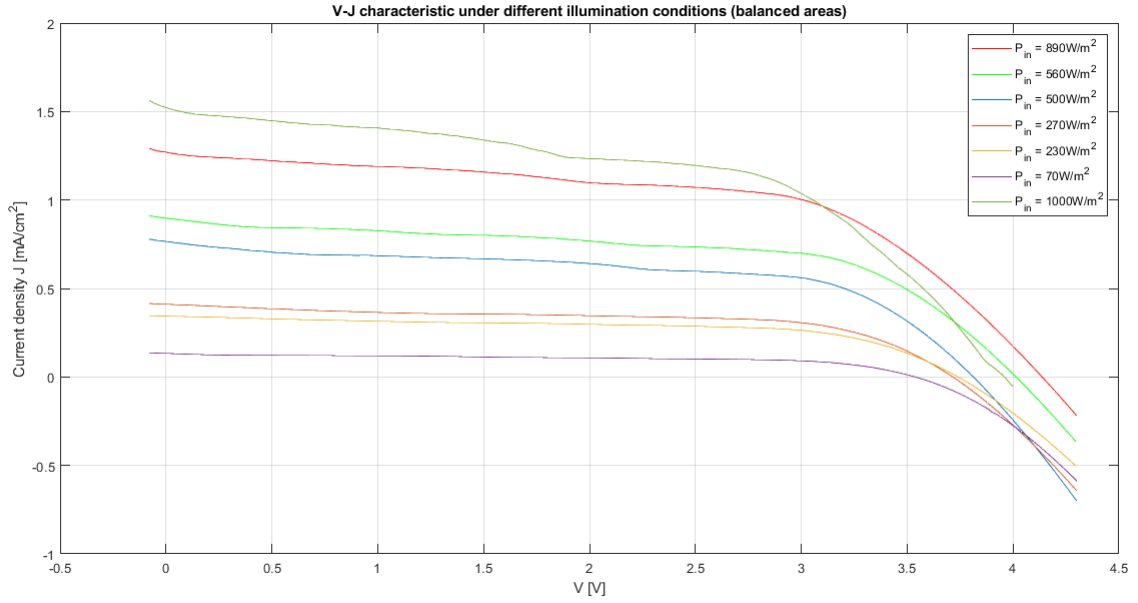


Figure 3.16: V-J curve under different illumination conditions

Table 3.6: DSSCs module parameters under different illumination conditions

Parameter	$P_{in} = \frac{1000W}{m^2}$	$P_{in} = \frac{890W}{m^2}$	$P_{in} = \frac{560W}{m^2}$	$P_{in} = \frac{500W}{m^2}$	$P_{in} = \frac{270W}{m^2}$	$P_{in} = \frac{230W}{m^2}$	$P_{in} = \frac{70W}{m^2}$
Area( $cm^2$ )	5.74	5.74	5.74	5.74	5.74	5.74	5.74
$I_{SC}$ (A)	$8.75 \cdot 10^{-3}$	$7.3 \cdot 10^{-3}$	$5.16 \cdot 10^{-3}$	$4.4 \cdot 10^{-3}$	$2.3 \cdot 10^{-3}$	$1.98 \cdot 10^{-3}$	$7.65 \cdot 10^{-4}$
$V_{OC}$ (V)	3.95	4.13	4.01	3.81	3.72	3.74	3.54
$P_{MAX}$ (W)	$1.83 \cdot 10^{-2}$	$1.72 \cdot 10^{-2}$	$1.21 \cdot 10^{-2}$	$9.66 \cdot 10^{-3}$	$5.3 \cdot 10^{-3}$	$4.55 \cdot 10^{-3}$	$1.59 \cdot 10^{-4}$
$I_{MAX}$ (A)	$6.46 \cdot 10^{-3}$	$5.73 \cdot 10^{-3}$	$3.92 \cdot 10^{-3}$	$3.2 \cdot 10^{-3}$	$1.77 \cdot 10^{-3}$	$1.53 \cdot 10^{-3}$	$5.4 \cdot 10^{-4}$
$V_{MAX}$ (V)	2.84	3.02	3.09	3.02	2.98	2.98	2.94
FF	0.53	0.57	0.59	0.58	0.60	0.62	0.59
Eff(%)	3.19	3.4	3.78	3.36	3.42	3.48	4.12
$J_{SC}$ ( $\frac{mA}{cm^2}$ )	1.52	1.27	$8.97 \cdot 10^{-1}$	$7.66 \cdot 10^{-1}$	$4.1 \cdot 10^{-1}$	$3.44 \cdot 10^{-1}$	$1.33 \cdot 10^{-1}$

### 3.5.1 DSSCs module EIS

In order to go further into the characterization of the module, an EIS was performed to study in a quantitative way the internal impedances involved in the DSSCs materials and operating principles. The frequency range chosen was between [0.1Hz,100kHz] and the measurements were performed in dark conditions under open circuit potential. Fig.3.17 reports the Nyquist plot of the impedance spectrum of the module.

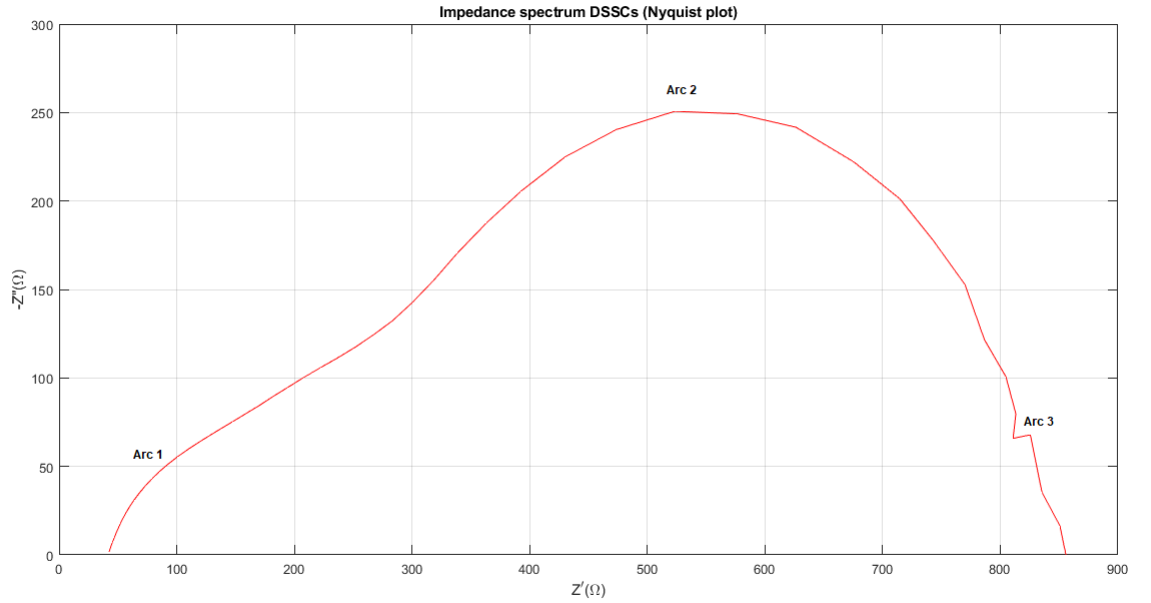


Figure 3.17: Impedance spectrum DSSCs module (Nyquist plot)

As reported in [28], we can see that Fig.3.17 shows three arcs. "Arc 1" is related to high frequencies, "Arc 2" to intermediate frequencies and "Arc 3" to low frequencies[52]. Moreover, the high frequency arc is related to the impedance at the Pt electrode ( $Z_{Pt}$ ) while the impedance of the  $TiO_2$  electrode ( $Z_{TiO_2}$ ) is determined through the central arc and the impedance due to the diffusion into the electrolyte ( $Z_{Elec}$ ) is related to the low frequency arc. Finally, there is another series resistive

contribution ( $R_{S_{FTO}}$ ) which is due to the FTO sheet resistance and to the electrical wiring[28].  $R_{S_{FTO}}$  can be determined from the EIS Nyquist plot by considering the distance between the origin of the axes and the beginning of "Arc 1". Considering just resistances, instead of impedances, the total module resistance is given by eq.3.1 from[28].

$$R = R_{S_{FTO}} + R_{TiO_2} + R_{Pt} + R_{Elec} \quad (3.1)$$

Where  $R_{TiO_2}$ ,  $R_{Pt}$  and  $R_{Elec}$  are computed from the "Arc 2", "Arc 1" and "Arc 3" diameters respectively. The shape of the three semicircles, needed to find the diameters values, were derived considering Fig.3.17 and using the best shape-preserving fitting (provided by Matlab software) for the three arcs. Therefore, the following values were derived:  $R_{S_{FTO}} \approx 42.5\Omega$ ,  $R_{Pt} \approx 250\Omega$ ,  $R_{TiO_2} \approx 620\Omega$  and  $R_{Elec} \approx 120\Omega$ . Thus, a total module resistance  $R \approx 1k\Omega$  is obtained. To conclude this part regarding DSSCs EIS, it should be noted that in some cases the Nyquist plot may show an inductive behaviour (the imaginary part of the impedance can assume positive values). This behaviour can be seen at high frequency, because of the inductance of the electrical wiring, or even at low frequency for exemple when a solid-state electrolyte is used[28].

### 3.5.2 Indoor Measurements

As the object of this master thesis was to build a energy harvesting and storage system for indoor applications, the DSSCs module built was tested under different artificial light sources, namely a LED lamp, a fluorescent lamp and a halogen lamp. The dedicated experimental setup used to perform the indoor conditions measurements is reported in Fig.3.18:

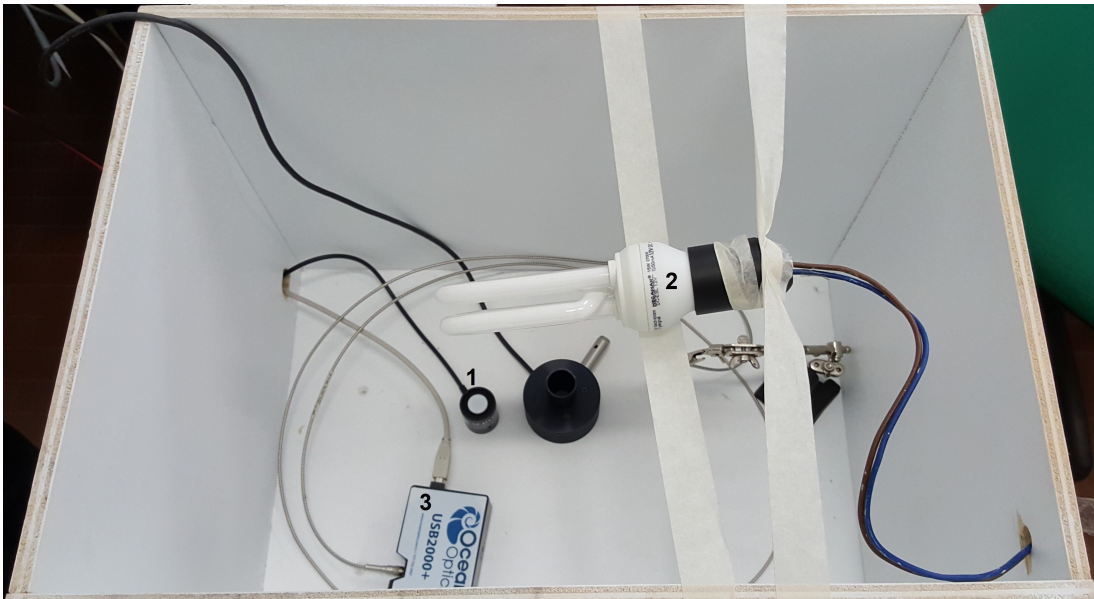


Figure 3.18: Indoor measurements setup

Where:

- 1) Luxmeter
- 2) Lamp
- 3) Spectrometer

It can be seen that a wooden box with dimensions  $70 \times 40 \times 40\text{cm}^3$  was employed as the measurement chamber. The interior walls of the box were covered with a white water-paint in order to simulate the diffused light conditions typical of an indoor

environment [53]. The lamps were placed on the top of the box in a central position, as shown in Fig.3.18, and a luxmeter (by DeltaOhm) together with a *Kipp&Zonen* pyranometer CMP10 were used to evaluate the illuminance and the incident power respectively. It is to be remarked that the luxmeter gives a measure of the light intensity as it is perceived by the human eye response, thus it does not coincide with the incident power, which should be known in order to evaluate the module performance. That is the reason why the pyranometer is needed.

The V-J characteristics under different indoor illumination conditions are reported in figures: 3.19, 3.20 and 3.21 for the LED lamp, the fluorescent lamp and the halogen lamp respectively. More details about the parameters values are, instead, reported in tables: 3.7, 3.8 and 3.9.

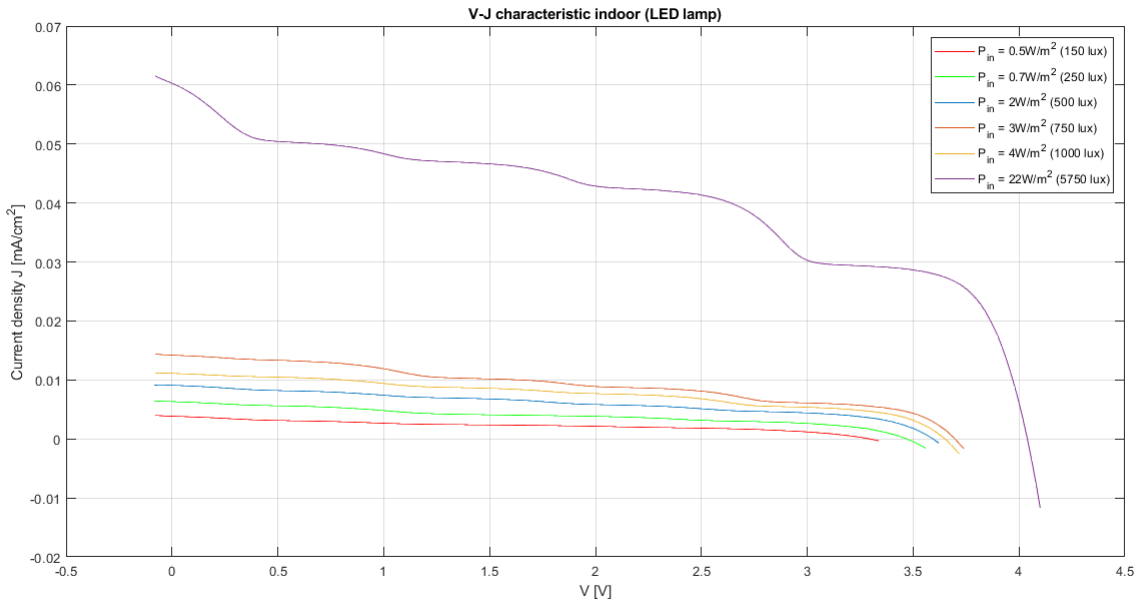


Figure 3.19: V-J curve indoor measurements LED lamp

Table 3.7: Results under different indoor illumination conditions (LED)

$P_{IN}$	$\frac{0.5W}{m^2}$	$\frac{0.7W}{m^2}$	$\frac{2W}{m^2}$	$\frac{3W}{m^2}$	$\frac{4W}{m^2}$	$\frac{22W}{m^2}$
Lux	150	250	500	750	1000	6750
Area( $cm^2$ )	5.74	5.74	5.74	5.74	5.74	5.74
$I_{SC}$ (A)	$2.2 \cdot 10^{-5}$	$3.62 \cdot 10^{-5}$	$5.2 \cdot 10^{-5}$	$8.12 \cdot 10^{-5}$	$6.36 \cdot 10^{-5}$	$3.45 \cdot 10^{-4}$
$V_{OC}$ (V)	3.3	3.47	3.6	3.7	3.65	4.01
$P_{MAX}$ (W)	$2.63 \cdot 10^{-5}$	$4.65 \cdot 10^{-5}$	$7.58 \cdot 10^{-5}$	$1.16 \cdot 10^{-4}$	$9.8 \cdot 10^{-5}$	$6.03 \cdot 10^{-4}$
$I_{MAX}$ (A)	$1 \cdot 10^{-5}$	$1.65 \cdot 10^{-5}$	$2.53 \cdot 10^{-5}$	$4.67 \cdot 10^{-5}$	$4.05 \cdot 10^{-5}$	$2.27 \cdot 10^{-4}$
$V_{MAX}$ (V)	2.62	2.82	3	2.48	2.42	2.66
FF	0.36	0.37	0.41	0.39	0.42	0.43
Eff(%)	9.1	10.12	6.69	6.8	4.25	4.8
$J_{SC}$ ( $\frac{mA}{cm^2}$ )	$3.85 \cdot 10^{-3}$	$6.34 \cdot 10^{-3}$	$9.1 \cdot 10^{-3}$	$1.42 \cdot 10^{-2}$	$1.11 \cdot 10^{-2}$	$6.03 \cdot 10^{-2}$

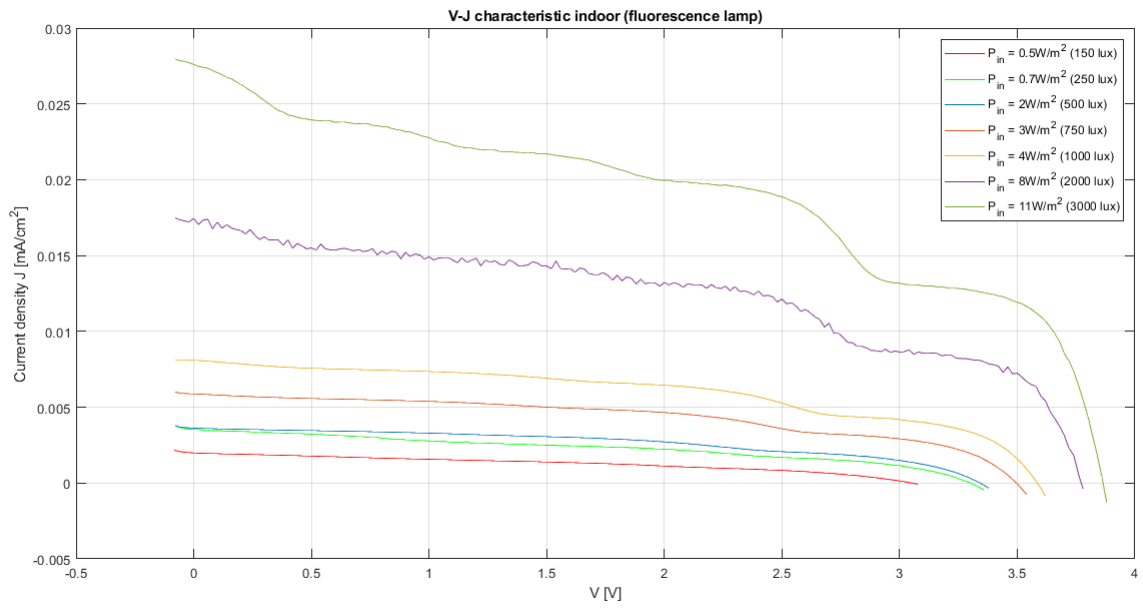


Figure 3.20: V-J curve indoor measurements fluorescent lamp

Table 3.8: Results under different indoor illumination conditions (fluo. lamp)

$P_{IN}$	$\frac{0.5W}{m^2}$	$\frac{0.7W}{m^2}$	$\frac{2W}{m^2}$	$\frac{3W}{m^2}$	$\frac{4W}{m^2}$	$\frac{8W}{m^2}$	$\frac{11W}{m^2}$
LUX	150	250	500	750	1000	2000	3000
Area( $cm^2$ )	5.74	5.74	5.74	5.74	5.74	5.74	5.74
$I_{SC}$ (A)	$1.14 \cdot 10^{-5}$	$2.01 \cdot 10^{-5}$	$2.07 \cdot 10^{-5}$	$3.36 \cdot 10^{-5}$	$4.62 \cdot 10^{-5}$	$9.97 \cdot 10^{-5}$	$1.58 \cdot 10^{-4}$
$V_{OC}$ (V)	3.05	3.3	3.34	3.5	3.59	3.77	3.86
$P_{MAX}$ (W)	$1.3 \cdot 10^{-5}$	$2.59 \cdot 10^{-5}$	$3.12 \cdot 10^{-5}$	$5.49 \cdot 10^{-5}$	$7.86 \cdot 10^{-5}$	$1.73 \cdot 10^{-4}$	$2.71 \cdot 10^{-4}$
$I_{MAX}$ (A)	$6.91 \cdot 10^{-6}$	$1.19 \cdot 10^{-5}$	$1.48 \cdot 10^{-5}$	$2.48 \cdot 10^{-5}$	$3.42 \cdot 10^{-5}$	$7.23 \cdot 10^{-5}$	$1.05 \cdot 10^{-4}$
$V_{MAX}$ (V)	1.88	2.18	2.1	2.22	3	2.4	2.58
FF	0.37	0.39	0.45	0.47	0.47	0.46	0.44
Eff(%)	4.49	6.43	2.71	3.21	3.4	3.77	5.8
$J_{SC}$ ( $\frac{mA}{cm^2}$ )	$1.99 \cdot 10^{-3}$	$3.52 \cdot 10^{-3}$	$3.62 \cdot 10^{-3}$	$5.88 \cdot 10^{-3}$	$8.09 \cdot 10^{-3}$	$1.74 \cdot 10^{-2}$	$2.76 \cdot 10^{-2}$

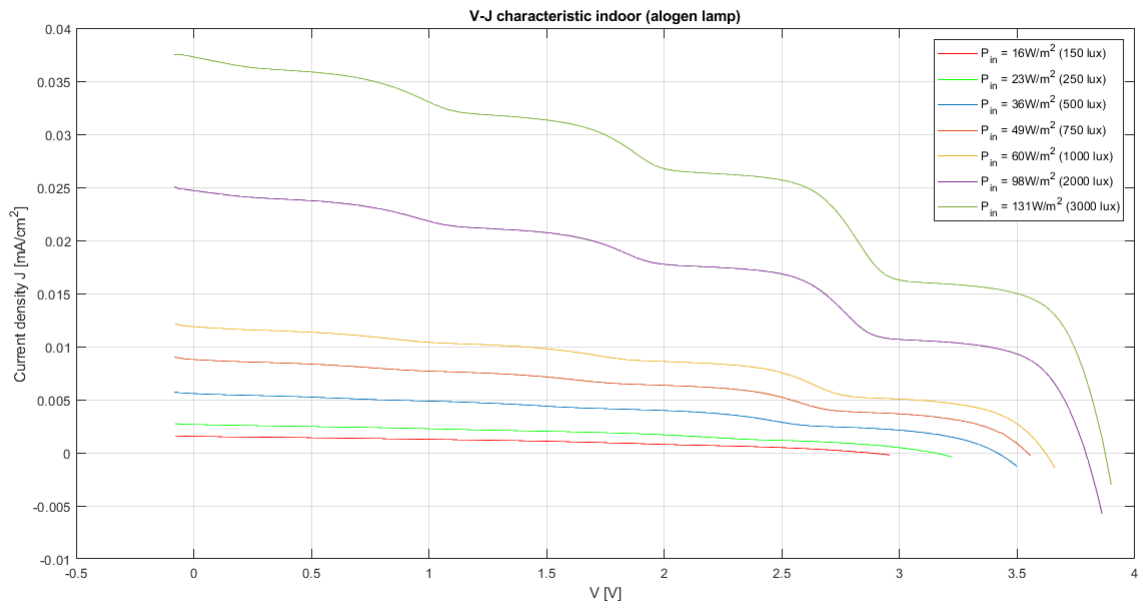


Figure 3.21: V-J curve indoor measurements halogen lamp

Table 3.9: Results under different indoor illumination conditions (halogen lamp)

$P_{IN}$	$\frac{16W}{m^2}$	$\frac{23W}{m^2}$	$\frac{36W}{m^2}$	$\frac{49W}{m^2}$	$\frac{60W}{m^2}$	$\frac{98W}{m^2}$	$\frac{131W}{m^2}$
LUX	150	250	500	750	1000	2000	3000
Area( $cm^2$ )	5.74	5.74	5.74	5.74	5.74	5.74	5.74
$I_{SC}$ (A)	$8.83 \cdot 10^{-6}$	$1.52 \cdot 10^{-5}$	$3.18 \cdot 10^{-5}$	$5.02 \cdot 10^{-5}$	$6.79 \cdot 10^{-5}$	$1.41 \cdot 10^{-4}$	$2.13 \cdot 10^{-4}$
$V_{OC}$ (V)	2.86	3.14	3.41	3.54	3.62	3.79	3.87
$P_{MAX}$ (W)	$9.56 \cdot 10^{-6}$	$1.94 \cdot 10^{-5}$	$4.7 \cdot 10^{-5}$	$7.87 \cdot 10^{-5}$	$1.1 \cdot 10^{-4}$	$2.41 \cdot 10^{-4}$	$3.72 \cdot 10^{-4}$
$I_{MAX}$ (A)	$5.14 \cdot 10^{-6}$	$1 \cdot 10^{-5}$	$2.13 \cdot 10^{-5}$	$3.36 \cdot 10^{-5}$	$4.57 \cdot 10^{-5}$	$9.5 \cdot 10^{-5}$	$1.43 \cdot 10^{-4}$
$V_{MAX}$ (V)	1.86	1.94	2.2	2.34	2.4	2.54	2.6
FF	0.38	0.41	0.43	0.44	0.45	0.45	0.45
Eff(%)	0.11	0.15	0.23	0.28	0.32	0.43	0.5
$J_{SC}$ ( $\frac{mA}{cm^2}$ )	$1.54 \cdot 10^{-3}$	$2.66 \cdot 10^{-3}$	$5.57 \cdot 10^{-3}$	$8.78 \cdot 10^{-3}$	$1.19 \cdot 10^{-2}$	$2.47 \cdot 10^{-2}$	$3.73 \cdot 10^{-2}$

As it can be seen from the values reported in the previous tables, the FF measured for the three different lamps shows comparable values between 0.36 and 0.47, while, as regards the efficiencies, the values are very different. For example, we have an efficiency greater than 10% for the LED lamp and lower than 1% for the halogen one. This huge difference should not be ascribed to the different illumination technology, but to the fact that, being the halogen lamp a spotlight (see Fig.3.22), the radiation is much more directional, leading to an incident power which is not widespread all over the module. In fact, the incident power is very high in a small spot of the total module photoactive area and almost zero everywhere, as reported in Fig.3.23; this dramatically reduces the efficiency.



Figure 3.22: Halogen spotlight

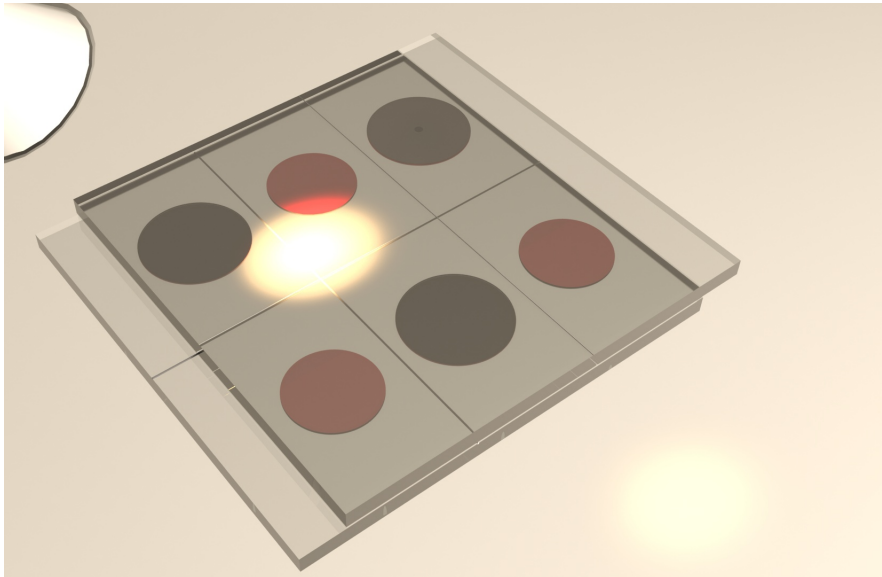


Figure 3.23: Halogen spotlight illumination

It is important to note that the maximum efficiency under indoor enlightenment is equal to 10.12%, one of the highest values reported in literature at the best of my knowledge, and is obtained for a LED lamp under 250 lux, which is a very common place illumination condition for indoor environments.

Fig.3.24

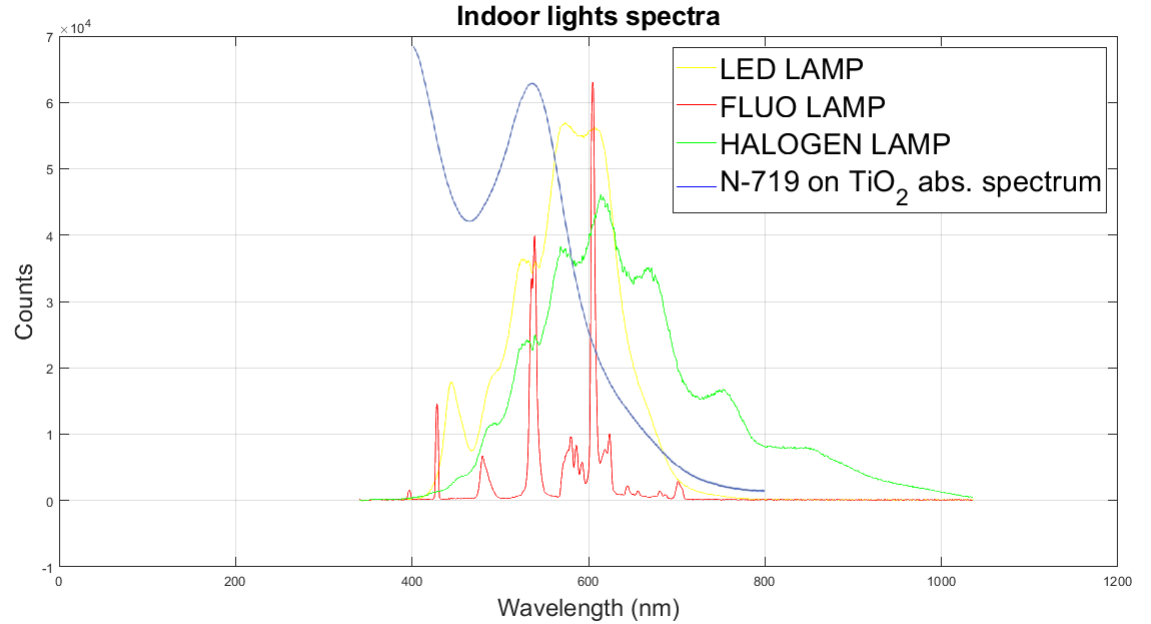


Figure 3.24: Lamps emission spectra and N-719 dye on  $TiO_2$  absorptium spectrum

As it can be seen from Fig.3.24, the LED lamp is the one showing the highest efficiency because of its emission spectrum. In fact, the absorption spectrum of the dye has a peak around 530 nm, where the LED lamp has the highest emission among the three indoor light sources. More in details, the LED lamp emission spectrum is the one showing the greatest overlap with the N-719 absorption spectrum, thus ensuring a greater quantum efficiency for the photovoltaic module.

In order to improve indoor features, De Rossi et Al. [54] showed that a possible boost is to lower the electrolyte concentration to enhance transparency and, thus, improving the cell efficiency. Even though usual illumination conditions in indoor environments are about 200 lux [54], 1000 lux have been considered in Fig.3.25 to give an immediate feeling of the three kind of lamps features comparison. This choice was carried out considering that 1000 lux is a conservative estimation of the illuminance measured under a desk lamp, giving a quite practical exemple of an indoor methode of use.

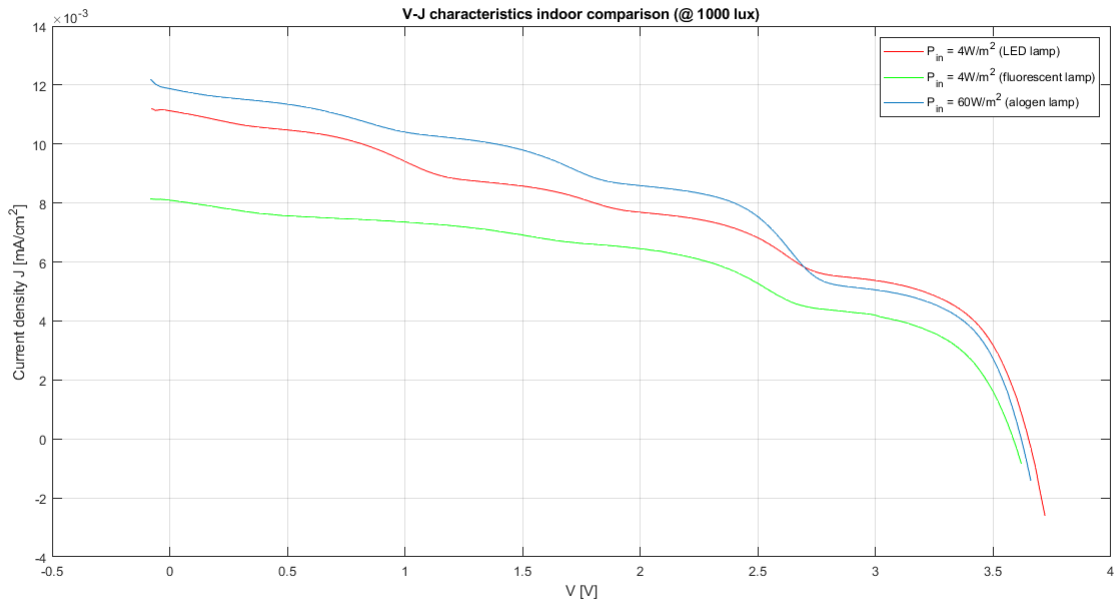


Figure 3.25: V-J curves indoor comparison (@ 1000lux)

### 3.5.3 Module stability with respect to time

In order to assess the stability with respect to time of this "home-made" module, even though no particular care was taken in ensuring a long-cycle life to the device, its performance where measured on different days. More in details, The V-J characteristic was measured as soon as the module was built, 2 days after, then after almost three months and finally again after a few days. In this way, it was possible to investigate the effects of both short and long periods of time. The results obtained are reported in Fig.3.26 and in Table3.10.

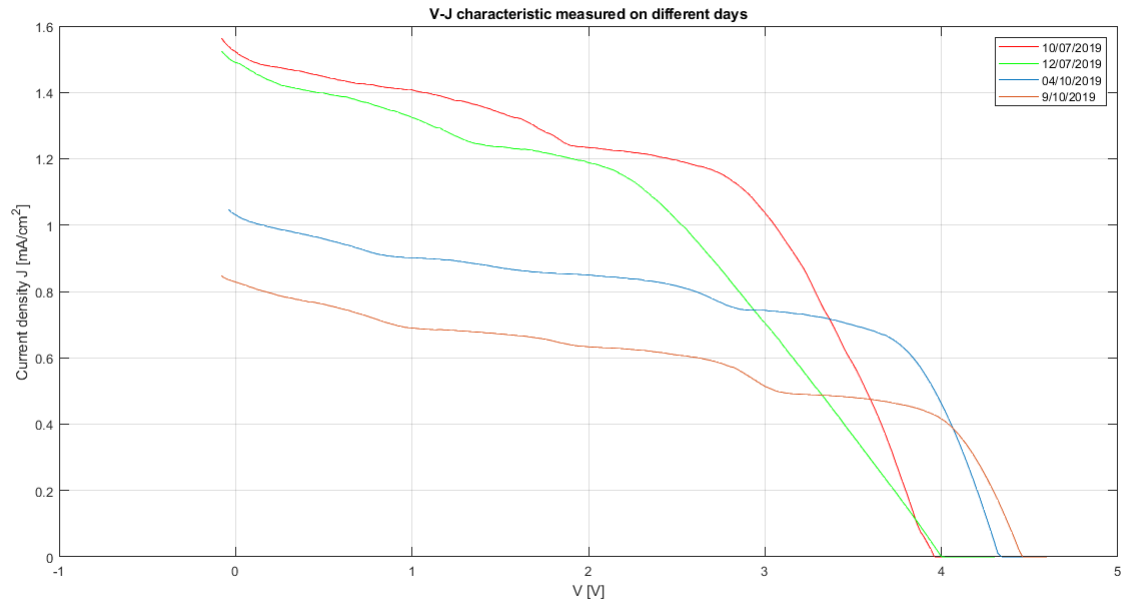


Figure 3.26: V-J curves measured on different days

Table 3.10: V-J curves measured on different days.

Parameter	10/07/2019	12/07/2019	04/10/2019	14/10/2019
Area( $cm^2$ )	5.74	5.74	5.74	5.74
$I_{SC}$ (A)	$8.75 \cdot 10^{-3}$	$8.57 \cdot 10^{-3}$	$5.93 \cdot 10^{-3}$	$4.73 \cdot 10^{-3}$
$V_{OC}$ (V)	3.96	4	4.33	4.45
$P_{MAX}$ (W)	$1.84 \cdot 10^{-2}$	$1.47 \cdot 10^{-2}$	$1.42 \cdot 10^{-2}$	$9.9 \cdot 10^{-3}$
$I_{MAX}$ (A)	$6.46 \cdot 10^{-3}$	$6.15 \cdot 10^{-3}$	$3.9 \cdot 10^{-3}$	$2.6 \cdot 10^{-3}$
$V_{MAX}$ (V)	2.84	2.4	3.62	3.8
FF	0.53	0.43	0.55	0.47
Eff(%)	3.19	2.57	2.46	1.73
$J_{SC}$ ( $\frac{mA}{cm^2}$ )	1.52	1.49	1.03	$8.28 \cdot 10^{-1}$

It can be seen that, as it was expected, the DSSC properties are degraded. More in details, it is observed that the efficiency is dramatically reduced and this is due to the fact that  $J_{SC}$  is heavily lowered. The photogenerated current reduction is mainly due to the decrease of the photon injection efficiency of the dye which undergoes degradation under illumination and desorption due to the reaction with  $I_3^-$  of the electrolyte[55]. On the other hand, the efficiency degradation is reduced by the  $V_{OC}$  increase which can be explained through the decrease in the  $I_3^-$  concentration (electrolyte bleaching) according to equation 2.1. When using aqueous electrolytes the  $J_{SC}$  is furtherly decreased and the  $V_{OC}$  is furtherly increased as reported in [56] and [57]. Considering that the DSSCs module was not sealed industrially, the effects of humidity and aqueous vapor may not be negligible causing a variation of the  $V_{OC}$ .

### 3.6 Energy harvesting module with transparent $TiO_2$ round photoanodes

In order to allow a direct integration of the DSSC modules in buildings windows and expand their field of use, another device was built using a transparent titania paste, performing the fabrication steps reported in 2. It is clear that making the photoanodes transparent would imply an increase in transmittance, therefore enhancing the incident power and the photogenerated current, when using the back-mirroring configuration. On the other hand, it should be considered that the transparent titania paste, unlike the opaque one, does not contain the scattering  $TiO_2$  particles that, diffusing light, increase the incident power. So, a certain worsening of the device performance is to be expected. The final device is reported in Fig.3.27.

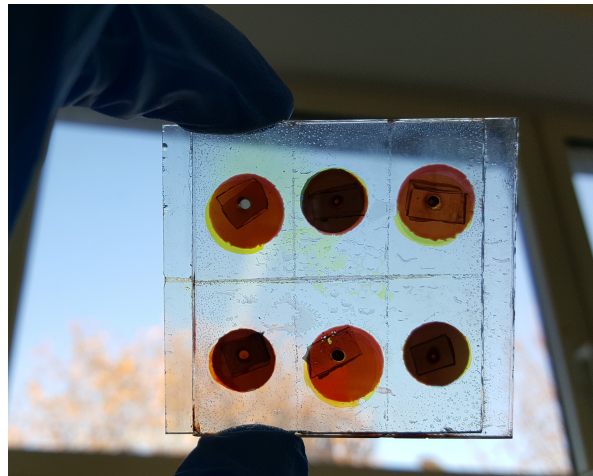


Figure 3.27: Energy harvesting module

Fig.3.28 reports the V-J curve of the module and Table3.11 shows the measured parameters values.

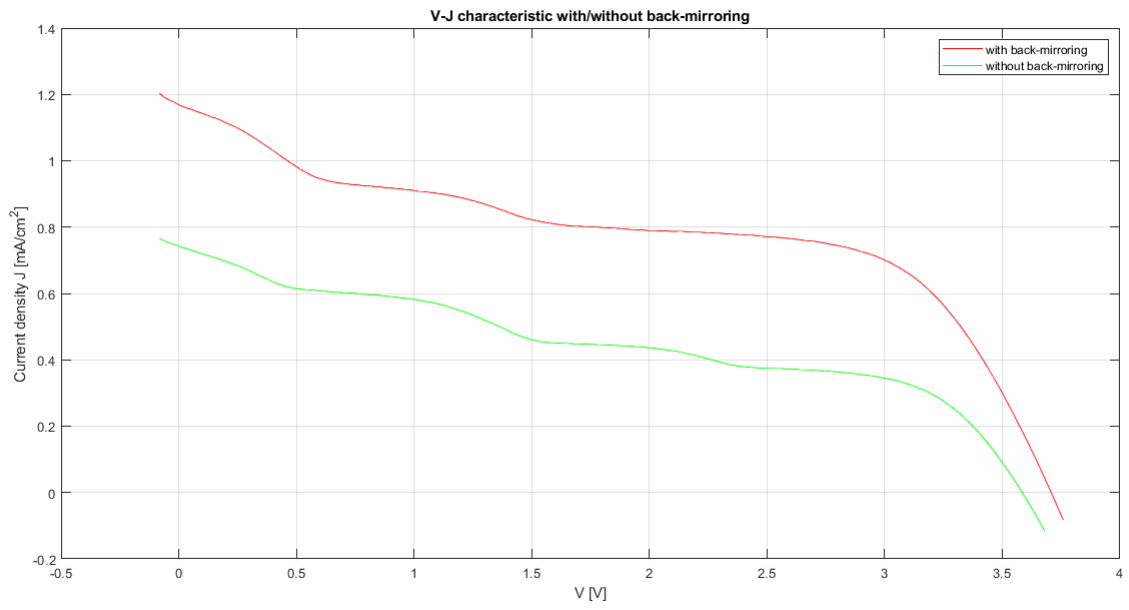


Figure 3.28: V-J curve transparent  $TiO_2$  module (device1)

Table 3.11: Module parameters transparent  $TiO_2$  (device1)

Parameter	with back-mirror	w/out back-mirror
Area( $cm^2$ )	5.74	5.74
$I_{SC}$ (A)	$6.71 \cdot 10^{-3}$	$4.27 \cdot 10^{-3}$
$V_{OC}$ (V)	3.71	3.58
$P_{MAX}$ (W)	$1.21 \cdot 10^{-2}$	$5.95 \cdot 10^{-3}$
$I_{MAX}$ (A)	$4.1 \cdot 10^{-3}$	$2.02 \cdot 10^{-3}$
$V_{MAX}$ (V)	2.96	2.94
FF	0.49	0.39
Eff(%)	2.11	1.04
$J_{SC}$ ( $\frac{mA}{cm^2}$ )	1.17	$7.42 \cdot 10^{-1}$

It can be seen that, as expected, the device features have worsen with respect to the opaque titania module. However, there is an effective improvement in the boost given by the back-mirroring, as it was predicted above. A more clear feel of the different performance of transparent and opaque titania photoanodes modules will be given in 3.37. In order to check the results obtained with this first attempt and to assess repeatability, another module was built nominally identycal to the previous one. This time, besides the classical V-J characteristic under 1 SUN and with or without back-mirroring, also the V-J curves under different illumination conditions were plotted. But, as the device performance in normal conditions were really poor, even worse than the previous module, the values reported in Table3.13 have been obtained in the back-mirroring configuration.

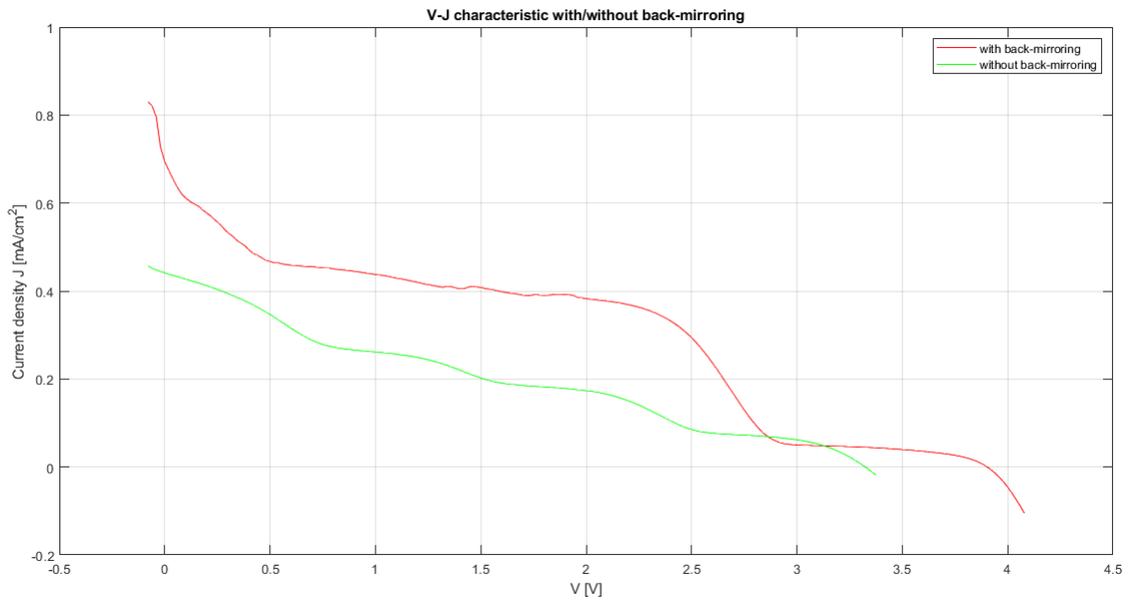


Figure 3.29: V-J curve transparent  $\text{TiO}_2$  module (device2)

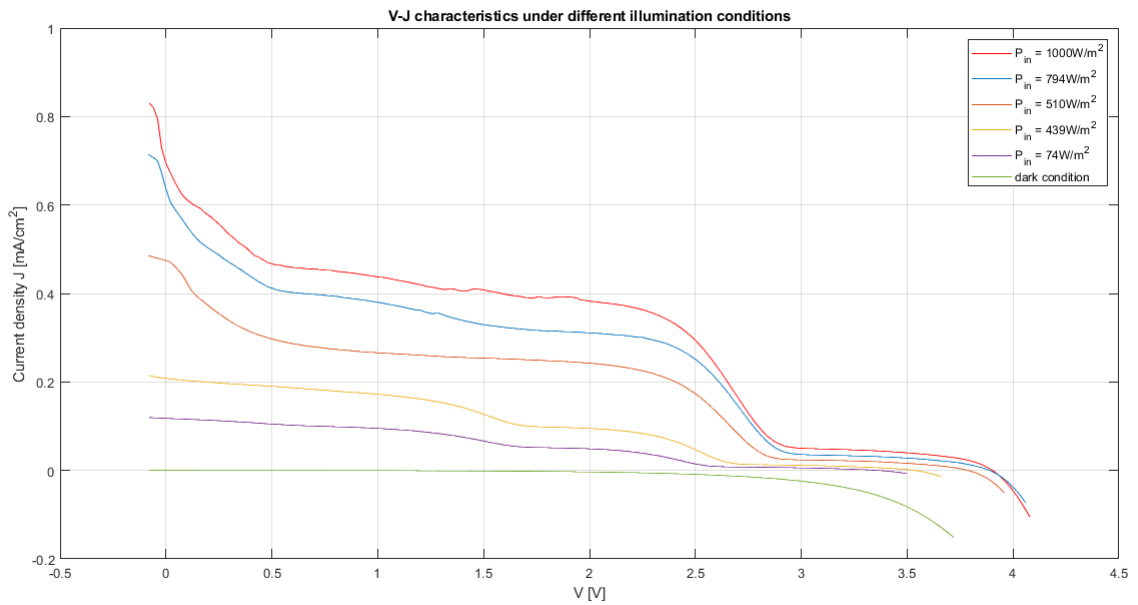


Figure 3.30: V-J curves under different illumination conditions transparent  $\text{TiO}_2$  (device 2)

Table 3.12: Module parameters transparent  $TiO_2$  (device2)

Parameter	with back-mirror	w/out back-mirror
Area( $cm^2$ )	5.74	5.74
$I_{SC}$ (A)	$3.99 \cdot 10^{-3}$	$2.54 \cdot 10^{-3}$
$V_{OC}$ (V)	3.9	3.32
$P_{MAX}$ (W)	$4.69 \cdot 10^{-3}$	$2 \cdot 10^{-3}$
$I_{MAX}$ (A)	$2.06 \cdot 10^{-3}$	$9.74 \cdot 10^{-4}$
$V_{MAX}$ (V)	2.28	2.06
FF	0.3	0.24
Eff(%)	0.82	0.35
$J_{SC}$ ( $\frac{mA}{cm^2}$ )	$6.94 \cdot 10^{-1}$	$4.41 \cdot 10^{-1}$

Table 3.13: Module parameters with back-mirroring under different illumination conditions (device 2)

Parameter	$P_{in} = \frac{1000W}{m^2}$	$P_{in} = \frac{794W}{m^2}$	$P_{in} = \frac{510W}{m^2}$	$P_{in} = \frac{439W}{m^2}$	$P_{in} = \frac{74W}{m^2}$
Area( $cm^2$ )	5.74	5.74	5.74	5.74	5.74
$I_{SC}$ (A)	$3.99 \cdot 10^{-3}$	$3.65 \cdot 10^{-3}$	$2.72 \cdot 10^{-3}$	$1.19 \cdot 10^{-3}$	$6.76 \cdot 10^{-4}$
$V_{OC}$ (V)	3.9	3.89	3.79	3.54	3.36
$P_{MAX}$ (W)	$4.69 \cdot 10^{-3}$	$3.89 \cdot 10^{-3}$	$2.91 \cdot 10^{-3}$	$1.15 \cdot 10^{-3}$	$6.16 \cdot 10^{-4}$
$I_{MAX}$ (A)	$2.06 \cdot 10^{-3}$	$1.68 \cdot 10^{-3}$	$1.31 \cdot 10^{-3}$	$8.59 \cdot 10^{-4}$	$4.74 \cdot 10^{-4}$
$V_{MAX}$ (V)	2.28	2.32	2.22	1.34	1.3
FF	0.3	0.27	0.28	0.27	0.27
Eff(%)	0.82	0.81	0.93	0.82	0.82
$J_{SC}$ ( $\frac{mA}{cm^2}$ )	$6.94 \cdot 10^{-1}$	$6.36 \cdot 10^{-1}$	$4.75 \cdot 10^{-1}$	$2.08 \cdot 10^{-1}$	$1.18 \cdot 10^{-1}$

The main reason why the features of this second attempt were worsen with respect to the previous one have to be found in the detaching of the  $TiO_2$  paste after the sintering process and the immersion in the dye solution (see Fig.3.31). This phenomenon can be due to a non properly successful doctor blade  $TiO_2$  deposition. Another detrimental element of this second module is to be found in the poor quality of the Pt layer, which shows evident inhomogeneities, as can be seen in Fig.3.31

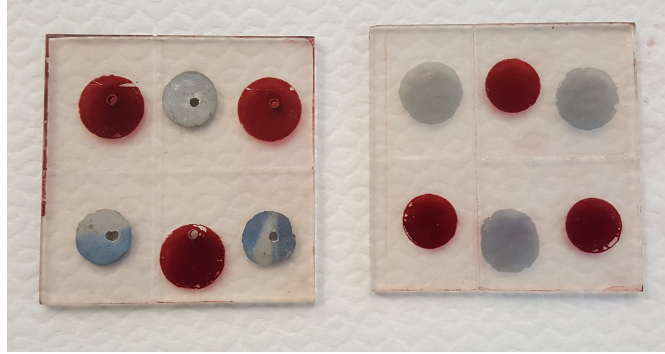


Figure 3.31: Damaged photoanodes

### 3.7 Energy harvesting module with transparent $TiO_2$ squared photoanodes

In order to try to overcome the issues faced in section 3.6, therefore trying to maximize the photoactive area with respect to the geometrical one and reduce the un-effective surfaces of the module, this time another DSSCs energy harvesting device was built, always following the fabrication steps described in 2, using squared electrodes. The chosen sides where 1cm for the front-illuminated cells and 1.2cm for the back illuminated ones. This new design should increase the photoactive area and therefore the efficiency of the module. A possible drawback may be a decrease of the FF due to an expected increase in the sheet resistance caused by the bigger surface [51]. The two substrates are depicted in Fig.3.32, while the final device is shown in Fig.3.33.

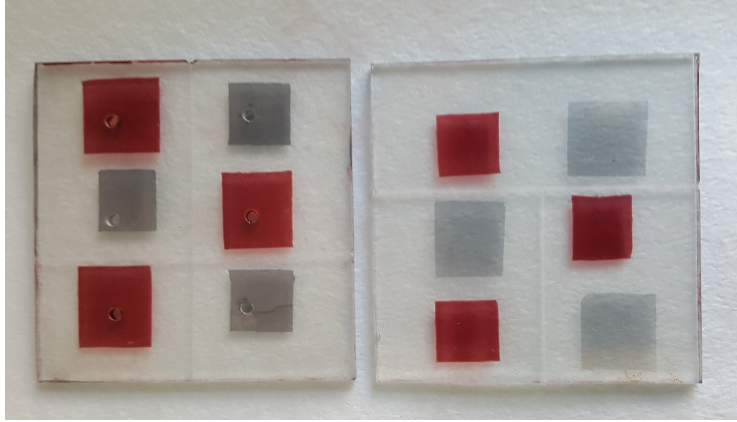


Figure 3.32: Squared electrodes (balanced)

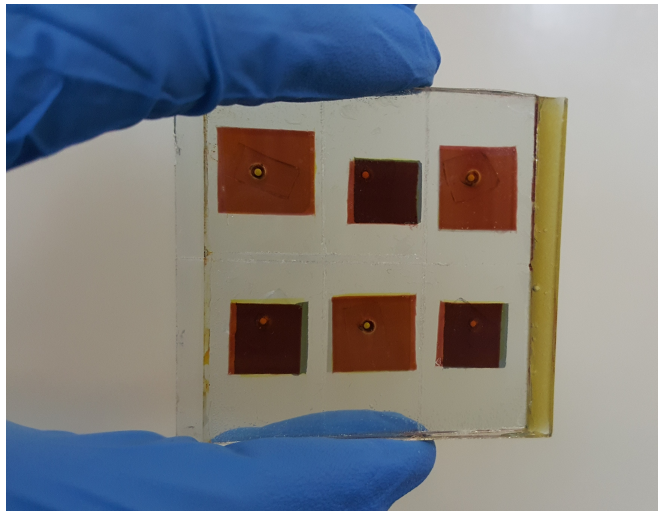


Figure 3.33: DSSCS module with squared electrodes

The V-J curve for the squared electrodes module is reported in Fig.3.34. Measurements have also been carried out under different illumination conditions (see Fig.3.35) always using the back-mirror configuration to better exploit the transparent titania features. As can be read out from the plots and the related tables, both efficiency and FF are quite better than the ones reported in section 3.6 for round electrodes module. Thus, according to the experimental results, the surface increase has led to just positive effects for the overall performance of the module

and, moreover, the simpler geometrical shape allows a higher precision in making front and back-illuminated cells properly matching, reducing current mismatch and the related step-wise behaviour of the V-J characteristic.

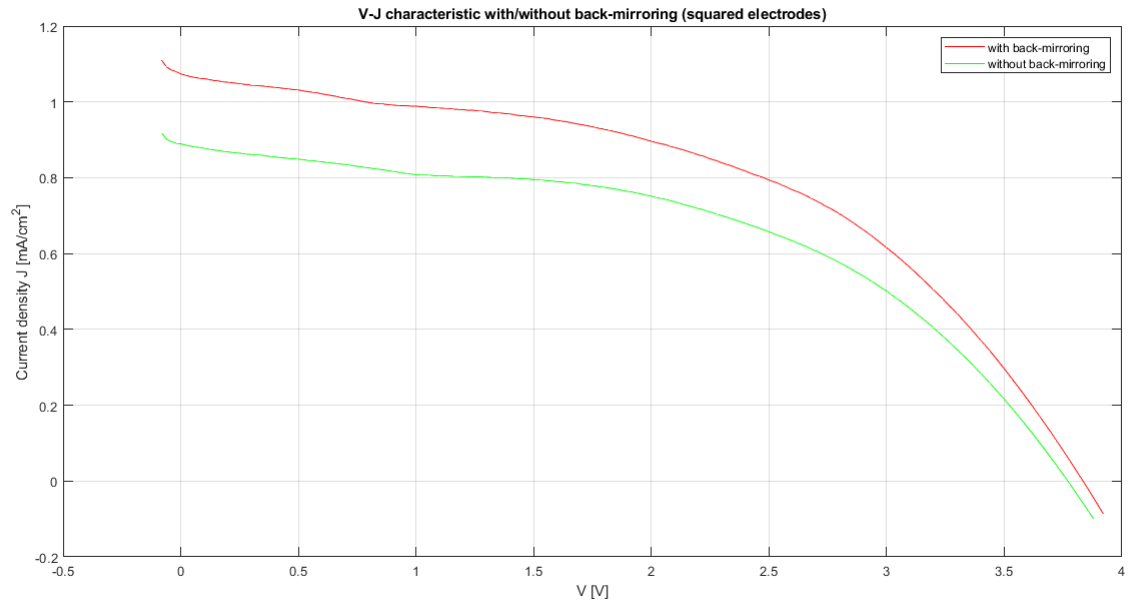


Figure 3.34: V-J curve with/without back-mirroring (squared electrodes)

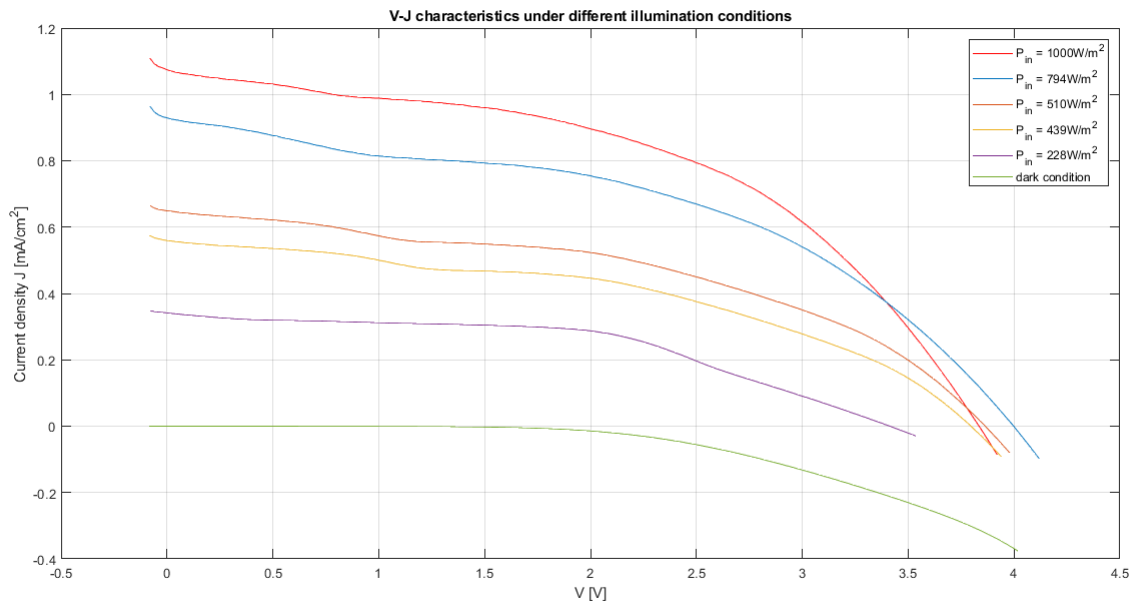


Figure 3.35: V-J curves under different illumination conditions (squared electrodes)

Table 3.14: Module parameters transparent  $TiO_2$  (squared electrodes)

Parameter	with back-mirror	w/out back-mirror
Area( $cm^2$ )	7.3	7.3
$I_{SC}$ (A)	$7.84 \cdot 10^{-3}$	$6.49 \cdot 10^{-3}$
$V_{OC}$ (V)	3.83	3.77
$P_{MAX}$ (W)	$1.46 \cdot 10^{-2}$	$1.2 \cdot 10^{-2}$
$I_{MAX}$ (A)	$5.49 \cdot 10^{-3}$	$4.63 \cdot 10^{-3}$
$V_{MAX}$ (V)	2.66	2.6
FF	0.49	0.49
Eff(%)	2	1.65
$J_{SC}$ ( $\frac{mA}{cm^2}$ )	1.07	$8.89 \cdot 10^{-1}$

Table 3.15: Module parameters under different illumination conditions (squared electrodes)

Parameter	$P_{in} = \frac{1000W}{m^2}$	$P_{in} = \frac{794W}{m^2}$	$P_{in} = \frac{510W}{m^2}$	$P_{in} = \frac{410W}{m^2}$	$P_{in} = \frac{288W}{m^2}$
Area( $cm^2$ )	7.3	7.3	7.3	7.3	7.3
$I_{SC}$ (A)	$7.84 \cdot 10^{-3}$	$6.78 \cdot 10^{-3}$	$4.74 \cdot 10^{-3}$	$4.1 \cdot 10^{-3}$	$2.49 \cdot 10^{-3}$
$V_{OC}$ (V)	3.83	4	3.86	3.8	3.41
$P_{MAX}$ (W)	$1.46 \cdot 10^{-2}$	$1.23 \cdot 10^{-2}$	$8.22 \cdot 10^{-3}$	$6.89 \cdot 10^{-3}$	$4.25 \cdot 10^{-3}$
$I_{MAX}$ (A)	$5.49 \cdot 10^{-3}$	$4.64 \cdot 10^{-3}$	$3.26 \cdot 10^{-3}$	$2.87 \cdot 10^{-3}$	$2.03 \cdot 10^{-3}$
$V_{MAX}$ (V)	2.66	2.66	2.52	2.4	2.1
FF	0.49	0.45	0.45	0.44	0.5
Eff(%)	2	2.14	2.21	2.15	2.56
$J_{SC}$ ( $\frac{mA}{cm^2}$ )	1.07	$9.29 \cdot 10^{-1}$	$6.49 \cdot 10^{-1}$	$5.6 \cdot 10^{-1}$	$3.42 \cdot 10^{-1}$

The EIS completes the characterization of this squared electrodes module allowing a deeper insight in the resistive behaviour of the device. According to what has been stated in 3.5.1, it is possible to read out the different resistive contribution involved in the device structure and working principle directly from the Nyquist plot reported in Fig.3.36. Again, the measurements were performed in dark conditions, under open circuit potential and in the frequency range [0.1Hz,100kHz].

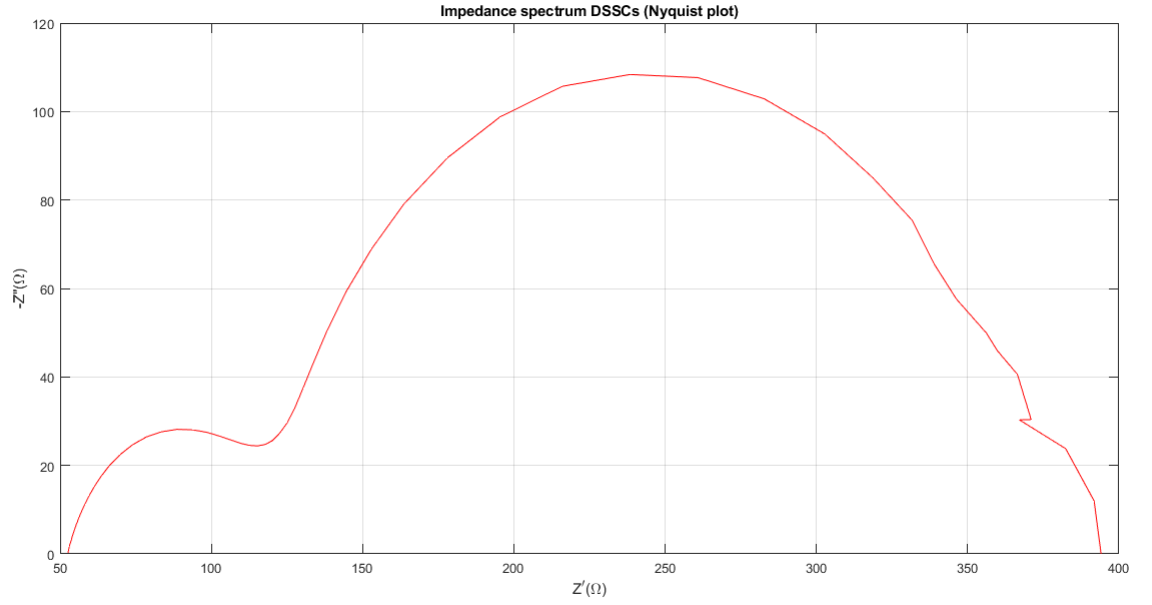


Figure 3.36: Impedance spectrum DSSCs module (Nyquist plot)

Carrying out the steps performed in 3.5.1 we have:  $R_{S_{FTO}} \approx 52\Omega$ ,  $R_{Pt} \approx 80\Omega$ ,  $R_{TiO_2} \approx 270\Omega$  and  $R_{Elec} \approx 90\Omega$ . The total resistance is, therefore, given by:

$$R = R_{S_{FTO}} + R_{TiO_2} + R_{Pt} + R_{Elec} \approx 500\Omega$$

It can be seen that with respect to the previous case in which EIS was performed (The opaque titania module with round electrodes) the resistive behaviour is much lowered. In fact, a part from  $R_{S_{FTO}}$ , that is increased from  $42.5\Omega$  to  $52\Omega$  due to larger area and larger sheet resistance electrodes, all the other resistive contributions are significantly lowered giving a total resistance of  $500\Omega$  instead of  $1k\Omega$ .

### 3.8 Transparent and opaque $TiO_2$ paste: a comparison

In order to give a synoptic picture of the different performances of the modules that were built (with transparent and opaque titania photoanodes, with or without back-mirroring) Fig.3.37 plots the different V-J curves obtained.

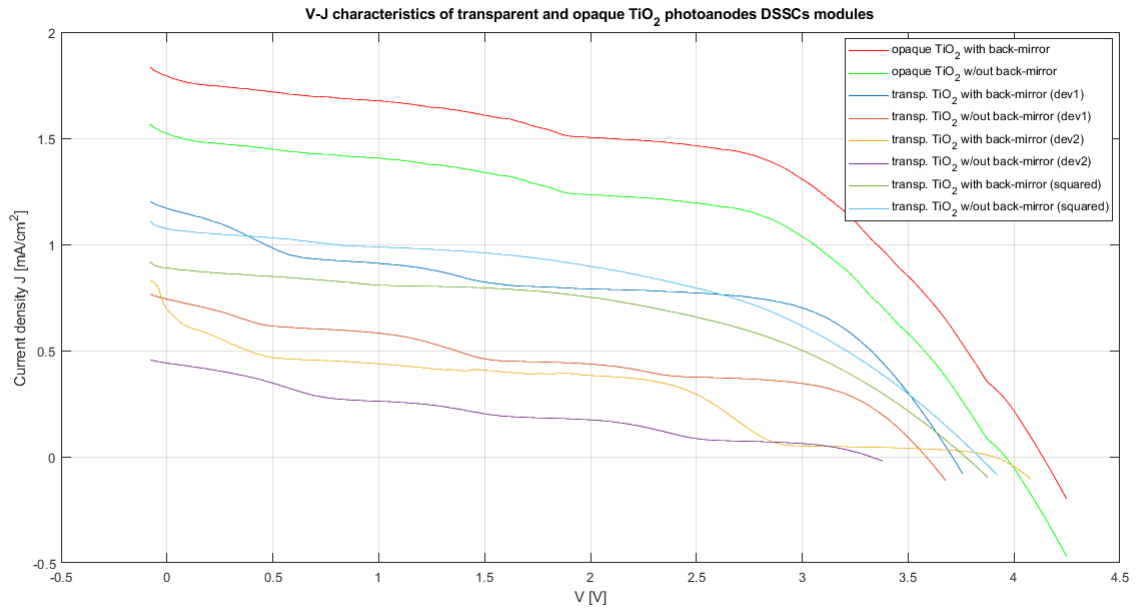


Figure 3.37: V-J curves of transparent and opaque  $TiO_2$  photoanodes DSSCs modules

According to the experimental results found in this work, it seems that the module with the opaque  $TiO_2$  is working quite better than the transparent titania one. In fact, we can see both higher  $V_{OC}$  and higher  $J_{SC}$  values. But still further investigation is needed to verify this point.

### 3.9 HS power-pack system: characterization and testing

The final HS power-pack is made up of the DSSCs module built in section 3.5 connected in parallel to a 33mF commercial supercapacitor by AVX Bestcaps. In order to characterize the overall system and give a measure of its quality, the OPECSE, defined in 1, was computed and plotted with respect to voltage and photo-charge time. More in details, at first the DSSCs module was used to photocharge the supercapacitor and then galvanostatic discharge at different current values were performed as reported in Fig.3.38

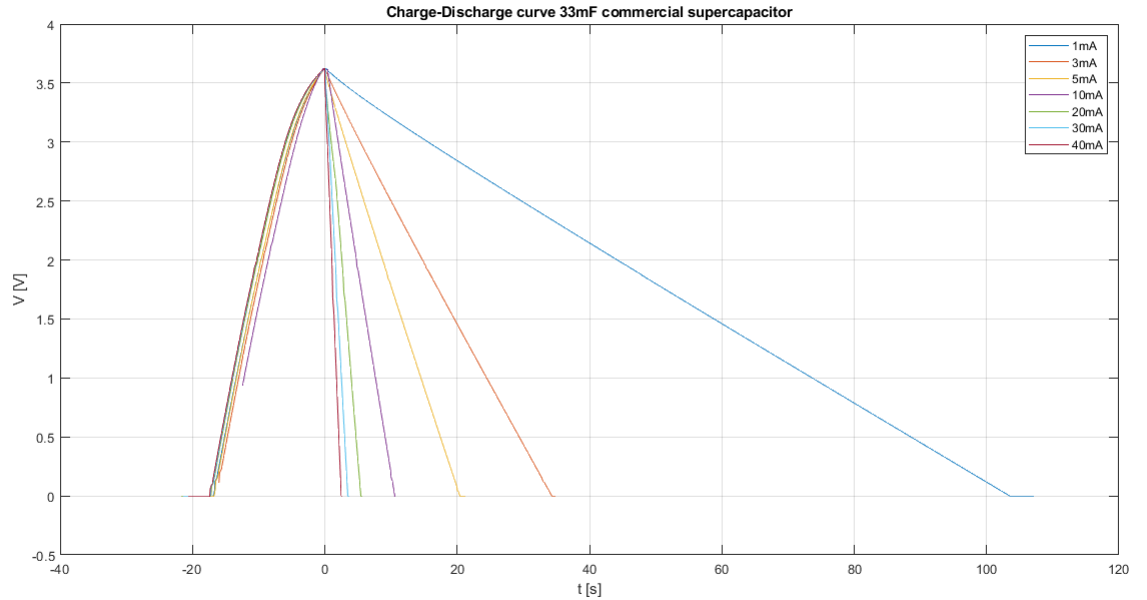


Figure 3.38: Charge and galvanostatic discharge 33mF commercial supercapacitor

From Fig.3.38 we get the information needed to compute the OPECSE according to the known equation:  $\eta(OPECSE) = \frac{0.5CV^2}{GtS}$  where  $C = 33 \cdot 10^{-3}F$ ,  $G = 1000 \frac{W}{m^2}$  and  $5.74 \cdot 10^{-4}$ . Fig.3.39 and 3.40 plot the OPECSE with respect to time and to the voltage across the supercapacitor respectively.

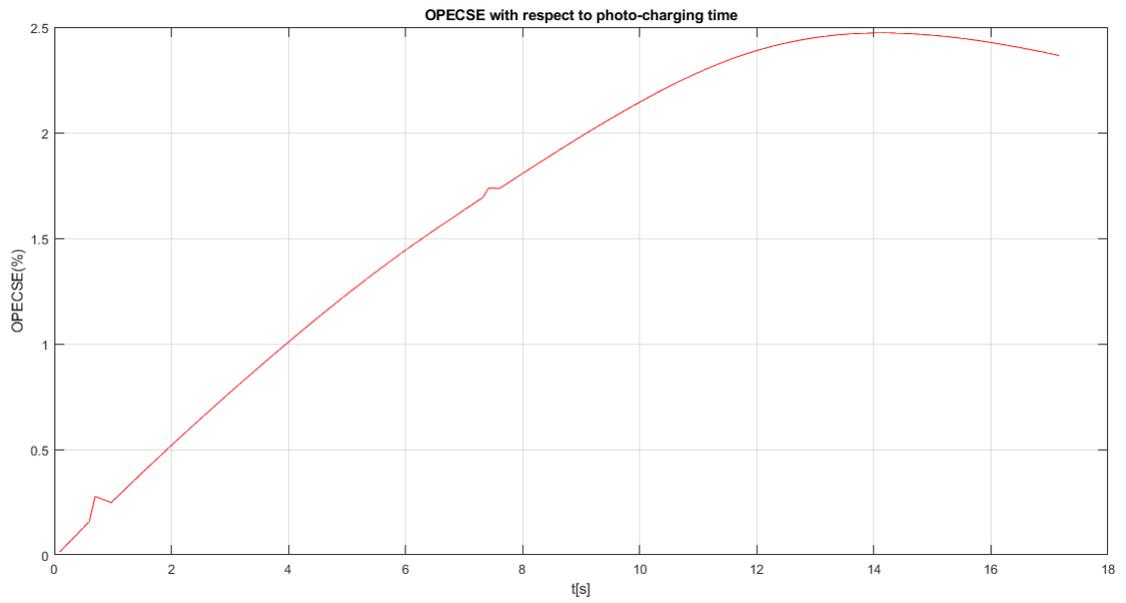


Figure 3.39: OPECSE(%) with respect to photocharging time

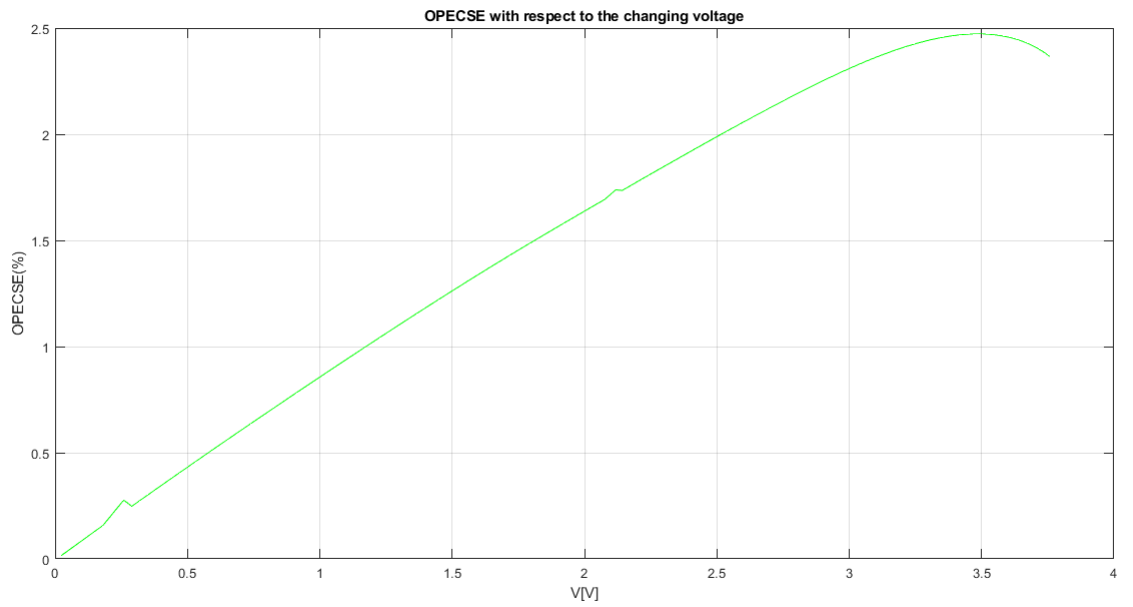


Figure 3.40: OPECSE(%) with respect to the changing voltage

From these plots we can read out that the maximum OPECSE is reached after a

photocharging time  $t_{pc} = 14.18s$  and when the voltage across the supercapacitor  $V$  is equal to  $\approx 3.493V$ .  $OPECSE = 2.473\%$  is the value found for the maximum of this overall photon conversion efficiency and this can be considered a quite good value remembering that being the efficiency of the harvesting module equal to  $3.19\%$  and being the OPECSE also defined as  $\eta(OPECSE) = \eta_{PV}\eta_{STORAGE}$ , its maximum possible value was  $3.19\%$ . So the obtained value is approximately the  $77.6\%$  of the maximum possible result.

### 3.9.1 HS power-pack test

This section is concluded giving a very simple exemple of a possible domestic application of the HS power-pack system built in this thesis. In particular, it was used to power a humidity and temperature sensor. Fig.3.41 shows the parallel connection between the DSSCs module, the commercial supercapacitor and the load(the sensor), which is off. This connection was simply obtained by means of crocodile clips.

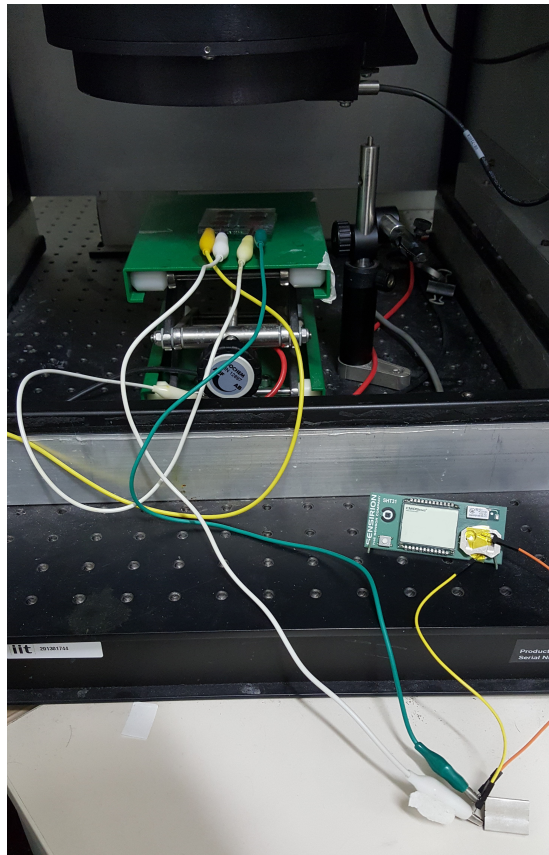


Figure 3.41: Power-pack system test a)

Figure 3.42, instead, shows the device when it is properly working. In fact we see that the energy harvesting device is under illumination conditions, charges the supercapacitor and powers the load which is now on.

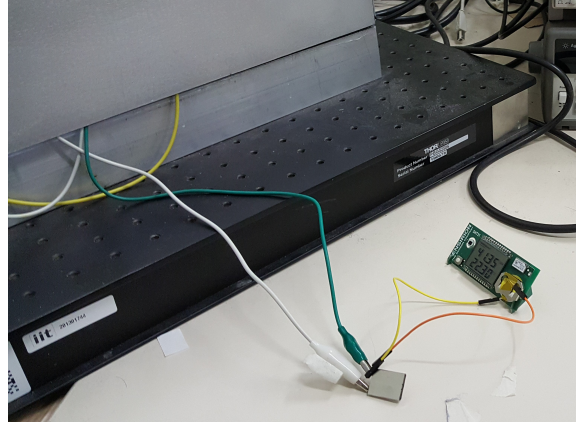


Figure 3.42: Power-pack system test b)

A complete view of the testbench is given in Fig.3.43, that shows the whole experimental setup.

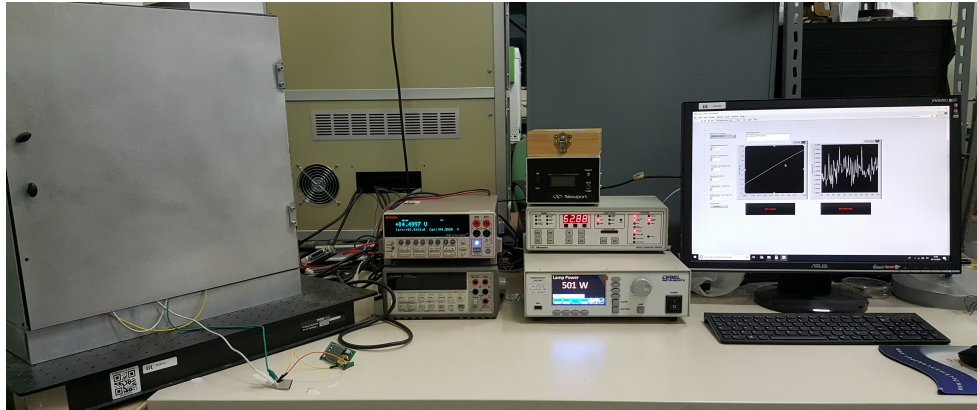


Figure 3.43: Power-pack system testbench

It was observed that the sensor was able to work for a few minutes (about 2-5 minutes) after the shutdown of the light source. In fact, the current needed from the sensor to work is given by the discharge process of the supercapacitor.

# Chapter 4

## Conclusions and future developments

The final power-pack system built in this master thesis was the result of a series of tests, performed to define the proper design and a quite easy and standard fabrication procedure that could allow good performance to the device. In particular, this work was focused on the fabrication of a high voltage energy harvesting module. More in details, a  $V_{OC} = 3.95V$  was achieved under 1 SUN illumination condition, that became 4.11 V when using back-mirroring configuration. It is one of the highest values reported in literature, at the best of my knowledge, for power-pack systems exploiting DSSCs modules as the energy harvesting element. In fact, a similar work was carried out by [58] who develop a power-pack system made up of 6 series-connected DSSCs connected in parallel to a lithium ion battery (LIB). In particular, the energy harvesting part was made up of "three tandem solar cells", where each tandem was constituted by "two series wound DSSCs", a top placed one and a bottom placed one. The former employed N-719 dye as the photo-sensitizer, while the latter employed N-749 dye (black dye) that, being more efficient than the previous one, counterbalances the lower incident power onto the bottom cell trying to uniform the photogenerated current accross the series-connected devices. The top and the bottom cells, just like the three tandem solar cells, are connected in series by using electrical wiring. They got a  $V_{OC}$  equal to 3.39 V[58]. The same idea of realizing high voltage power-pack systems connecting in parallel a DSSCs based

---

energy harvesting element and a LIB was exploited by [59] and [60]. In the former paper a single DSSC was connected in parallel to the LIB exploiting an external low power boost converter reaching an output voltage of 3 V, in the latter one the DSSCs module was made up of just 4 series-connected cells.

The high  $V_{OC}$  values obtained in this thesis, instead, are the result of a series connection of six DSSCs integrated on the same FTO covered glass substrates. For the sake of clarity, the 5 tests carried out are summed up in the following in the form of a bulleted list:

- test 1): a 2 series-connected DSSCs module was built sharing the electrolyte between the two cells, the device was closed just using two clips. The electrodes had rectangular shapes ( $1.1 \times 5$  and  $1.9 \times 4.5$ ) The result was a properly working device (with a  $V_{OC} = 1.2V$ ), but with poor performance, which are due to a low  $J_{SC}$  caused by a too diluted N-719 dye solution in ethanol(0.1 mM) and maybe by the short immersion time of the glass substrates in the dye solution.
- test 2): a 6 series-connected DSSCs module was built, again, sharing the electrolyte, a meltonix layer was placed at the border of the module to seal the device. But, this time, all the cells had equal circular photoanodes(radius = 0.5cm), the N-719 solution concentration was 0.3 mM and the substrates were kept immersed in the solution for 24 hours. This time the device was not working because of the parasitic charge paths created by the shared electrolyte that had more dramatic effects with respect to the previous case because of the larger area involved (6 devices instead of 2).
- test 3): in this test, a parafilm layer was used to seal the module and insulate the single cells, instead of the meltonix film in order to simplify the sealing procedure and lower the sealing costs. This attempt was not successful because the parafilm layer was damaged by the hot press allowing the electrolyte

leakage. Thus, a meltonix film was necessary to seal the module.

- test 4): this time, a meltonix film was used to insulate the single cells and seal the device. The DSSCs module was working but showed very poor performance because of the current unbalance between the cells due to different incident power for front and back-illuminated solar cells.
- test 5): In order to reduce the current unbalance issue, another test was performed that led to the final working module, using different photoactive areas for front and back-illuminated cells. More in details, the back-illuminated cells had circular photoanodes of radius equal to 0.6 cm, while the front illuminated ones had a radius of 0.5 cm.

The final energy harvesting module showed promising features ( $\eta = 3.19\%$  and  $FF = 0.53$  under 1 SUN illumination condition). Moreover, the presence of a back-mirror boosted the module performance to  $\eta = 3.95\%$  and  $FF = 0.54$ . Under indoor illumination conditions (LED lump, 250 lux), instead, an efficiency of 10.12% was achieved. Another module, with the same design of the final one, was built using transparent  $TiO_2$  paste. It showed worse performance ( $\eta = 1.04\%$  and  $FF = 0.39$ , always under 1 SUN illumination condition) but, when considering the back-mirror configuration, the efficiency is boosted to 2.11% and the FF becomes equal to 0.49, with an increase of the  $I_{SC}$  of about 57%. This is due to the fact that the transparent paste, even if less efficient with respect to the opaque one, increases the transmittance of the incident radiation and, therefore, a bigger amount of light is reflected back by the mirror, enhancing the photogenerated current. Finally, a last device was built using again the transparent  $TiO_2$  paste, but, this time, a squared geometry was chosen for the cells electrodes. The aim of this different geometry was to try to reduce the uneffective areas of the module increasing the photoactive surfaces with respect to the geometrical ones. This module was characterized by higher

---

efficiency and FF ( $\eta = 1.65\%$ ,  $FF = 0.49$ , under 1 SUN illumination). The squared configuration is easier to be built with simple handmade processes, with respect to the round electrodes one, and enhances the photogenerated current enlarging the active surface. On the other hand, the back-mirror configuration gave not the same benefits of the previous case ( $\eta = 2\%$ ,  $FF = 0.49$  and the  $I_{SC}$  is increased just of the 21%, approximately). This worsening may be due to a detrimental contribution of the square corners that are not so effective in generating the photocurrent, but are considered in the computation of the total active area, thus lowering the final value for the efficiency. In fact, the  $TiO_2$  paste may not be uniformly deposited on the square corners causing some defect points in the cell. However, this aspect needs further investigation and many more tests than the ones performed in this thesis to be clarified. In this spirit, with an eye to the future developments of this work, a brief recap of the possible improvements in DSSCs fabrication is reported here in the form of a bulleted list. Some of them have already been established in advanced DSSCs manufacturing processes, others are still under development:

- semiconductor photoanodes: other materials are also employed, such as ZnO which shows almost the same bandgap of  $TiO_2$ , but does not require an annealing process, making it suitable for flexible DSSCs applications. On the other hand, its overall features seem to be not as good as the  $TiO_2$  ones. But, when used in combination with other wide bandgap semiconductor oxides (e.g.  $SnO_2, In_2O_3, Nb_2O_5$ ), its performance can be significantly improved[10]. Moreover, another more effective technique, such as atomic layer deposition, can be used, instead of doctor-blading, to obtain better results.
- sensitizing dye: a drawback of the N-719 dye is its poor injection efficiency in the infrared region. This issue can be mitigated introducing an extra  $TiO_2$  layer of larger particles that work as a light scattering layer increasing the optical path of the light rays and, thus, enhancing the radiation absorption.[10].

Moreover, despite the good features of N-719, other artificial dyes are under development. Black-dyes, such as N-749, show higher injection efficiency than N-719 due to a wider operating spectral range, but they are also more expensive. Another solution under investigation are the so called metal free dyes. With respect to the Ru-based ones, they show a much higher biocompatibility, but also lower efficiencies[61].

- A  $TiCl_4$  treatment on the FTO layer can be performed to reduce the recombination processes and therefore to reduce the dark current.
- electrolyte: the liquid electrolyte used in this work showed good performance, but it is not a good solution in terms of temperature stability and sealing effectiveness. In this regard, solid state electrolyte (SSE) and ionic liquids represent a good choice to face this issues (SSE does not have the problem of the electrolyte leakage and ionic liquids do not evaporate so easily as liquid electrolyte), but, on the other hand, their performance are not so good [10]. In addition to this, in order to increase the voltage drop across the cell it is possible to exploit cobalt based electrolyte that allow the presence of a  $V_{OC} \approx 0.95V$ [62].
- introduction of an anti-reflection (AR) coating in order to reduce the losses due to the reflection of the incident light on the glass substrates.
- flexibility can be a huge plus in DSSCs modules, further enlarging their applicability in many fields, such as: sensors, portable electronics, wearable technologies, smartphones, automotive[33]. A possible way to realize a flexible DSSCs module is to use ITO/PET (Indium tin oxide/polyethylene terephthalate) substrates and ZnO as the semiconductor oxide as reported in[63]. The drawback of these flexible modules is their performance which is still worse than the conventional rigid DSSCs.

---

As regards the overall HS power-pack system, in this thesis it was obtained by connecting in parallel the DSSCs module built and the commercial supercapacitor. This parallel connection was simply obtained by means of crocodile clips. The maximum OPECSE (i.e. the overall efficiency of energy harvesting and storage) was evaluated equal to 2.473%, when the voltage across the supercapacitor is equal to 3.493V and after a photocharging time of 14.18 seconds. The positive aspect of this electrical wiring connection is that it avoids the autodischarge of the supercapacitor on the DSSCs module when the light sources are turned off. On the other hand, a physical implementation of the DSSCs module and the supercapacitor on the same substrates would allow the development of a compact device paving the way to true integration of the energy harvesting and storage components. In this spirit, the same FTO glass substrates can be used for both the DSSCs module and the supercapacitor electrodes. In fact, in order to build the supercapacitor, the latter can be functionalized by depositing a water-based slurry ("90wt% of activated carbon (AC), 5wt% of conductive carbon and 5wt% binder (sodium carboxymethylcellulose, CMC" [35]) by means of doctor blade technique. Moreover,  $\text{Pyr}_{14}\text{TFSI}$  electrolyte and glass fiber separators can be used, as it can be read in [35], where the detailed fabrication steps of the supercapacitor are reported by Scalia et al.

So, in conclusion, from the work carried out in this master thesis, it is clear that the development of a renewable high voltage and high performance HS power-pack system is a key challenge for our smart technologies world. In fact, it will play a crucial role in ensuring us the best possible electronic devices user experience, respecting the environment.

# Bibliography

- [1] Hasan MA and Sumathy K. Photovoltaic thermal module concepts and their performance analysis: a review. *Renewable and Sustainable Energy Reviews*, 14(7):1845–59, 2010.
- [2] Anders Hagfeldt, Gerrit Boschloo, Licheng Sun, Lars Kloo, and Henrik Pettersson. Dye-sensitized solar cells. *Chem. Rev.*, 110(11):6595–6663, 2010.
- [3] PV EDUCATION.ORG. "standard solar spectra for space and terrestrial use". [ Online at <https://www.pveducation.org/pvcdrom/appendices/standard-solar-spectra>].
- [4] Sharma S., Jain K.K., and Sharma A. Solar cells: In research and applications - a review. *Materials Sciences and Applications*, 6:1145–1155, 2015.
- [5] Shanawani M., Masotti D., and Costanzo A. "energy-band diagram of a silicon p-n junction solar cell". [ Online at <https://www.researchgate.net/figure/Energy-band-diagram-of-a-silicon-p-n-junction-solar-cell>].
- [6] Shockley W. and Queisser H.J. Detailed balance limit of efficiency of p-n junction solar cells. *Journal of Applied Physics*, 32(3):510–519, March 1961.
- [7] A decade of perovskite photovoltaics. *Nat Energy*, 4(1), 2019. [ Online at <https://doi.org/10.1038/s41560-018-0323-9>].
- [8] K.Kakiage, Y.Aoyama, T.Yano, K.Oya, J.Fujisawa, and M.Hanaya. Improving the performance of dye-sensitized solar cells. *Chem. Commun.*, 2015. DOI:10.1039/C5CC06759F.

- [9] The National Renewable Energy Laboratory. "best research-cell efficiency chart". [ Online at <https://www.nrel.gov/pv/cell-efficiency.html>].
- [10] Md Imran Khan. A study on the optimization of dye-sensitized solar cells. Master thesis, University of South Florida, 2013.
- [11] PV EDUCATION.ORG. "i-v characteristic solar cell". [ Online at <https://www.pveducation.org/pvcdrom/solar-cell-operation/iv-curve>].
- [12] PV EDUCATION.ORG. "fill factor". [ Online at <https://www.pveducation.org/pvcdrom/solar-cell-operation/fill-factor>].
- [13] PV EDUCATION.ORG. "quantum efficiency". [ Online at <https://www.pveducation.org/pvcdrom/solar-cell-operation/quantumefficiency>].
- [14] T. Markvart, A. McEvoy, and L. Castaner. *Practical Handbook of Photovoltaics*. Elsevier, 2003.
- [15] T. Buonassisi. "fundamentals of photovoltaics", 2011. [ Online at [https://ocw.mit.edu/courses/mechanical-engineering/2-627-fundamentals-of-photovoltaics-fall-2013/lecture-videos-slides/MIT2\\_627F13\\_lec03.pdf](https://ocw.mit.edu/courses/mechanical-engineering/2-627-fundamentals-of-photovoltaics-fall-2013/lecture-videos-slides/MIT2_627F13_lec03.pdf)].
- [16] Jiawei Gong, Jing Liang, and K.Sumathy. Review on dye-sensitized solar cells(dsscs): Fundamental concepts and novel materials. *Renewable and Sustainable Energy Reviews*, 16:5848–5860, 2012.
- [17] Michael Grätzel. Solar energy conversion by dye-sensitized photovoltaic cells. *Inorg. Chem.*, 44(20):6841–6851, 2005.
- [18] Peter L. Marek. *Biomimetic dye aggregate solar cells*. Phd thesis, Technische Universität Darmstadt, 2012. [ Online at <http://tuprints.ulb.tu-darmstadt.de/3017>].

- [19] L.M. Da Silva et al. Reviewing the fundamentals of supercapacitors and the difficulties involving the analysis of the electrochemical findings obtained for porous electrode materials. *Energy Storage Materials*, 2019. [ Online at <https://doi.org/10.1016/j.ensm.2019.12.015>].
- [20] Nicola Capitello. Supercondensatori tecnologie e applicazioni, 2012.
- [21] Yong Zhang, Hui Feng, Xingbing Wu, Lizhen Wang, Aiqin Zhang, Tongchi Xia, Huichao Dong, Xiaofeng Li, and Linsen Zhang. Progress of electrochemical capacitor electrode materials: A review. *International journal of hydrogen energy*, 34:4889–4899, 2009.
- [22] R.Kötz and M. Carlen. Principles and applications of electrochemical capacitors. *Electrochimica Acta*, 45:2483–2498, 2000.
- [23] Z.Lin, E.Goikolea, A.Balducci, K.Naoi, P.L.Taberna, M.Salanne, G.Yushin, and P.Simon. Materials for supercapacitors: When li-ion battery power is not enough. *Materials Today*, 21(4):419–436, May 2018.
- [24] A.J.Rudge, J.P.Ferraris, and S.Gottesfeld. "electrochemical supercapacitors", 1996. US Patent 005527640A.
- [25] Avx supercaps bz series. [ Online at <http://www.avx.com/products/supercapacitors/bestcapreg-bz-series/>].
- [26] Sanliang Zhang and Ning Pan. Supercapacitors performance evaluation. *Advanced energy materials*, 5:1–19, 2015.
- [27] Andrea Balducci. "supercapacitors", 2018. [ Online at <https://congresses.icmab.es/matener2018/presentations/AndreaBalducci-matener2018.pdf>].

- [28] A. Sacco. Electrochemical impedance spectroscopy: Fundamentals and application in dye-sensitized solar cells. *Renewable and Sustainable Energy Reviews*, (79):814–829, 2017.
- [29] Science Direct. "cyclic voltammetry". [ Online at <https://www.sciencedirect.com/topics/materials-science/cyclic-voltammetry>].
- [30] Joshi P.S. and Sutrave D.S. A brief study of cyclic voltammetry and electrochemical analysis. *International Journal of ChemTech Research*, 11(9):77–88, 2018.
- [31] G.P. Pandey. "cyclic voltammograms os supercapacitor cell at different scan rates". [ Online at [https://www.researchgate.net/figure/a-Cyclic-voltammograms-of-supercapacitor-cell-at-different-scan-rates-b-Cyclic\\_fig2\\_271910905](https://www.researchgate.net/figure/a-Cyclic-voltammograms-of-supercapacitor-cell-at-different-scan-rates-b-Cyclic_fig2_271910905)].
- [32] Chih-Tao Chien, Pritesh Hiralal, Di-Yan Wang, I-Sheng Huang, Chia-Chun Chen, Chun-Wei Chen, and Gehan A.J.Amaratunga. Graphene-based integrated photovoltaic energy harvesting/storage device. *small*, 11(24):2929–2937, 2015.
- [33] Alberto Scalia, Federico Bella, Andrea Lamberti, Stefano Bianco, Claudio Gerbaldi, Elena Tresso, and Candido Fabrizio Pirri. A flexible and portable powerpack by solid-state supercapacitor and dye-sensitized solar cell integration. *Journal of Power Sources*, (359):311–321, 2017.
- [34] Nick Vlachopoulos, Paul Liska, Jan Augustynski, and Michael Grätzel. Very efficient visible light energy harvesting and conversion by spectral sensitization of high surface area poly crystalline titanium dioxide films. *J.Am.Chem.Soc.*, (110):1216–1220, 1988.

- [35] Alberto Scalia, Alberto Varzi, Andrea Lamberti, Timo Jacob, and Stefano Passerini. Portable high voltage integrated harvesting-storage device employing dye-sensitized solar module and all-solid-state electrochemical double layer capacitor. *Frontiers in Chemistry*, 6(443), 2018.
- [36] Vega Garita V., Ramirez Elizondo L., Narayan N., and Bauer P. Integrating a photovoltaic storage system in one device: A critical review. *Progress in Photovoltaics: research and applications*, pages 1–25, 2018. [ Online at <https://doi.org/10.1002/pip.3093>].
- [37] Z.Yang, L.Li, Y.Luo, R.He, L.Qiu, H.Lin, and H.Peng. An integrated device for both photoelectric conversion and energy storage based on free- standing and aligned carbon nanotube film. *J.Mater.Chem.A*, (1):954–958, 2013.
- [38] Alberto Scalia, Alberto Varzi, Andrea Lamberti, Elena Tresso, Sangsik Jeong, Timo Jacob, and Stefano Passerini. High energy and high voltage integrated photoelectrochemical double layer capacitor. *Sustainable Energy Fuels*, (2):968–977, 2018.
- [39] S.Nakade, Y.Saito, W.Kubo, T.Kitamura, Y.Wada, and S.Yanagida. Influence of TiO<sub>2</sub> nanoparticle size on electron diffusion and recombination in dye- sensitized TiO<sub>2</sub> solar cells. *J.Phys.Chem.B*, (107):8607–8611, 2003.
- [40] C.J.Barbe', F.Arendse, P.Comte, M.Jirousek, F.Lenzmann, V.Shklover, and M. Grätzel. Nanocrystalline titanium oxide electrodes for photovoltaic applications. *Journal of the American Ceramic Society*, 80(12):3157–3171, 1997.
- [41] S.Nakade, M.Matsuda, S.Kambe, Y.Saito, T.Kitamura, T.Sakata, Y.Wada, H.Mori, and S.Yanagida. Dependence of TiO<sub>2</sub> nanoparticle preparation methods and annealing temperature on the efficiency of dye-sensitized solar cells. *J.Phys.Chem.B*, 106(39):10004–10010, 2002.

- [42] M.K.Nazeeruddin, P.Pe'chy, T.Renouard, S.M.Zakeeruddin, R.Humphry-Baker, P.Comte, P.Liska, L.Cevey, E.Costa, V.Shklover, L.Spiccia, G.B.Deacon, C.A.Bignozzi, and M. Grätzel. Engineering of efficient panchromatic sensitizers for nanocrystalline  $\text{TiO}_2$ -based solar cells. *J.Am.Chem.Soc.*, 123(8):1613–1624, 2001.
- [43] Filippo De Angelis, Simona Fantacci, Edoardo Mosconi, Mohammad K. Nazeeruddin, and Michael Grätzel. Absorption spectra and excited state energy levels of the n-719 dye on  $\text{TiO}_2$  in dye- sensitized solar cell models. *J.Phys.Chem.C*, (115):8825–8831, 2011.
- [44] Science Direct. "absorption spectrum n-719 dye". [ Online at [https://www.researchgate.net/figure/Absorption-spectra-of-N719-dye-in-ethanol-solution-a-and-adsorbed-onto-TiO2-nanocrystal\\_fig3\\_258388308](https://www.researchgate.net/figure/Absorption-spectra-of-N719-dye-in-ethanol-solution-a-and-adsorbed-onto-TiO2-nanocrystal_fig3_258388308)].
- [45] Research Gate. "absorption spectrum of n-719 dye adsorbed on  $\text{TiO}_2$  electrodes". [ Online at [https://www.researchgate.net/figure/Absorption-spectra-of-Ru-dye-N719-a-and-Z907-b-adsorbed-TiO2-nanocrystalline\\_fig4\\_258394595](https://www.researchgate.net/figure/Absorption-spectra-of-Ru-dye-N719-a-and-Z907-b-adsorbed-TiO2-nanocrystalline_fig4_258394595)].
- [46] Kee Eun Lee, Mario A.Gomez, Samir Elouatik, and George P.Demopoulos. Further understanding of the adsorption mechanism of n-719 sensitizer on anatase  $\text{TiO}_2$  films for dssc applications using vibrational spectroscopy and confocal raman imaging. *Langmuir*, 26(12):9575–9583, 2010.
- [47] W-type series connection. [ Online at <https://www.researchgate.net/figure/Schematic-of-different>]

[-types-of-series-connections-a-monolithic-b-parallel-grid\\_fig7\\_266144048](#)].

- [48] S.Zhang and N. Pan. Supercapacitors performance evaluation. *Adv. Energy Mater*, (5):1–19, 2015.
- [49] Seigo Ito, Paul Liska, Pascal Comte, Raphaël Charvet, Peter Pe'chy, Udo Bach, Lukas Schmidt-Mende, Shaik Mohammed Zakeeruddin, Andreas Kay, Mohammad K. Nazeeruddin, and Michael Grätzel. Control of dark current in photoelectrochemical  $\text{TiO}_2/I^- - I_3^-$  and dye-sensitized solar cells. *Chem. Commun.*, (34):4351–4353, 2005.
- [50] Min-Kyu Son, Hyunwoong Seo, Kyoung-Jun Lee, Soo-Kyoung Kim, Songyi Park, Myeong-Soo Jeong, and Hee-Je Kim. Computational modeling and experimental analysis on the improvement of current mismatch in a w-type series-connected dye-sensitized solar module. *Journal of Photochemistry and Photobiology A, Chemistry*(268):17–23, 2013.
- [51] Fabrizio Giordano, Eleonora Petrolati, Thomas M. Brown, Andrea Reale, and Aldo Di Carlo. Series-connection designs for dye solar cell modules. *IEEE TRANSACTIONS ON ELECTRON DEVICES*, 58(8):2759–2764, August 2011.
- [52] Motonari Adachi, Masaru Sakamoto, Jinting Jiu, Yukio Ogata, and Seiji Isoda. Determination of parameters of electron transport in dye-sensitized solar cells using electrochemical impedance spectroscopy. *J.Phys.Chem.B*, (110):13872–13880, 2006.
- [53] Adriano Sacco, Lidia Rolle, Luciano Scaltrito, Elena Tresso, and Candido Fabrizio Pirri. Characterization of photovoltaic modules for low-power indoor application. *Applied Energy*, 102:1295–1302, 2013.

- [54] Francesca De Rossi, Tadeo Pontecorvo, and Thomas M Brown. Characterization of photovoltaic devices for indoor light harvesting and customization of flexible dye solar cells to deliver superior efficiency under artificial lighting. *Applied Energy*, 156:413–422, 2015.
- [55] Guogang Xue, Yong Guo, Tao Yu, Jie Guan, Xirui Yu, Jiyuan Zhang, Jianguo Liu, and Zhigang Zou. Degradation mechanisms investigation for long-term thermal stability of dye-sensitized solar cells. *Int. J. Electrochem. Sci*, 7:1496–1511, 2012.
- [56] Fahmid Kabir, Syed Nazmus Sakib, and Nafisa Matin. Stability study of natural green dye based dssc. *Optik*, 181:458–464, 2019.
- [57] Hung-Lin Lu, Tina F-R Shen, Sheng-Tung Huang, Yung-Liang Tung, and Thomas C-K Yang. The degradation of dye sensitized solar cell in the presence of water isotopes. *Solar energy materials and solar cells*, 95(7):1624–1629, 2011.
- [58] Wenxi Guo, Xinyu Xue, Sihong Wang, Changjian Lin, and Zhong Lin Wang. An integrated power pack of dye-sensitized solar cell and li battery based on double-sided tio2 nanotube arrays. *Nano letters*, 12(5):2520–2523, 2012.
- [59] Geetha Varnekar. Integrated tandem dye sensitized solar cell (dssc)-lithium ion battery. 2016.
- [60] Yi Di, Suping Jia, Xiaoshuang Yan, Junfei Liang, and Shengliang Hu. Available photo-charging integrated device constructed with dye-sensitized solar cells and lithium-ion battery. *New Journal of Chemistry*, 2020.
- [61] S. Shalini, R. Balasundaraprabhu, Satish Thandalam, N. Prabavathy, Senthilarasu Sundaram, and S. Prasanna. Status and outlook of sensitizers/dyes used in dye sensitized solar cells (dssc): a review: Sensitizers for dssc. *International Journal of Energy Research*, 40, 08 2016.

- [62] Aswani Yella, Hsuan-Wei Lee, Hoi Nok Tsao, Chenyi Yi, Aravind Kumar Chandiran, Md Khaja Nazeeruddin, Eric Wei-Guang Diau, Chen-Yu Yeh, Shaik M Zakeeruddin, and Michael Grätzel. Porphyrin-sensitized solar cells with cobalt (ii/iii)-based redox electrolyte exceed 12 percent efficiency. *science*, 334(6056):629–634, 2011.
- [63] Liang Zhang and Akinori Konno. Development of flexible dye-sensitized solar cell based on predyed zinc oxide nanoparticle. *Int J Electrochem Sci*, 13:344–352, 2018.